Controlling unconventional superconductivity in artificially engineered heavy-fermion superlattices

Masahiro Naritsuka

January, 2020

Abstract

Strongly correlated electrons have been one of the most important topics in condensed matter physics research for more than half a century. They exhibit a rich variety of exotic phenomena such as unconventional superconductivity, non-Fermi liquid behavior, and exotic orders. In various families of strongly correlated electron systems, including cuprates, iron pnictides, and heavy fermion compounds, superconductivity is often observed near a magnetic instability. In particular, the highest superconducting transition temperature is often observed near a magnetic quantum critical point (QCP), realized by suppressing a finite-temperature magnetic ordering transition to zero temperature via some non-thermal tuning parameters, such as pressure and doping. This suggests that the proliferation of critical magnetic excitations resulting from the QCP plays an essential role in Cooper pairing. Another fascinating and puzzling phenomenon related to the QCP is a microscopic coexistence of a superconducting phase and a magnetically ordered phase containing the same charge carriers, which is a prominent example of unusual emerging electronic phases. However, despite the vast amount of research, there remain many unsolved mysteries about the intertwining relationship between superconductivity and magnetism.

Recently, by using a state-of-the-art molecular beam epitaxy (MBE) technique, the artificially engineered superlattices with alternating layers of heavy-fermion superconductors or heavy-fermion antiferromagnetic (AFM) compounds and conventional metals are successfully fabricated. In these superlattices, the superconducting heavy quasiparticles as well as magnetic fluctuations can be confined within a few atomic layers. These heavy-fermion superlattices pave the way for studying the mutual interactions between the unconventional superconducting state and magnetically ordered or conventional metallic states through the atomic interface and thereby seek clues to the above-mentioned mysteries.

Rashba effect is a topic of growing interest in two-dimensional (2D) superconductivity at the interface between two different materials, which inevitably have broken inversion symmetry. In some systems the Rashba effect is tunable and enables the possibility of achieving exotic states, such as topological superconducting states. However, in these 2D systems discovered until now, superconductivity emerges from weakly correlated electron states. Thus, in 2D superconductors with strong Rashba effect, the role of strong electron-electron interaction has remained largely unexplored. The situation calls for new 2D systems with significant electron correlations and tunable Rashba effect.

In this thesis, we introduce new strategies for controlling unconventional superconductivity by fabricating two kinds of heavy-fermion superlattices, namely the tricolor superlattices of $YbCoIn_5/CeCoIn_5/YbRhIn_5$, and the hybrid superlattices of

$CeCoIn_5/CeRhIn_5$ and $CeCoIn_5/CeIn_3$. In the tricolor superlattices, we demonstrate that the Rashba effect induced by the global inversion symmetry breaking leads to profound changes in the superconducting properties of $CeCoIn_5$ with atomic thickness. We find a possible signature of an exotic superconducting phase under the magnetic field. In the hybrid superlattices, we demonstrate that superconductivity can be modified by magnetic fluctuations injected through interfaces.

Emergent exotic superconductivity in $YbCoIn_5/CeCoIn_5/YbRhIn_5$ tricolor superlattices

Rashba effect, which lifts the electron-spin degeneracy under broken inversion symmetry, can dramatically affect the electronic properties, giving rise to a number of intriguing phenomena including exotic superconducting pairing state. Here, to introduce the Rashba effect in 2D strongly correlated electron systems, we fabricated noncentrosymmetric (tricolor) superlattices in which *d*-wave heavy-fermion superconductor $CeCoIn_5$ is sandwiched by two different nonmagnetic metals, $YbCoIn_5$ and $YbRhIn_5$.

We find that the global inversion symmetry breaking in these tricolor superlattices leads to profound changes in the superconducting properties of $CeCoIn_5$ with atomic layer thickness, which are revealed by unusual temperature and angular dependencies of upper critical fields that are in marked contrast with the bulk $CeCoIn_5$ single crystals. We demonstrate that the magnitude of the Rashba effect incorporated into the 2D $CeCoIn_5$ block layers (BLs) is controllable mainly by changing the thickness of $CeCoIn_5$ BLs. Moreover, the temperature dependence of the in-plane upper critical field exhibits an anomalous upturn at low temperatures, which is attributed to a possible emergence of a helical or stripe superconducting state.

Our results demonstrate that the tricolor superlattices provide a new playground for exploring exotic superconducting states in the strongly correlated 2D electron systems with the Rashba effect.

Tuning the pairing interaction through interfaces in hybrid superlattices of $CeCoIn_5/CeRhIn_5$ and $CeCoIn_5/CeIn_3$

Unconventional superconductivity and magnetism are intertwined on a microscopic level in a broad class of materials. A new approach to this most fundamental and hotly debated issue focuses on the role of interactions between superconducting electrons and bosonic fluctuations at the interface between adjacent layers in heterostructures.

To study the role of interaction between *d*-wave superconducting electrons and magnetic fluctuations at the interface between adjacent layers in heterostructures, we fabricate hybrid superlattices consisting of alternating atomic layers of *d*-wave superconductor $CeCoIn_5$ and AFM metal $CeRhIn_5$, in which the AFM order can be suppressed by applying pressure. We also establish the hydrostatic pressure measurements on the heavy-fermion thin films and heavy-fermion superlattices. We find that the superconducting and AFM states coexist in spatially separated layers, but their mutual coupling via the interface significantly modifies the superconducting properties.

An analysis of upper critical fields reveals that in the vicinity of the QCP of $CeRhIn_5$ BLs, the superconducting pairing strength $2\Delta/k_BT_c$ is sharply increased. This demonstrates that superconducting pairing can be tuned non-trivially by magnetic fluctuations (paramagnons) injected through the interface, leading to the maximization of the pairing interaction.

Following the results on $CeCoIn_5/CeRhIn_5$ superlattices, we design and fabricate hybrid superlattices consisting of alternating layers of $CeCoIn_5$ and heavy-fermion AFM metal $CeIn_3$, in which the AFM transition temperature is higher than that of $CeRhIn_5$ and AFM order can be suppressed by pressure as in $CeRhIn_5$.

We demonstrate that by changing the number of magnetic layers in the superlattice, three-dimensional magnetic order is realized in $CeCoIn_5/CeIn_3$, while 2D magnetic order is realized in $CeCoIn_5/CeRhIn_5$. The analysis of the upper critical field reveals that the superconductivity of the $CeCoIn_5$ layers is not affected by the magnetic fluctuations of the $CeIn_3$ layer even in the vicinity of the QCP of $CeIn_3$ BLs. This is in stark contrast to $CeCoIn_5/CeRhIn_5$ superlattices, in which the superconductivity in the $CeCoIn_5$ BLs is profoundly affected by AFM fluctuations in the $CeRhIn_5$ BLs. The present results show that although AFM fluctuations are injected into the $CeCoIn_5$ BLs from the $CeIn_3$ BLs through the interface, they barely affect the force that binds superconducting electron pairs. These results demonstrate that 2D AFM fluctuations are essentially important for the pairing interactions in $CeCoIn_5$.

Contents

Chapter 1

Introduction

1.1 Superconductivity

Superconductivity, one of the most famous macroscopic quantum phenomenon, was discovered by Heike Kamerlingh Onnes in 1911 when measuring the electrical resistivity of mercury. In 1957, half a century after the discovery of superconductivity, the BCS theory proposed by John Bardeen, Leon Neil Cooper and John Robert Schrieffer successfully explained various superconducting phenomena quantitatively. It was suggested that superconductivity is established through quantum condensation of a vast number of Cooper pairs formed by exchanging phonons between two electrons with opposite momentum and spins near the Fermi energy. This phonon-mediated superconductivity is characterized by an isotropic s-wave superconducting gap structure and is now called 'conventional' superconductivity.

In the last three decades, many unconventional superconductors, including heavy fermions, organic materials, copper oxide, and iron-based superconductors, were discovered: they seem to violate the basis of the BCS theory to some extent. These compounds are known to be strongly correlated electron systems. Among them, the discovery of high-temperature copper oxide superconductors by Johannes Georg Bednorz and Karl Alexander Müller in 1987, was a breakthrough in the investigation of the superconducting pairing mechanism. At that time, the superconducting transition temperature was below 35 K in $La_{2-x}Ba_xCuO_4$. The highest-T_c achieved for cuprates was for $HgBa_2Ca_2Cu_3O_{8+\delta}$ at 164 K under pressure. In copper oxide superconductors, also called cuprates, superconductivity is known to appear on doping charge carriers (electrons or holes) into the antiferromagnetic (AFM) Mott insulator. In terms of the above, the superconductivity in cuprates is beyond the BCS paradigm, opening the door to study unconventional superconductivity.

Figures 1.1(a)-(d) shows phase diagrams of several strongly correlated materials. The common aspects of these phase diagrams are following. The superconducting phase appears near the quantum critical point (QCP), where the ordered phase (e.g., AFM order) is suppressed by doping or pressure. As will be described later, the observation of various anomalous electronic states has clarified that critical magnetic fluctuations develop near the QCP. This critical magnetic fluctuation is considered to be very im-

portant for unconventional superconductivity.

Among strongly correlated electron systems, the ones with the strongest electron correlation comprise a group of materials called heavy-fermion systems. In these compounds containing rare-earth elements, a variety of electrical and magnetic phases are produced by the conduction of f-electrons with large angular momenta through c-f hybridization. As will be described later, many heavy-fermion systems are found to be located near the QCP, where the Kondo effect and the Ruderman-Kittel-Kasuya-Yoshida (RKKY) interaction compete each other. Heavy-fermion systems are very suitable for studying quantum critical phenomena, magnetism, and emerging unconventional superconductivity. When it is difficult to form a conventional s-wave Cooper pair due to the strong Coulomb repulsion between electrons, an anisotropic pair with a higher internal angular momentum is established. A significant number of theoretical and experimental studies have been conducted so far, and it has been confirmed that d-wave superconductivity with sign inversion is realized in the superconducting gap structure in heavy-electron superconductors, and the mechanism involves pairing mediated by AFM fluctuation.

1.2 Quantum critical point (QCP)

Usually, the phase transition from some ordered phase to a disordered phase occurs with increasing temperature. For example, neighboring magnetic moments that are parallel to each other in a ferromagnet become disordered at the Curie temperature. Thermal fluctuations drive such a phase transition. Meanwhile, in many strongly correlated electron systems, the magnetic ordered phase can be suppressed by tuning the pressure or the substitution of elements, and the magnetic transition temperature can be continuously reduced to zero temperature. The phase transition from the magnetically ordered phase to the paramagnetic phase at $T = 0$ is called the quantum phase transition, and when the transition is continuous, the transition point is called a QCP.

Figure 1.2 depicts the schematic phase diagram of a quantum phase transition. Here, g is a non-thermal parameter such as pressure, substitution, and magnetic field. When g is small, a second-order phase transition occurs. Near the transition temperature T_o, a thermal fluctuation region exists, in which conventional scaling properties can be observed. As g is increased, the transition temperature is suppressed and becomes zero when $g = g_c$. At the QCP, a quantum magnetic fluctuation develops, leading to anomalous behavior in various physical quantities. Interestingly, this quantum critical regime is observed over a wide region in a fan shape around g_c.

The quantum-classical crossover can be considered as follows. The order parameter correlation time ξ_τ (i.e., correlation length along the imaginary time axis), is denoted as $\xi_\tau \sim \xi^z$, where ξ is the correlation length and z is the dynamical exponent of the quantum phase transition [5]. Therefore, the characteristic energy scale of the quantum fluctuations is

$$\hbar\omega = \hbar\xi_\tau^{-1} \propto \xi^{-z}. \tag{1.1}$$

The relationship between its magnitude and the thermal fluctuation energy scale de-

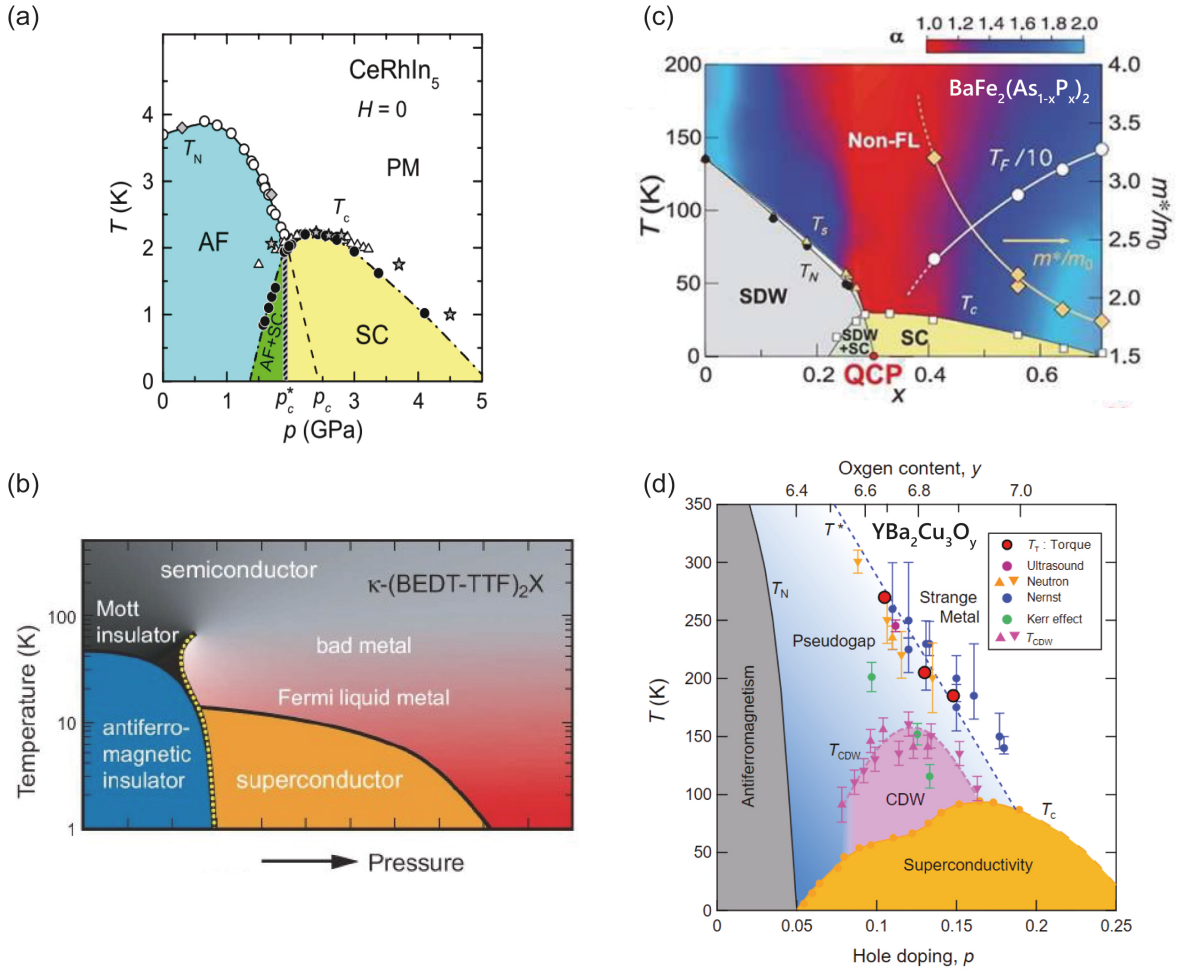

Figure 1.1: Phase diagram of several strongly correlated materials. (a) Heavy-fermion superconductor $CeRhIn_5$ [1], (b) Fe-pnictide $BaFe_2(As_{1-x}P_x)_2$ [2], (c) organic κ-(BEDT-TTF)$_2$X [3], and (d) high-T_c cuprate $YBa_2Cu_3O_y$ [4].

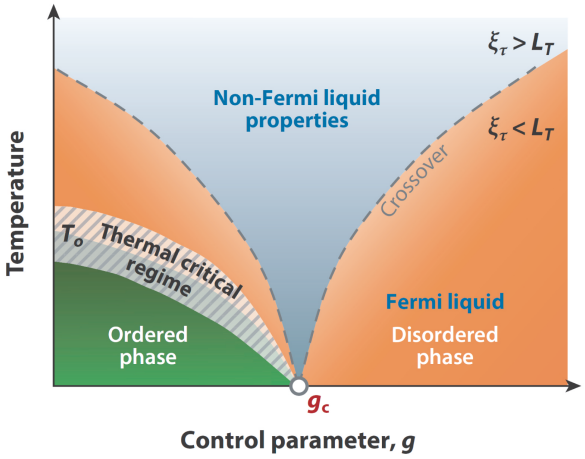

Figure 1.2: General phase diagram in the vicinity of the QCP [2]. The non-Fermi liquid region spreads in a fan shape around the QCP. Unconventional superconductivity often emerges in the vicinity of QCP and quantum fluctuations influencing the QCP play a key role in forming Cooper pairs.

termines whether quantum fluctuations or thermal fluctuations are dominant in the system.

As ξ diverges as $\xi \propto |g - g_c|^{-\nu}$, where ν is the correlation length exponent, the crossover line is defined by

$$k_{\mathrm{B}}T \simeq |g - g_c|^{-\nu z}. \tag{1.2}$$

Therefore, the boundary spreads in a fan shape around g_c.

The self-consistent renormalization (SCR) theory constructed by Moriya *et al.* has been successfully applied to the understanding of the thermal equilibrium state of magnetic materials near the QCP [6]. They gave qualitatively new results on specific heat, resistivity, and nuclear magnetic relaxation rate by introducing the interaction between different modes of spin fluctuation. Table 1.1 summarizes the temperature dependence of the physical properties near a magnetic QCP. Therefore, detailed examination of the temperature dependence of these physical quantities is very important to discuss the nature of the QCP and how close the system is to it. For instance, in the two-dimensional (2D) AFM QCP case, resistivity shows a T-linear dependence at low temperature, the specific heat devided by temperature $C/T \propto -\ln T$, and the nuclear spin-lattice relaxation rate $1/T_1T \propto \ln T$. As mentioned in Section 1.1, in many strongly correlated materials, unconventional superconductivity emerges in the vicinity of the QCP [1–3, 7]. Furthermore, the superconducting transition temperature often has a maximum at the QCP. These indicate that the pairing interactions in unconventional superconductivity are not phonon vibrations but other mechanisms related to the quantum instability arising from the QCP such as AFM critical fluctuations.

Table 1.1: Temperature dependence of physical properties near a magnetic QCP, compared with that for Fermi liquid [8]. a and b are constants.

	$\chi(Q)$	C/T	ρ	$1/T_1T$
Ferromagnetic 3D	$T^{4/3}$	$-\ln T$	$T^{5/3}$	$T^{-4/3}$
Ferromagnetic 2D	$(-T\ln T)^{-1}$	$T^{-1/3}$	$T^{4/3}$	$T^{-1/2}(-\ln T)^{-3/2}$
Antiferromagnetic 3D	$T^{3/2}$	$-T^{1/2}$	$T^{3/2}$	$T^{-3/4}$
Antiferromagnetic 2D	$-T/\ln T$	$-\ln T$	T	$-\ln T$
Fermi liquid	$a+bT^2$	a	T^2	a

1.3 Heavy-fermion compounds

In rare-earth and actinide metals, the f-shell electrons are localized at high temperatures but couple with conduction electrons residing in s, p, d orbitals at low temperature. Several ground states emerge that are determined by the competition between the Kondo effect [9] and Ruderman–Kittel–Kasuya–Yoshida (RKKY) exchange interaction [10–12]. The f-electron compounds are generally described by the Kondo-lattice system. The Kondo-lattice Hamiltonian is given by

$$H = \sum_{ij} t_{ij} c^\dagger_{i\sigma} c_{j\sigma} + J \sum_i \boldsymbol{S}_i \cdot \boldsymbol{s}_i, \tag{1.3}$$

where t_{ij} is the hopping matrix element, $c^\dagger_{i\sigma}(c_{i\sigma})$ is the creation (anihilation) operator of the conduction electrons, $\boldsymbol{S}_i$ is the local spin, $\boldsymbol{s}_i$ is the spin of a conduction electron, J is the antiferromagnetic Kondo coupling constant. The second term describes the Kondo interaction between localized f-electrons and conduction electrons. For the high temperature well above the characteristic Kondo temperature T_K, the system is in a paramagnetic state described by Curie-Weiss law. With decreasing temperature below T_K, the f-electron is entangled with surrounding conduction electrons and form a Kondo singlet, resulting in the screening of the local moments. The Kondo temperature is given by

$$k_\mathrm{B} T_\mathrm{K} \sim \frac{1}{g(E_\mathrm{F})} \exp(-\frac{1}{Jg(E_\mathrm{F})}) \tag{1.4}$$

where $g(E_\mathrm{F})$ is the density of state at the Fermi energy. For $T \ll T_\mathrm{K}$, Bloch's theorem insures that Kondo singlets couple coherently in Kondo lattice. Therefore, the narrow quasiparticle band is formed near the Fermi energy through c-f hybridization. As a consequence, the quasiparticle effective mass m^* can be several hundred times larger than that of copper, which gives rise to the term 'heavy fermion'.

The RKKY exchange interaction is a conduction-electron-mediated indirect interaction between f-electrons which stabilizes long-range magnetically ordered ground state. The RKKY Hamiltonian is given by

$$H_\mathrm{RKKY} = \sum_{ij} J_{ij} \boldsymbol{S}_i \cdot \boldsymbol{S}_j, \tag{1.5}$$

$$J_{ij} \propto J^2 g(E_{\rm F}) \frac{\cos(2k_{\rm F} r_{ij})}{r_{ij}^3}, \tag{1.6}$$

where J_{ij} is the RKKY coupling constant. The characteristic temperature is given by

$$k_{\rm B} T_{\rm RKKY} \sim J^2 g(E_{\rm F}). \tag{1.7}$$

In contrast to the case of the Kondo effect leading to a non-magnetic ground state, the RKKY exchange interaction stabilizes the magnetically ordered ground state. To understand the bilateral character in heavy-fermion systems, Mott and Doniach proposed the Kondo lattice model in which f-electrons form a lattice and are immersed in a sea of conduction electrons [13, 14]. Here, localized f-electrons are screen by the Kondo effect to form a nonmagnetic phase, and the RKKY exchange interaction stabilizes the magnetic ordered ground state. There are two energy scales in the Kondo lattice: Kondo temperature $T_{\rm K} \sim De^{-1/(2J\rho)}$ and RKKY scale $J_{\rm RKKY} \sim J^2\rho$, where ρ is the density of state of the conduction sea and D is the bandwidth. They proposed that the heavy electron system is located near the QCP of the AFM and nonmagnetic phases because the two energy scales are close. In fact, quantum critical phenomena appear in various physical quantities in many heavy electron systems. For example, $CeIn_3$ and $CeCu_{6-x}Au_x$ are well explained by the three-dimensional (3D) AFM QCP model [1,15]. On the other hand, $YbRh_2Si_2$ and $CeRhIn_5$ show distant behavior and propose a new model of quantum critical phenomena [16,17]. It has been pointed out that such various quantum critical phenomena appear in heavy electron systems because in real materials, it is necessary to consider the duality of itinerancy and localization of f-electrons [18].

By virtue of the diversity and highly tunable nature of their ground state, heavy-fermion compounds are suitable systems for exploring the emergent properties of correlated quantum matter. In this section, we will describe historical aspects of heavy-fermion superconductors. Then, we will discuss quantum critical phenomena and unconventional superconductivity of typical heavy-fermion compounds, $CeCoIn_5$, $CeRhIn_5$, and $CeIn_3$.

1.3.1 Heavy-fermion superconductors

The first heavy-electron superconductor was $CeCu_2Si_2$, reported by Steglich in 1979 [23], with $T_c = 0.6\,\mathrm{K}$. Contrary to previous examples, superconductivity appears from the normal state with strong temperature dependent paramagnetism at low temperatures, and T_c is a considerable part of degeneracy temperature $T_{\rm F}$ of heavy electrons forming Cooper pairs. The hierarchy of energy scales $k_{\rm B}T_c < k_{\rm B}T_{\rm F} < k_{\rm B}\Theta_{\rm D}$, where $k_{\rm B}\Theta_{\rm D}$ is a characteristic phonon energy was not consistent with BCS. Later, UBe_{13} [24], UPt_3 [25], and URu_2Si_2 [26–28] were discovered and investigated as first-generation heavy-electron superconductors. In these materials, unconventional superconductivity is developed from the nonmagnetic heavy Fermi liquid state.

The second generation heavy-fermion superconductors are $CeIn_3$, $CePd_2Si_2$, UPd_2Al_3, and UNi_2Al_3 [1, 29]. In $CeIn_3$ and $CePd_2Si_2$, the parent material is antiferromagnetic and the superconductivity appears when the magnetism is suppressed by

pressure. Both UPd_2Al_3 and UNi_2Al_3 exhibit the coexistence of unconventional superconductivity and magnetic order at low temperatures. It is widely believed that critical magnetic fluctuations that develop near the magnetic quantum critical point play an important role in the non-Fermi liquid behavior and the mechanism of superconductivity.

The third generation heavy-fermion superconductors are the 'Ce115' family, $CeCoIn_5$ [19], $CeRhIn_5$ [20], and $CeIrIn_5$ [21]. In contrast to the first and second generation heavy-fermion superconductors whose transition temperature was 1K or much lower, that of $CeCoIn_5$ is 2.3 K [19]. The $CeCoIn_5$ has a quasi-two-dimensional Fermi surface shape, and it is thought that two-dimensionality enhances the superconducting transition temperature [30]. The 'Ce115' systems share similarities to copper oxide high-temperature superconductors, such as the appearance of unconventional superconductivity near the antiferromagnetic QCP, d-wave symmetry in superconducting gap function, and the realization of a 'high' superconducting transition temperature relative to Fermi energy.

The 'Ce115' family has attracted extensive interest because of its anomalous normal state transport and superconducting properties, such as non-Fermi liquid behavior, QCP, $d_{x^2-y^2}$ superconducting gap symmetry, strong Pauli effect, possible Fulde–Ferrel–Larkin–Ovchinnikov (FFLO) phase, and the coexistence of superconductivity and magnetic order at low temperatures and high fields. In the following section, we describe the physical properties of $CeCoIn_5$ in detail.

1.3.2 $CeCoIn_5$

$CeCoIn_5$ crystallizes in a tetragonal $HoCoGa_5$ type structure ($P4/mmm$) comprising alternating layers of $CeIn_3$ and $CoIn_2$ stacked along the c-axis (Fig. 1.3(a)). $CeCoIn_5$ is a heavy-fermion superconductor with a superconducting transition temperature of T_c = 2.3 K, which is the highest among those of Ce-based heavy-fermion superconductors. A large Sommerfeld constant $\gamma = C/T = 290$ mJ mol^{-1}K^{-2} is observed just above T_c [19]. The normalized jump in heat capacity $\Delta C/\gamma T_c \sim 4.5$ suggests that $CeCoIn_5$ exhibits very strong coupling superconductivity compared with the BCS value of 1.43 [31].

Figure 1.3(b) is the Fermi surfaces obtained from de Haas-van Alphen (dHvA) measurement, suggesting that the main Fermi surface sheet with the cyclotron mass $m_c^* = 87m_0$ is highly corrugate [32, 36]. The upper critical field $H_{c2}(T)$ of $CeCoIn_5$ is anisotropic when the magnetic field is aligned parallel and perpendicular to the $CeIn_3$ planes ($H_{c2}^{H\|ab}/H_{c2}^{H\perp ab} \sim 2.4$), which means that anisotropic superconductivity is realized in $CeCoIn_5$.

The Pauli paramagnetic limit for $CeCoIn_5$ is estimated $H_P = 1.84T_c \simeq 4.2$ K using T_c = 2.3 K, and orbital limiting fields calculated using the Werthamer-Helfand-Hohenberg (WHH) model [34] are $H_{c2ab}^{\rm orb} \simeq 48.4$ T, and $H_{c2c}^{\rm orb} \simeq 17.1$ T. These indicate that superconductivity in $CeCoIn_5$ is strongly Pauli-limited.

The coherence length calculated from the measured zero-temperature upper critical field is $\xi_c(0) = 5$ nm for the field along the c-axis, and $\xi_{ab}(0) = 8$ nm in the basal plane. The mean free path $\ell \sim 2\,\mu$m of $CeCoIn_5$ estimated from the thermal conductivity

measurement at zero field is much longer than ξ, indicating that $CeCoIn_5$ is in the clean limit.

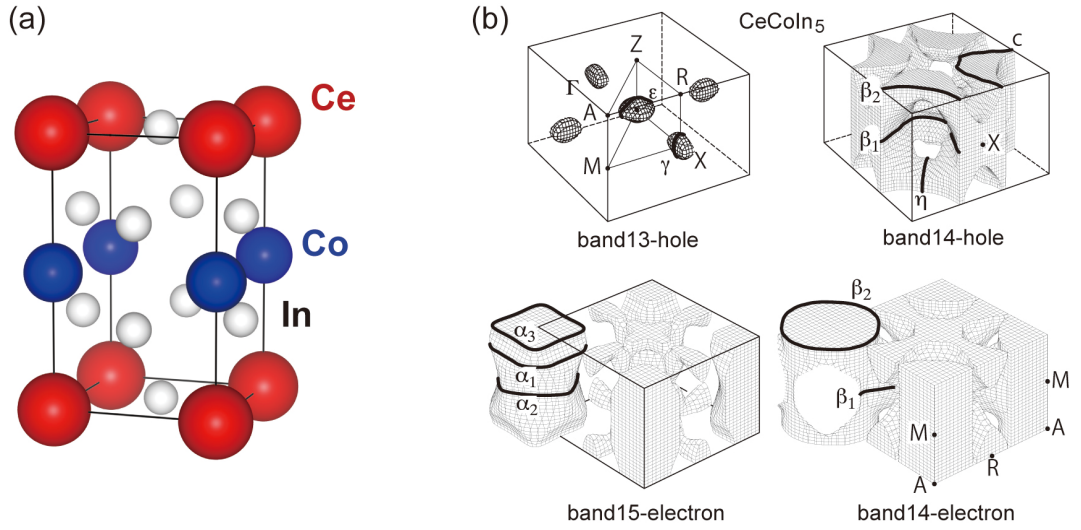

Figure 1.3: (a) Crystal structure of $CeCoIn_5$ (b) Fermi surface of $CeCoIn_5$ based on the itinerant $4f$ band model according to ref. [35]

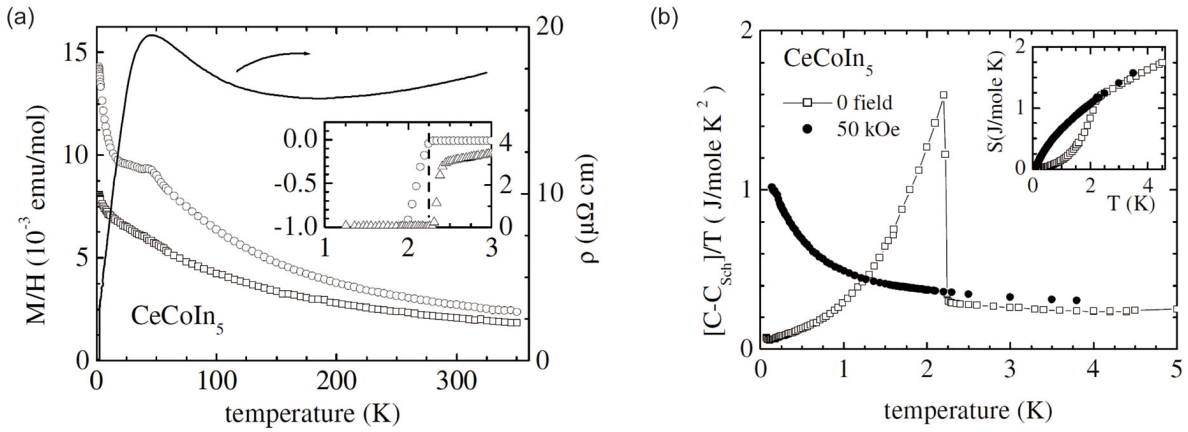

Figure 1.4: (b) Temperature dependence of specific heat divided by temperature of $CeCoIn_5$ (with nuclear Schottky contribution subtracted), showing the large entropy of condensation associated with the superconducting phase. After ref. [19].

Non-Fermi liquid behavior and AFM quantum criticality

The temperature dependence of the physical quantities exhibits a striking deviation from conventional Fermi-liquid behavior. For example, the electronic resistivity shows a T-linear dependence $\rho \sim T$ [37], a nuclear spin relaxation rate of $1/T_1 \sim T^{1/4}$ [38], and the ratio of specific heat to temperature $C/T \sim -\ln T/T_0$ [19]. The non-Fermi liquid behavior in the normal state and unconventional superconductivity in $CeCoIn_5$

are presumed to arise from the proximity of the system to a QCP that separates the paramagnetic and AFM phases.

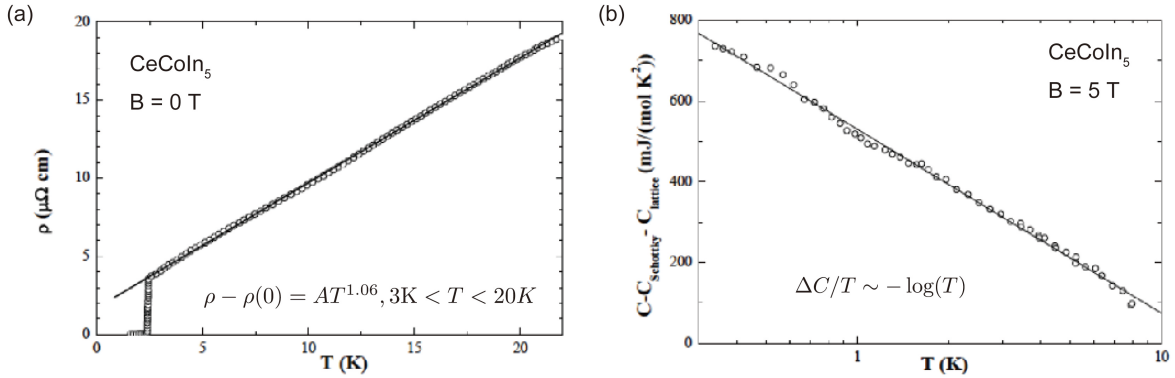

Figure 1.5: (a) Linear resistivity of $CeCoIn_5$ and (b) specific heat in the normal state under magnetic field $B = 5\,\mathrm{T}$ parallel to the c-axis [39]

It is known that the ground state is sensitive to chemical substitution in heavy-fermion compounds. For $CeCoIn_5$, the ground states were investigated by substitutions on the In site with Cd [40–44] or Sn [45–49] (see Figure 1.6). Hole doping with Cd and electron doping with Sn have very different consequences on c-f hybridization. Cd leads to a reduction in the T_c and an AFM order appears. There is a region of coexistence phase of superconductivity and AFM order. For higher Cd doping superconductivity is suppressed and T_N increases. When In sites are substituted by Cd atoms, it can be assumed that a negative chemical pressure is applied because the Cd atom has a smaller ionic radius than the In atom. Pressure experiments undertaken using $CeCoIn_{5(1-x)}Cd_x$ showed that a nominal Cd concentration of 5% corresponds to a negative chemical pressure of 0.7 GPa [41]. Recently, soft-x-ray absorption spectroscopy has shown that Cd substitution changes the ground state from superconductive to AFM, but the $4f$ wave function remains unchanged [50]. This is contrasted by the change in wave function due to Sn substitution in which c-f hybridization was increased. Increasing Sn in $CeCo(In_{1-y}Sn_y)_5$, T_c decreases monotonically and no further order appears, indicating the system coming away from the AFM QCP. Hydrostatic pressure measurements carried out for pure $CeCoIn_5$ also support this interpretation. It should be noted that the maximum value of T_c seen at $P_\mathrm{max} = 1.5\,\mathrm{GPa}$ is mainly due to the change in bandwidth due to pressure, and there is no AFM QCP at P_max. The fact that a non-Fermi liquid behavior is observed at ambient pressure and the AFM phase appears on the small negative pressure side indicates that the system is located in the vicinity of AFM QCP at ambient pressure in $CeCoIn_5$.

A similar phase diagram also appears for $Ce(Rh_x, Co_{1-x})In_5$. Figure 1.7 is the phase diagram of $Ce(Rh_x, Co_{1-x})In_5$ obtained from the specific heat, electrical resistance, and magnetic susceptibility. Superconductivity appears in the region $0.4 < x < 1$. The antiferromagnetic transition temperature decreases with increasing Co content and becomes $T = 0$ at around the critical concentration $x_c = 0.8$. There is no evidence of reconstruction of Fermi surface sheet nor any substantial enhancement of the cyclotron

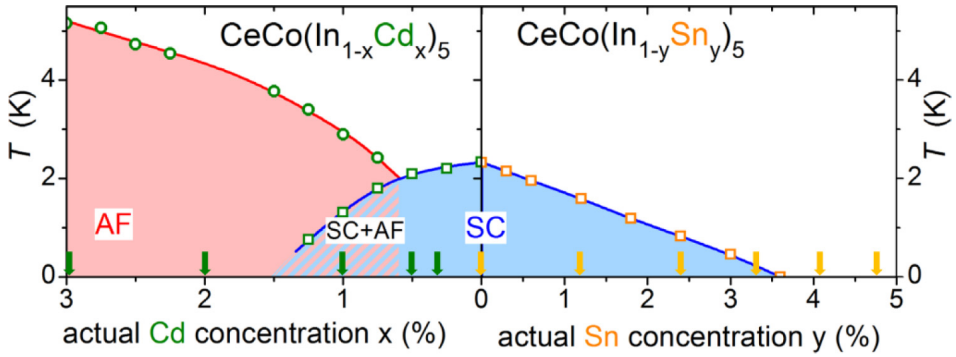

Figure 1.6: Temperature substitution phase diagram of $CeCo(In_{1-x}Cd_x)_5$ [40] and $CeCo(In_{1-y}Sn_y)_5$ [49]. This graph is adapted from Refs. [50]

mass near x_c. Instead, a qualitative change in the Fermi surface occurs well below the quantum critical concentration separating antiferromagnetic and paramagnetic ground states. The neutron scattering experiments revealed that the superconductivity competes with the incommensurate $(0.5, 0.5, 0.297)$ AFM order, while it coexists with the commensurate $(0.5, 0.5, 0.5)$ AFM order [51].

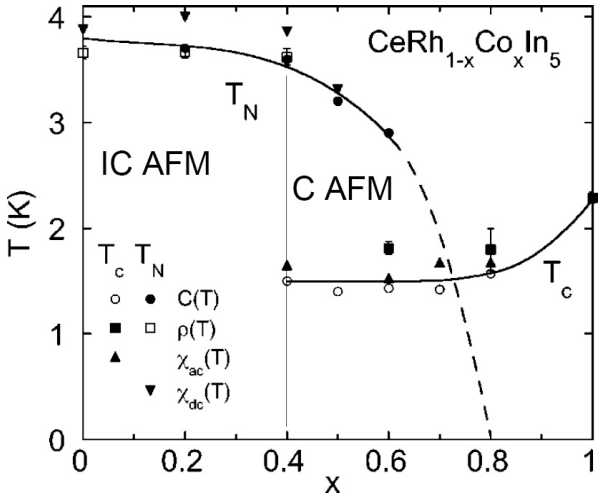

Figure 1.7: x-T phase diagram of $Ce(Rh_{1-x}, Co_x)In_5$. 'C AFM' and 'IC AFM' indicate commensurate and incommensurate AFM order, respectively. This graph is adapted from Refs. [52]

Superconducting gap symmetry

Information on the pairing interaction can be obtained by examining the superconducting gap symmetry. In the case of superconductivity mediated by AFM fluctuations, sign change in the superconducting gap function, $\Delta(\boldsymbol{k})\Delta(\boldsymbol{k}-\boldsymbol{Q}) < 0$, is required. Such a sign change is expected for a gap with d-wave symmetry with line nodes in the superconducting gap. For instance, tunneling spectra [53, 54], a four-fold modulation in the angular dependence of thermal conductivity [55] and specific heat [56], a power-law

temperature dependence of thermal conductivity, $1/T_1$ [38], and T^2 dependence of C/T below T_c [56], are all consistent with $d_{x^2-y^2}$ symmetry of the superconducting gap in which line nodes extend along the c-axis in $CeCoIn_5$. This is concrete evidence that AFM fluctuations are important for the superconductivity in this system.

Q-phase

In high magnetic fields and at low temperatures, a specific magnetic phase within the superconducting region was discovered and linked to a FFLO phase [57,58]. The FFLO state is predicted to appear in clean, Pauli-limited superconductors, and proposed in the 1960s but has never been demonstrated unambiguously so far. In the FFLO phase, the order parameter of superconductivity is spatially modulated, and the Cooper pair has a finite momentum. To stabilize the FFLO state, we need large Maki parameter $\alpha = \sqrt{2}H_{c2}^{\rm orb}/H_{c2}^{\rm P}$. Because the spin polarization due to the Zeeman effect produces FFLO superconductivity, the upper critical field due to the orbital critical field must be sufficiently large. The orbital upper critical field is defined as $H_{c2}^{\rm orb} \approx \Phi_0/2\pi\xi^2$, where coherence length is $\xi = \hbar v_F/\pi\Delta \approx E_{\rm F}/\Delta$. In a system with a heavy effective mass, that is, a system with a small Fermi energy $E_{\rm F}$, the orbital critical field becomes large, and a large Maki parameter is realized. The cleanness of the sample is also important because the FFLO phase becomes unstable in the presence of the nonuniformity of the sample. In fact, at low temperatures and high magnetic fields, first-order phase transitions have been observed by the measurement of thermal conductivity, specific heat, magnetic susceptibility, magnetocaloric effect and thermal expansion, providing evidence that the Pauli effect is dominant. The Maki parameter is $\alpha = 4.6$ for $H \parallel ab$, and $\alpha = 3.6$ for $H \parallel c$, which greatly exceeds the theoretical minimum requirement of 1.8. Meanwhile, nuclear magnetic resonance (NMR) and neutron scattering measurements revealed the presence of a magnetic spin-density wave (SDW) order in the high-field low-temperature phase. This 'Q'-phase is inconsistent with the simple picture of the FFLO state. For a magnetic ordering wave vector $(q, q, 0.5)$, there are two possible SDW domains, one with $Q_1 = (q, q, 0.5)$ and the other with $Q_2 = (q, -q, 0.5)$. Remarkably, recent neutron scattering measurements reveal that the SDW order is single domain, with the ordering vector being either Q_1 or Q_2, with $q \approx 0.45$ [60]. When the magnetic field is rotated within the ab plane about the a-axis direction, the ordering vector switches sharply between Q_1 and Q_2, choosing the one that is more perpendicular to the magnetic field. It was suggested that a secondary p-wave pair-density-wave (PDW) component drives the switching behavior of the ordering vector in the direction of the magnetic field. This scenario was further supported by thermal conductivity measurements [61].

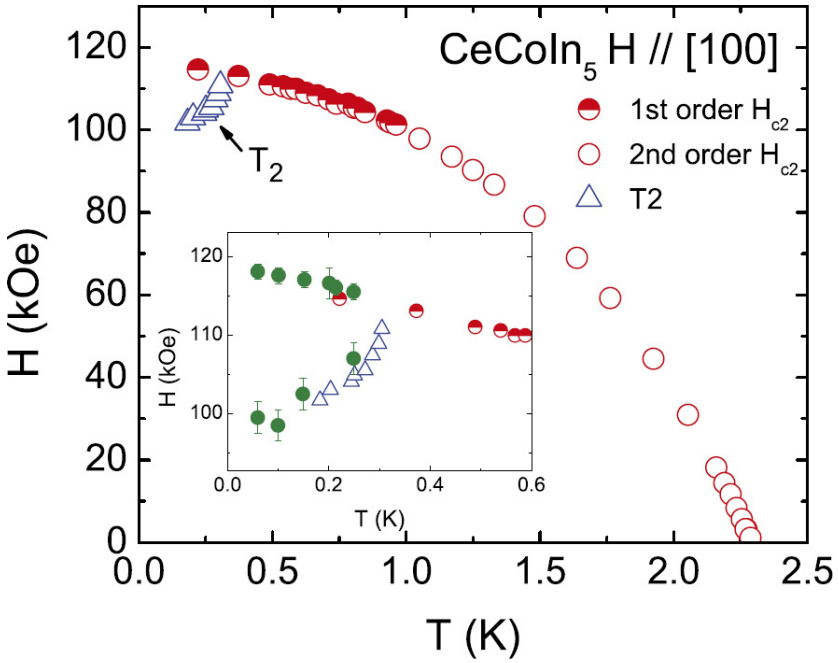

Figure 1.8: Magnetic field dependence of phase transition in $CeCoIn_5$. Circles denote the upper critical field boundary that is second (first) order, as indicated by open (half-filled) symbols. Open triangles define a line of field-induced second order phase transition, labeled T_2, inside the superconducting state, called the 'Q'-phase. The inset is an expanded view of the low-T, high-H part of the phase diagram and includes results from neutron diffraction. Closed circles in the inset represent points at which AFM order is detected. From ref. [59].

1.3.3 $CeRhIn_5$

$CeRhIn_5$ has the same crystal structure as $CeCoIn_5$ and a smaller quasi-2D Fermi surface than that of $CeCoIn_5$ with reflecting localized nature of f-electrons. At ambient pressure, this compound undergoes an AFM transition at Néel temperature $T_N = 3.8\,K$, with the ordered magnetic moment of $0.75\,\mu_B$, and with an incommensurate wave vector $\boldsymbol{q} = (0.5, 0.5, 0.297)$ helical in the c-axis direction [62]. The ^{115}In nuclear quadrupole resonance (NQR) measurements suggested that in the ordered state the magnetic moments lie strictly in the $CeIn_3$ plane and a spiral spin structure is realized along the c-axis direction. Figures 1.9(a) and (b) show the temperature dependence of resistivity in $CeRhIn_5$ single crystal. At ambient pressure, ρ decreases monotonically with decreasing temperature. Above 1.3 GPa, it shows maximum value around 30 K which is the typical temperature dependence of Kondo lattice systems.

T_N is increased with increasing pressure p and shows a maximum at $p \sim 1\,GPa$ where superconductivity appears. At higher pressures, the AFM phase and the superconducting phase coexist, and T_c increases with pressure but T_N decreases. Above the pressure p^* where $T_c = T_N$, the antiferromagnetic order suddenly disappears and the pressure-induced transition to superconductivity appears to be first order, thus avoiding a QCP. On the other hand, apparent deviations from Fermi liquid behavior have been observed in $\rho(T)$ over a wide temperature and pressure range (Figure 1.9(d)). Furthermore, there are a sharp change in the dHvA frequencies and a dramatic increase in the effective quasiparticle mass [36] under pressure. As shown in Figure 1.10, the dHvA frequency is unchanged even when it exceeds p^* but it shows a drastic change at p_c where T_N is extrapolated to the zero temperature on the $p - T$ phase diagram. The effective cyclotron mass m^* begins to gradually increase above the pressure at which superconductivity begins to appear and diverges with approaching p_c, and then, it gradually decreases above p_c. These results indicate that the critical pressure is p_c, not p^*. Later, a quantum critical line between a phase of coexistence and a purely superconducting phase was revealed [33, 64]. This line ends at a tetracritical point, which separate four distinct phases, namely, thee pure AFM phase , the coexistence phase of AFM order superconductivity, pure superconducting phase, and paramagnetic phase, under a magnetic field.

Regarding the gap symmetry, field-angle-dependent specific heat measurements under pressure have been reported [64]. The measurements were performed in the coexistence of the AFM and superconducting phase (at 1.45 GPa which is below p^*) and the pure superconducting phase (at 2.3 GPa). At both pressures, in-plane fourfold modulation and out-of-plane twofold modulation have been seen, which are consistent with the d-wave gap symmetry being the same as that of $CeCoIn_5$.

Figure 1.11 shows the temperature dependence of the upper critical field H_{c2} at $p = 2.45\,GPa$ [65]. As $CeRhIn_5$ has a quasi-2D cylindrical Fermi surface similar to that of $CeCoIn_5$, it is expected that H_{c2}^{ab} will be higher, but actually H_{c2}^{c}. This reversed anisotropy is also different from H_{c2} in the coexistence phase below, where p^*, $H_{c2}^{c} < H_{c2}^{ab}$ is preserved [64].

Figure 1.12 shows the field-temperature phase diagram of $CeRhIn_5$ determined by heat capacity measurements and dHvA oscillations. The AFM transition tempera-

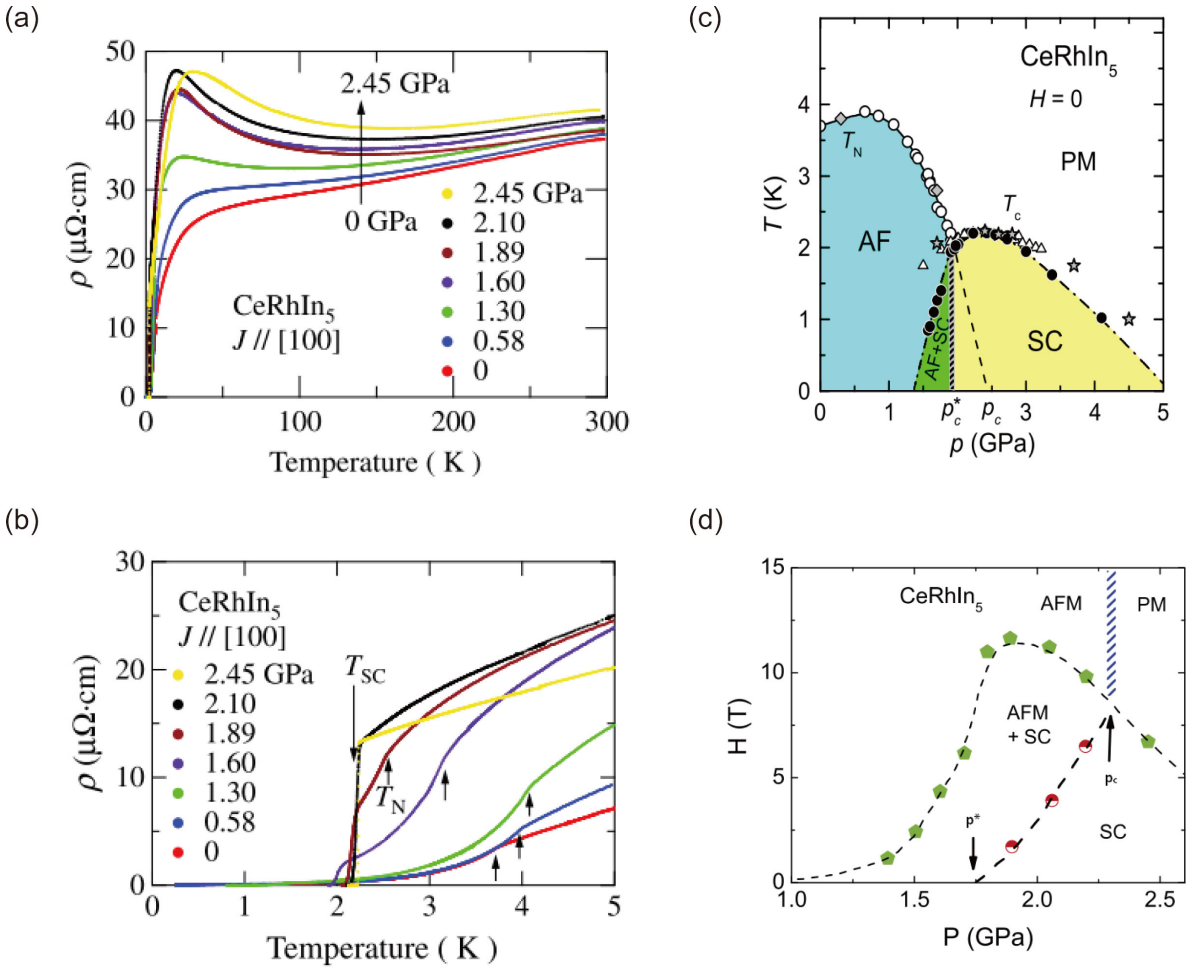

Figure 1.9: Temperature dependence of resistivity of $CeRhIn_5$ for different pressures [63]. $P-T$ phase diagram of $CeRhIn_5$ in zero magnetic field from ac calorimetry (circles), ac susceptibility (triangles), and resistivity (diamonds for T_N, and stars for T_c). Below p^*, both antiferromagnetic (AF) and superconducting (SC) phases coexist. At p^* the AF is suppressed suddenly before the QCP at p_c is reached under pressure. Above p^*, a purely superconducting phase appears in a zero magnetic field. The dashed line is a smooth extrapolation of T_N [33]. (d) Field-temperature phase diagram of $CeRhIn_5$ at zero temperature obtained from extrapolation of data to $T = 0$. The tetracritical point at p_c separates four distinct phases. Figure after [59].

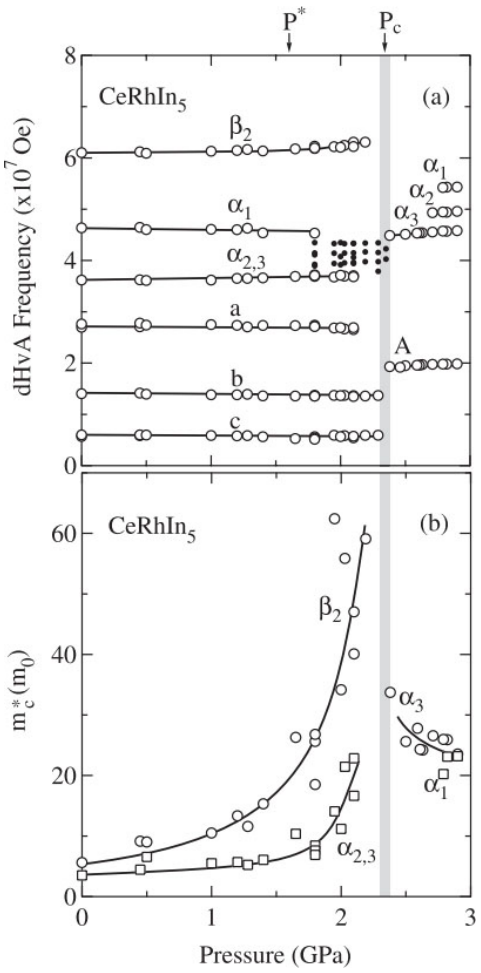

Figure 1.10: Pressure dependence of dHvA frequency and cyclotron mass in $CeRhIn_5$. [36]

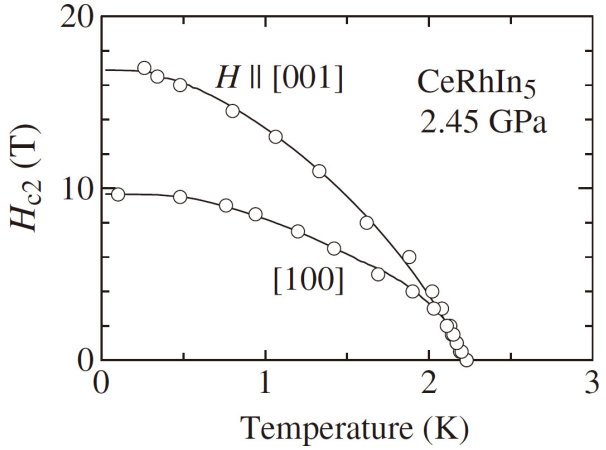

Figure 1.11: Temperature dependence of upper critical field in $CeRhIn_5$ at 2.45 GPa [63]

ture reflects the anisotropy of the crystal field at low magnetic fields and has a large anisotropy in the a-axis direction and the c-axis direction. It is known that there is a field-induced QCP at $H_{c0} = 50\,\mathrm{T}$ under high magnetic fields, on the a- and c-axes. Focusing on the magnetic field dependence of T_N near QCP, $T_\mathrm{N} \sim (H_{c0} - H)^{2/3}$ was observed, which is the expected behavior for 3D spin fluctuations. The change in the shape of the Fermi surface occurs at a lower magnetic field B^*. Field evolution of the Fermi surface is obtained from the fast Fourier transformation of the dHvA oscillations over different field windows. As shown in Figure 1.13(a)-(c), the dHvA spectra of $CeRhIn_5$ at $B < B^*$ and at $B > B^*$ are quite different. At low fields, the dHvA frequency of $CeRhIn_5$ is very similar to that of $LaRhIn_5$. On the other hand, dHvA frequency appearing above B^* is in good agreement with that of $CeCoIn_5$. This result demonstrates that the reconstruction of the Fermi surface occurs in B^*, and that the electronic structure changes from a small Fermi surface with localized f-electrons to a large Fermi surface with itinerant f-electrons. This anomaly in B^* is also shown in the Hall resistivity measurements [66]. The significant decrease in the Hall coefficient at B^* corresponds to a large change in the number of carriers and appears to reflect the reconstruction of the Fermi surface at B^*. Recently, a large anisotropy in the in-plane electrical resistance in the AFM phase above B^* has been reported, and this is considered to be a unique electronic phase that seems to be a spin nematic phase [67].

The QCP induced by magnetic field is qualitatively different from that induced by pressure where Fermi surface reconstruction occurs at QCP. The connection between these different types of QCPs remains an open question.

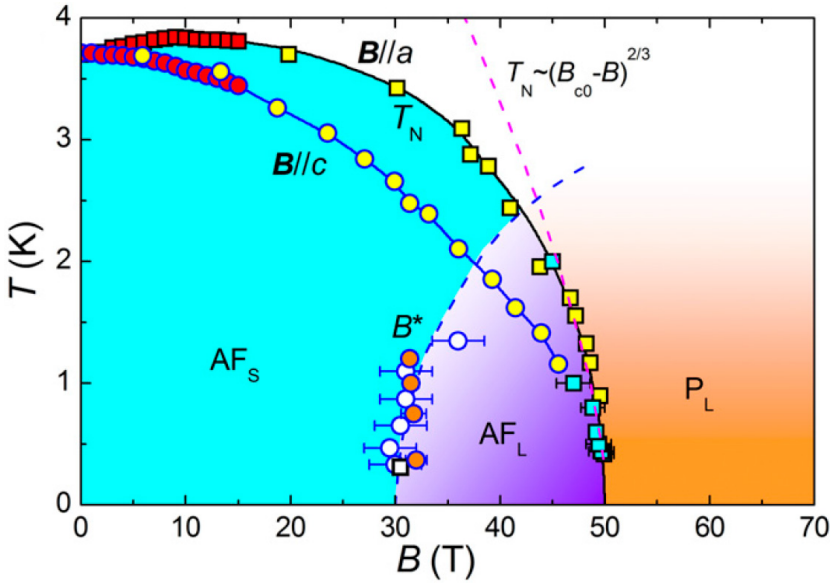

Figure 1.12: Field-temperature phase diagram of $CeRhIn_5$ for the field along a- and c-axes. AF and P denote antiferromagnetism and paramagnetism, respectively, while the subscript denotes a small (S) or large (L) Fermi surface. [66]

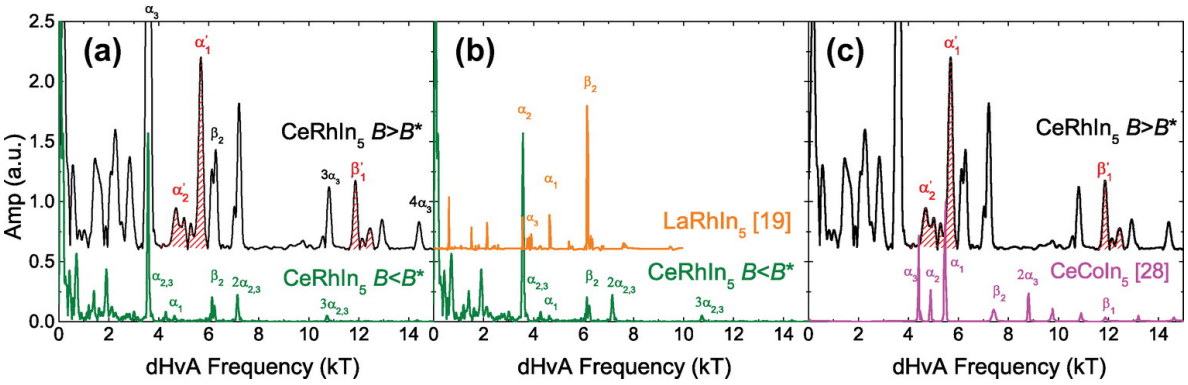

Figure 1.13: A comparison between the fast Fourier transforms of the dHvA spectra of (a) $CeRhIn_5$ at $B > B^*$ and $B < B^*$, (b) $CeRhIn_5$ at $B < B^*$ and $LaRhIn_5$, $CeRhIn_5$ at $B > B*$ and $CeCoIn_5$. [68]

1.3.4 $CeIn_3$

$CeIn_3$ has a cubic $AuCu_3$-type structure with a 3D Fermi surface as shown in Figure 1.14(a). At ambient pressure, this compound undergoes an AFM transition at $T_N = 10.1\,K$ with an ordered magnetic moment of $0.48\,\mu_B$ and a commensurate wave vector $\boldsymbol{q} = (0.5, 0.5, 0.5)$ [69]. Figure 1.14(b) shows the temperature dependence of resistivity in the $CeIn_3$ single crystal at several pressures [70]. With decreasing temperature, $\rho(T)$ increases below $\sim 150\,K$ due to the Kondo scattering but then begins to decrease due to strong c-f hybridization between f-electrons and conduction band electrons, leading to a narrow f-electron band at the Fermi level. The Kondo coherence temperature T_{coh}, at which the formation of heavy-fermion occurs, is estimated from the maximum in $\rho(T)$. With increasing pressure, T_{coh} increases, reflecting further c-f hybridization, which is typical for Ce compounds. The kink accompanied by the AFM transition appears at the low-temperature part of resistivity, indicated by arrows. At ambient pressure, the kink is sharp, but under pressure it gradually becomes smooth.

Figure 1.15 (a) shows the p-T phase diagram of $CeIn_3$ [70]. A dome-like superconducting phase appears with $T_c^{max} = 0.2\,K$ around the critical pressure $p_c = 2.6\,GPa$. The superconducting transitions are clearly seen in the low-temperature part of resistivities. The normal state of the resistivity near p_c shows non-Fermi liquid behavior. Figure 1.15 shows the pressure dependence of the exponent n (upper frame) and the prefactor A_n (lower frame) of the resistivity $\rho = \rho_0 + A_n T^n$. In the case of a Fermi liquid, n is 2, and it abruptly drops to ~ 1.6 around p_c. Above p_c, the value of $n = 2$ is recovered. A_2 diverges toward p_c in proportion to the power of 1.2. In heavy-fermion systems, the relationship $m^* = \sqrt{A_2}$ is preserved, indicating the enhancement of m^* toward a AFM QCP. If considering the isotropic Fermi surface, the effective mass m^* near p_c is estimated as $170m_0$, which is about 3 times larger than m^* at ambient pressure as determined by the specific heat.

The superconductivity in $CeIn_3$ is believed to be mediated by these magnetic fluctuations [1]. The normal state resistivity near the critical pressure shows non-Fermi liquid behavior [70]. Figure 1.15 (c) shows the temperature dependence of the upper

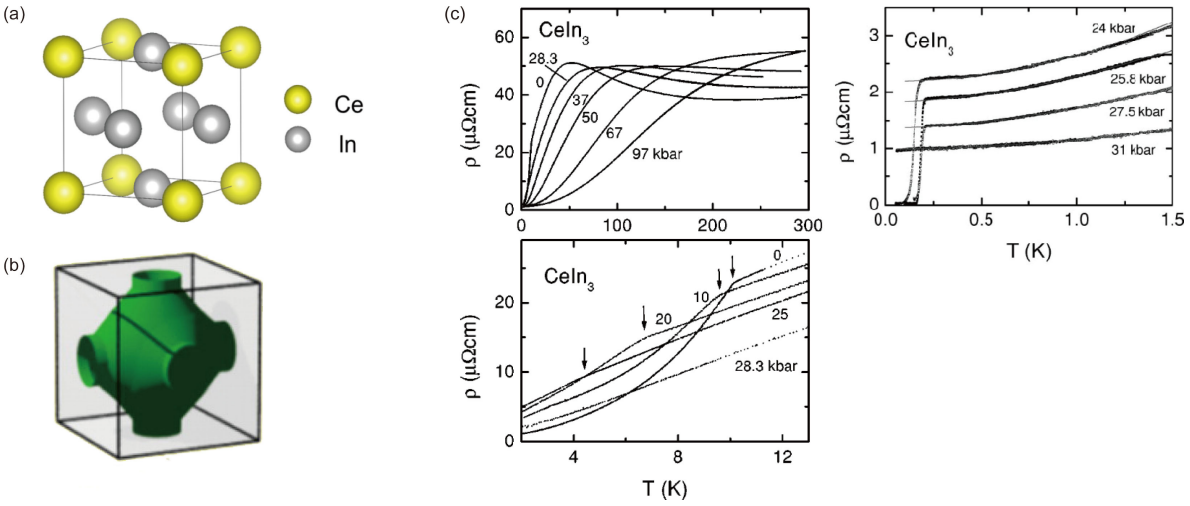

Figure 1.14: (a) A cubic structure of $CeIn_3$. (b) Fermi surface sheet from tight binding calculations in the paramagnetic phase of $CeIn_3$. (c) Temperature dependence of resistivity of $CeIn_3$ for different pressures.

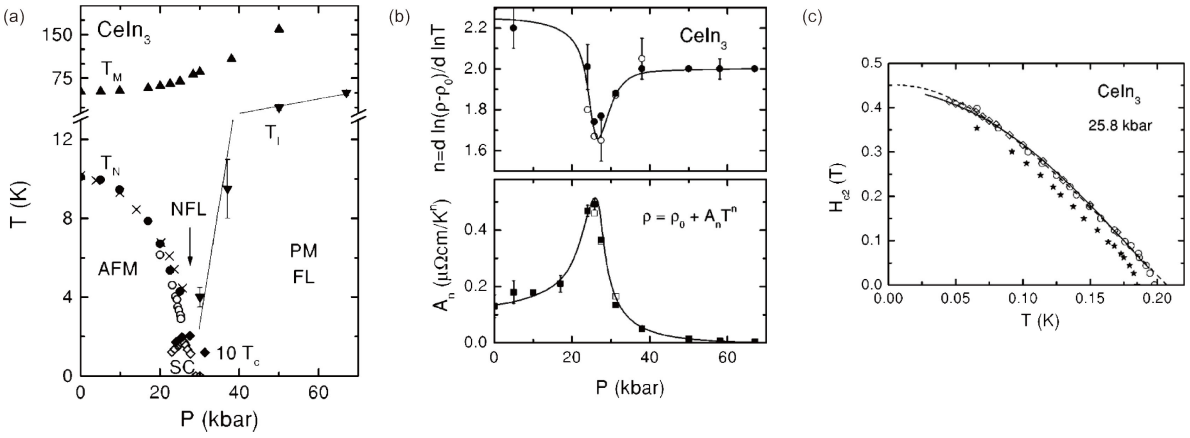

Figure 1.15: (a) Phase diagram of $CeIn_3$. T_M indicates the temperature of the maximum of the resistivity, T_N the Néel temperature, and T_l the crossover temperature to the Fermi-liquid regime. The superconducting transition temperature T_c is scaled by a factor of 10. (b) Pressure dependence of exponent n (upper frame) and prefactor A_n (lower frame) of the resistivity [70]. Both show anomalous behavior near the critical pressure. The lines are to guide the eye. (c) Upper critical field for $p = 2.58\,\mathrm{GPa}$. The circles denote $H_{c2}(T)$ determined by a temperature sweep at a constant field. The stars represent $H_{c2}(T)$ determined by the midpoint criterion.

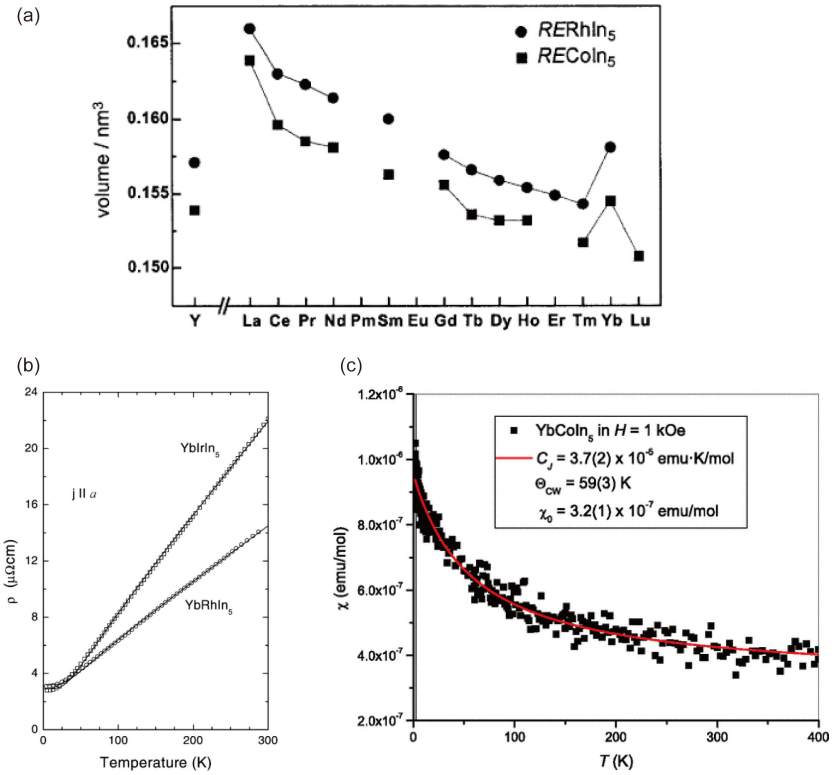

Figure 1.16: (a) Cell volumes of RECoIn$_5$ and RERhIn$_5$ compounds [71]. (b) Temperature dependence of resistivity of YbRhIn$_5$. Adapted from [73, 74]. (c) Magnetic susceptibility of YbCoIn$_5$, along with a Curie–Weiss fit [72].

critical field H_{c2} under a pressure of CeIn$_3$ [70]. From the slope of H_{c2} near T_c, the superconducting coherence length ξ_0 and Fermi velocity v_F are found to be $\xi_0 \approx 300\,\text{Å}$ and $v_F \approx 4500\,\text{m/s}$. The coherence length is much shorter than the mean free path $l_e \approx 2000\,\text{Å}$, indicating that CeIn$_3$ is in the clean limit.

1.3.5 YbCoIn$_5$ and YbRhIn$_5$

YbCoIn$_5$ and YbRhIn$_5$ have the same crystal structure as that of CeCoIn$_5$ with alternating layers of YbIn$_3$ and CoIn$_2$ or RhIn$_2$ stacked along the c-axis [71]. The lattice constants a and c are 4.533 Å and 7.413 Å for YbCoIn$_5$ and 4.595 Å and 7.442 Å for YbRhIn$_5$ [71, 72]. As shown in Figure 1.16(a), the cell volume decreases monotonically from La to Lu in RECoIn$_5$ and RERhIn$_5$, where RE is a rare earth element. Because Yb systems show a positive deviation from these trends, it has been pointed out that Yb ions are intermediate-valent or divalent [71]. In X-ray absorption near-edge structure measurements, it was found that the valence of the Yb ion is approximately 2.3, which is larger than that of divalence, but is still close to the nonmagnetic f^{14} configuration [72].

The electronic and magnetic properties of YbCoIn$_5$ and YbRhIn$_5$ are quite similar and trivial. Figure 1.16 depicts the temperature dependence of the resistivity of

$YbCoIn_5$ and $YbRhIn_5$, showing good metallic behavior with a residual resistivity ratio of 5–50 [73, 74]. In $YbCoIn_5$, the magnetic susceptibility $\chi(T)$ exhibits non-magnetic behavior as shown in Figure 1.16. The estimated Sommerfeld coefficient of the specific heat, $\gamma_0 = 11.6$ mJmol^{-1}K^{-2}, is more than 20 times smaller that of $CeCoIn_5$, indicating weak correlations in $YbCoIn_5$. The data for χ and ρ suggest that $YbCoIn_5$ and $YbRhIn_5$ are non-magnetic conventional metals.

1.4 Heavy-fermion superlattices

In bulk heavy-fermion systems, the electronic states are essentially 3D. In recent years, with technical development of the molecular beam epitaxy (MBE) technique, it has become possible to fabricate thin films of heavy-fermion compounds and superlattices that have an alternating layered structure of heavy-fermion compounds and conventional metals. As a result, we have succeeded in confining the heavy electrons within two dimensions, and we have observed many characteristic behaviors not seen in 3D systems [75–77]. In this section, we introduce the study of three kinds of heavy-fermion superlattices, namely, $CeIn_3/LaIn_3$ [75], $CeCoIn_5/YbCoIn_5$ [76], and $CeRhIn_5/YbRhIn_5$ superlattices [77].

1.4.1 $CeIn_3/LaIn_3$ superlattices

With reducing spatial dimensions, magnetic order is often suppressed because of quantum fluctuations. Therefore, the dimensionality can be regarded as a tuning parameter for quantum criticality. To control the dimensionality of the magnetism in Kondo lattice, Shishido *et al.* fabricated heavy-fermion superlattice $CeIn_3/LaIn_3$ consisting of heavy-fermion AFM metal $CeIn_3$ and conventional metal $LaIn_3$ [75]. The researchers developed a state-of-the-art MBE technique and, using a MgF_2 substrate, they successfully fabricated heavy-fermion superlattices for the first time. Figures 1.17(a), (b), and (c) show the high-resolution cross-sectional transmission electron microscopy (TEM) image, diffraction pattern of the electron beam X-ray diffraction, and reflection high-energy electron diffraction (RHEED) image, respectively, of $CeIn_3/LaIn_3$ superlattices with alternating layers of n unit-cell-thick (UCT) $CeIn_3$ and 4-UCT $LaIn_3$. These results demonstrate that superlattice structures have clear interfaces without discernible interdiffusion and precisely controlled block layer (BL) thickness.

Figures 1.18(a) and (b) show the temperature dependence of the in-plane resistivity normalized by its value at 10 K, $\rho(T)/\rho(10\,\mathrm{K})$, and the Hall coefficient R_H for $\boldsymbol{H} \parallel c$, respectively, in $CeIn_3(n)/LaIn_3(4)$ superlattice. For comparison, $\rho(T)$ for the $CeIn_3$ thin film and R_H for bulk $CeIn_3$ are displayed. The peak temperatures coincide well with the temperature at which $R_H(T)$ exhibits cusp-like minima. These observations indicate that T_N is suppressed with reducing $CeIn_3$ BL thickness, resulting in the disappearance of the AFM order at $n \sim 2$. To determine whether the resistivity obeys the Fermi-liquid expression, $\rho(T) = \rho_0 + AT^2$, the group fitted the low-temperature part of the resistivity. Figure 1.18(c) depicts the thickness dependence of T_N and prefactor A, which is related to the effective mass m^* through the effective specific heat coefficient $\gamma_\mathrm{eff} \propto m^*$ and the

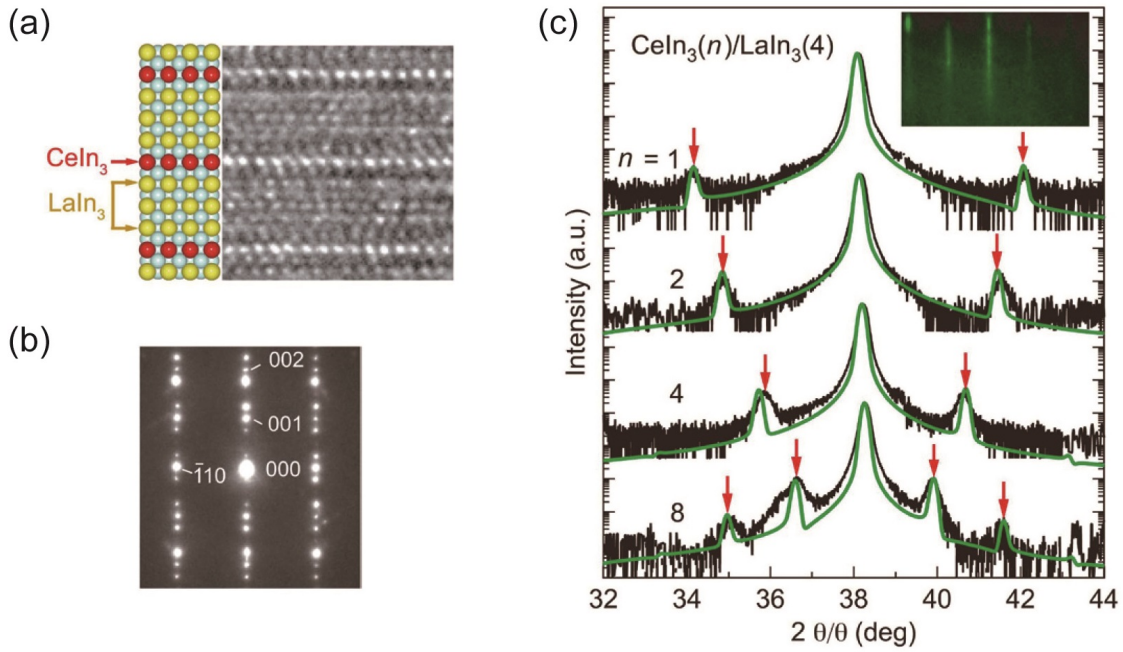

Figure 1.17: (a) High-resolution cross-sectional TEM image of the $CeIn_3(1)/LaIn_3(4)$ superlattice, which is with the designed superlattice structure shown in the left panel. (b) Diffraction pattern of the electron beam incident along the [1 1 0] direction. (c) X-ray diffraction patterns around (0 0 2) peak of the $CeIn_3(n)/LaIn_3(4)$ for $n = 1$, 2, 4, and 8. Green lines represent the step-model simulations ignoring the interface and layer-thick fluctuations. These simulations reproduce both the intensities and the position of the satellite peaks indicated by arrows. The RHEED image in the inset represents epitaxial growth.

Kadowaki–Woods Fermi liquid relation, $A/\gamma_{\rm eff} = 1 \times 10^{-5} \mu\Omega{\rm cm}\ ({\rm mJ/mole\ K})^{-2}$ [78]. Concomitant with the disappearance of $T_{\rm N}$ close to $n = 2$, the prefactor A was strikingly enhanced. It is natural to consider that the mass enhancement and deviation from the Fermi liquid behavior of the resistivity for the $n = 2$ superlattice are caused by the quantum critical fluctuations associated with the QCP in the vicinity of $n = 2$, implying dimensional control of the system toward an AFM QCP.

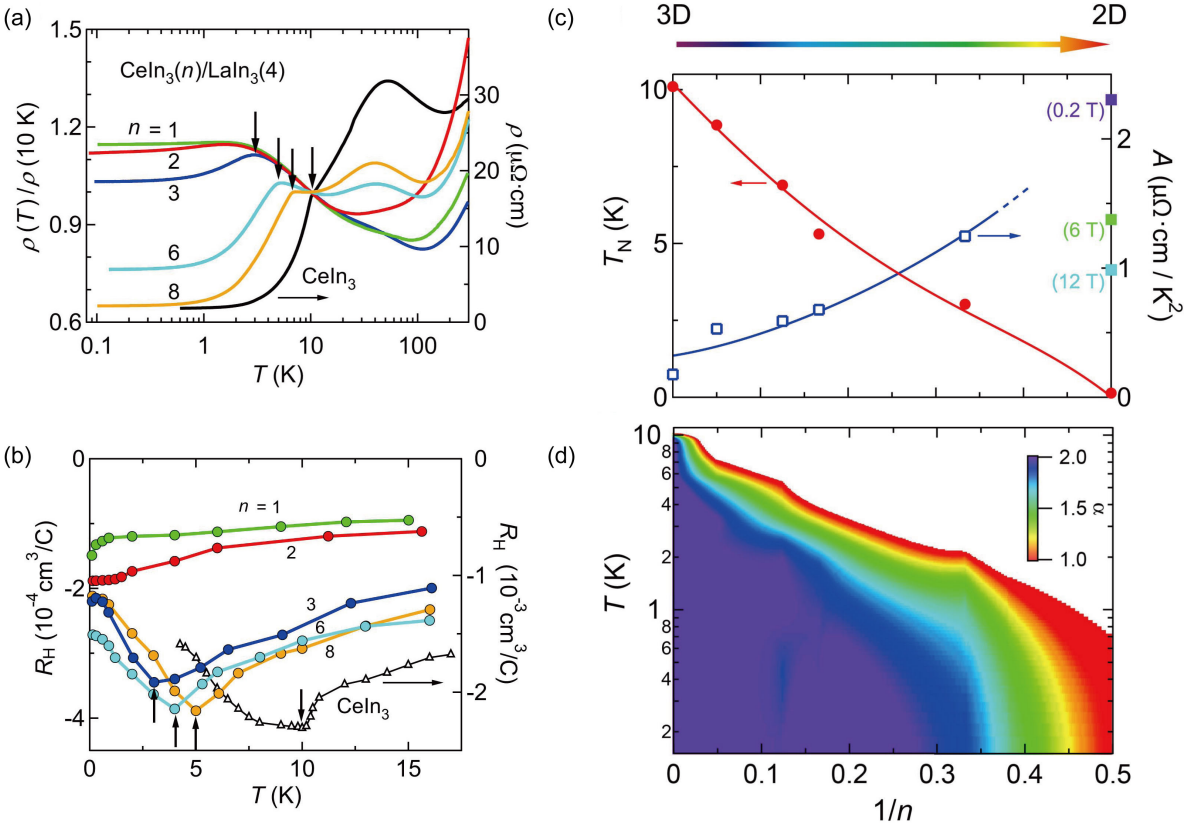

Figure 1.18: Transport properties in $CeIn_3/LaIn_3$ superlattices. (a) Temperature dependence of resistivity normalized by its value at 10 K, $\rho(T)/\rho(10\ {\rm K})$, in the $CeIn_3(n)/LaIn_3(4)$ superlattices for $n = 1$ (green), 2 (red), 3 (dark blue), 6 (light blue), and 8 (yellow). The $\rho(T)$ of the $CeIn_3$ thin film (black line, right axis) coincides well with the results for the bulk material. (b) Temperature dependence of Hall coefficient $R_{\rm H}$ for the superlattices (left axis) and for bulk $CeIn_3$ (right axis). Both $\rho(T)$ and $R_{\rm H}(T)$ show cusp-like behavior (arrows) for $n = 8$, 6, and 3 as well as for $CeIn_3$. [79] (c) Temperature versus dimensionality phase diagram. $T_{\rm N}$ (red circles) and Fermi liquid coefficient prefactor A (open blue squares) as a function of $1/n$. For $n = 2$, the A values were determined from $\rho(T)$ under magnetic fields (solid squares). The solid and dashed lines serve as visual guides. (d) Temperature and layer thickness evolution of the exponent α derived from the expression $\rho(T) = \rho_0 + AT^{\alpha}$. According to ref. [79]

Figure 1.18(d) depicts the temperature and layer thickness evolution of the exponent α derived from the expression $\rho(T) = \rho_0 + AT^{\alpha}$. The T-linear behavior for the $n = 2$

superlattice is consistent with scattering by fluctuations enhanced by the 2D-AFM QCP. This is in contrast to $CeIn_3$ single crystals, where $\alpha \sim$ of 1.6 which is close to $\alpha = 1.5$ expected near 3D AFM QCP. The researchers demonstrated that the dimensionality of the quantum criticality can be controlled by modulating the BL thickness. Their successful fabrication of heavy-fermion magnetic superlattices by MBE, paving the way for the study of 2D superconductivity in the vicinity of AFM QCP.

1.4.2 $CeCoIn_5/YbCoIn_5$ superlattices

2D AFM fluctuations are essentially important for *d*-wave superconductivity. However, in $CeCoIn_5$, all the electronic, magnetic, and superconducting properties are mostly 3D rather than 2D. Therefore, it is unclear whether superconductivity of $CeCoIn_5$ persists with the dimensionality reduction from 3D to 2D. To confine the *d*-wave superconducting state within a 2D Kondo lattice, Mizukami *et al.* fabricated superconducting superlattices of $CeCoIn_5/YbCoIn_5$ [76]. Figures 1.19(a) and (b) show the cross-sectional TEM image and X-ray diffraction of $CeCoIn_5(n)/YbCoIn_5(5)$ superlattices, respectively. These results demonstrate the clear interface between the Ce- and Yb- BL. As shown in Figure 1.19(c), a superconducting transition to zero resistance was observed for $n \geqq 3$ and a drop in the resistivity at low temperature for $n = 1$ and 2.

Figure 1.20(a) shows thee H-T phase diagram of the $CeCoIn_5/YbCoIn_5$ superlattice for $n = 3$, 5, and 7, compared with those of $CeCoIn_5$ single crystal. Despite the suppression of T_c, our-of-plane upper critical field $H_{c2\perp}$ of the superlattices remains comparable to that of single crystal $CeCoIn_5$. The inset of Figure 1.20(a) shows the anisotropy of the upper critical fields $H_{c2||}/H_{c2\perp}$. The anisotropy diverges on approaching T_c. This is in sharp contrast to the case involving $CeCoIn_5$ thin films, whose anisotropy is nearly temperature-independent up to T_c. The observed diverging anisotropy indicates that the superconducting electrons are confined in the 2D $CeCoIn_5$ BLs. The thickness of the $CeCoIn_5$ BL is comparable to the coherence length perpendicular to the layer. Thus, each 7-UCT $CeCoIn_5$ BL effectively behaves as a 2D superconductor. The most remarkable feature of this extremely 2D heavy-fermion superconductor is that the thickness reduction drastically enhances H_{c2}/T_c from the bulk value, as shown in Figure 1.20(b). At that time, the robustness of H_{c2} against the suppression of T_c in the superlattices was interpreted as enhancement of the superconducting pairing strength $2\Delta/k_{\mathrm{B}}T_c$ by two-dimensionalization. However, in 2012, Maruyama, Sigrist, and Yanase pointed out that the local inversion symmetry breaking at the interface of multilayer system also suppress the Pauli pair-breaking effect by Fermi surface splitting due to Rashba effect [80]. Go *et al.* performed additional experiments on $CeCoIn_5/YbCoIn_5$ superlattice with detailed analysis and pointed out that the Pauli pair-breaking mechanism was suppressed by Fermi surface splitting due to the Rashba effect [81]. Recently, Yamanaka *et al.* performed site-sensitive NMR measurements with detailed analysis of the spectra and demonstrated that it is possible to separate NMR signals from the interface and from those inside the layer [82]. They found that suppression of AFM magnetic fluctuations in $CeCoIn_5$ near the interface between the BLs of $CeCoIn_5$ and non-magnetic normal

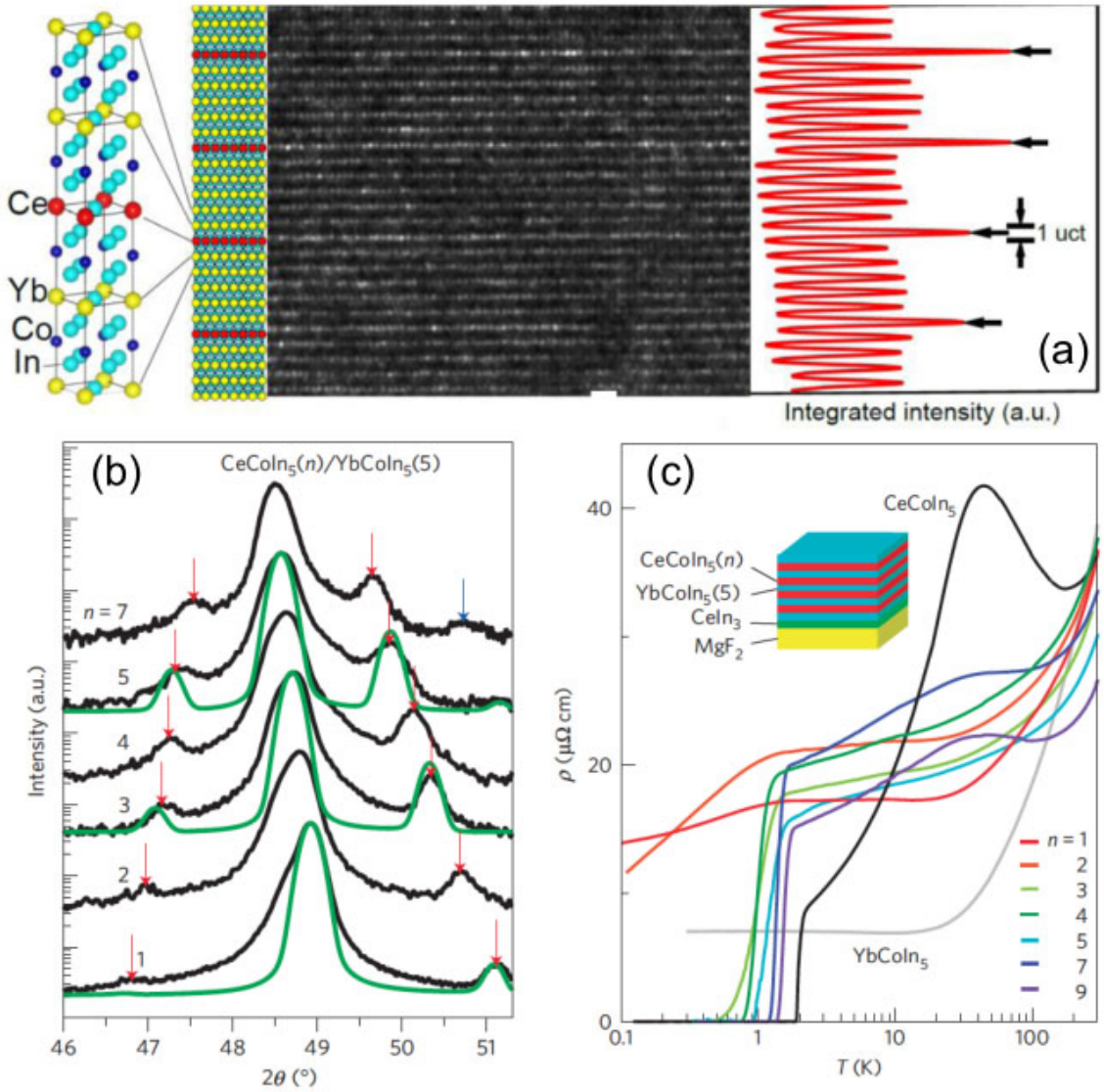

Figure 1.19: (a) Designed superlattice structure of $CeCoIn_5(1)/YbCoIn_5(5)$ and its high-resolution cross-sectional TEM image. The right panel shows the intensity integrated over the horizontal width of the image plotted against vertical position indicates a clear difference between the Ce and Yb layers, showing no discernible atomic interdiffusion between the neighboring Ce and Yb layers. (b) X-ray diffraction patterns for n = 1, 2, 3, 4, 5, and 7 superlattices that first exhibit the satellite peaks marked by the red arrows and, later, exhibit the satellite peak marked by the blue arrow. The positions of the satellite peaks and their asymmetric heights can be reproduced by step-model simulations, shown by the green lines by ignoring the interface and layer-thickness fluctuations. (c) Temperature dependence of electrical resistivity $\rho(T)$ for n = 1, 2, 3, 5, 7, and 9, compared with those of 300-nm-thick $CeCoIn_5$ and $YbCoIn_5$ single-crystalline thin films. Based on ref. [76].

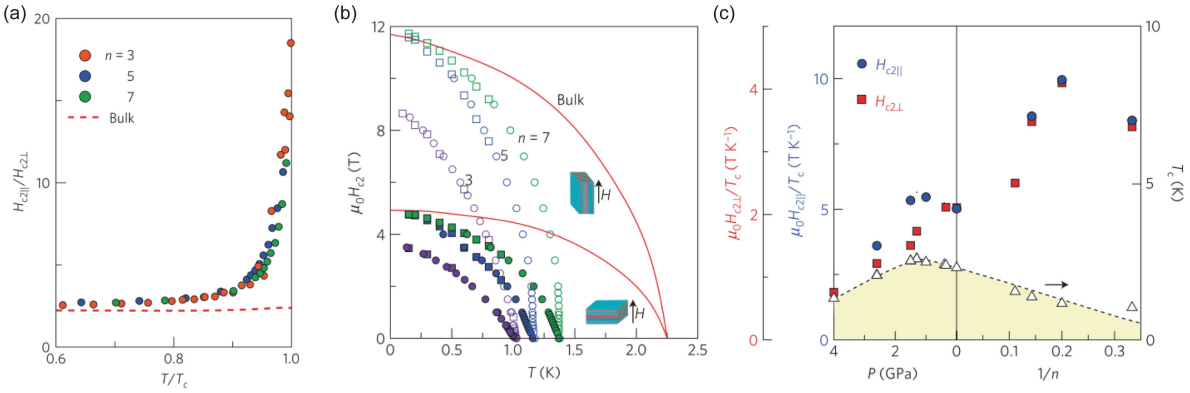

Figure 1.20: (a) Anisotropy of H_{c2}, $H_{c2||}/H_{c2\perp}$, as a function of reduced temperature T/T_c for $n = 3$, 5, and 7 superlattices and for the bulk $CeCoIn_5$. (b), (c) Superconducting transition temperature, T_c (open triangles), and reduced critical fields H_{c2}/T_c for parallel (filled blue circles) and perpendicular (filled red squares) magnetic fields as a function of dimensionality parameter $1/n$ (right panel). The pressure dependence of these quantities is also shown for comparison (left panel). Note the different scales for parallel (blue) and perpendicular (red) magnetic fields. From ref. [76]

$YbCoIn_5$.

1.4.3 $CeRhIn_5/YbRhIn_5$ superlattices

Next, we will look at another example of a heavy-fermion magnetic superlattice consisting of alternating layers of AFM metal $CeRhIn_5$ and non-magnetic normal metal $YbRhIn_5$ [77]. To control the dimensionality of the magnetism, $CeRhIn_5(n)/YbRhIn_5(7)$ superlattices were fabricated using the MBE technique. Figures 1.21(a) and (b) show ρ and $d\rho/dT$ at low temperatures for the thin film and the superlattices. For the $CeRhIn_5$ thin film, and $n = 9$, 5, and 4 superlattices, $d\rho/dT$ showed a pronounced peak structure as shown by arrows, indicating the AFM. For the $n = 3$ superlattice, on the other hand, the peak is very broad and thus the determination of T_N is ambiguous. The T_N of the $CeRhIn_5(n)/YbRhIn_5(5)$ superlattices systematically decreases with decreasing n. At the same time, the prefactor A is strikingly enhanced. In the vicinity of the QCP, quantum fluctuations cause enhancement of the effective mass or deviation from the Fermi liquid behavior. Thus, it was concluded that an QCP exists in the vicinity of $n = 3$ superlattice.

To investigate the nature of the QCP, the magnetoresistance and its anisotropy for the $n = 3$ superlattice was measured in an applied magnetic field. Figures 1.22(b) shows the evolution of α, the exponent in $\rho(T) = \rho_0 + AT^\alpha$, within the field-temperature (B-T) phase diagram of the $n = 3$ superlattice, for the magnetic field applied parallel to the ab plane and c axis, respectively. At $B_c \approx 1.2$ T for $\boldsymbol{B} \parallel ab$ and $B_c \approx 2$ T for $\boldsymbol{B} \parallel c$, non-Fermi liquid behavior ($\alpha \lesssim 1.5$) was observed down to the lowest temperatures and in a large extended field range at higher temperatures. For $B > B_c$, a broad crossover regime from the non-Fermi liquid state to the field-induced Fermi liquid state at a lower

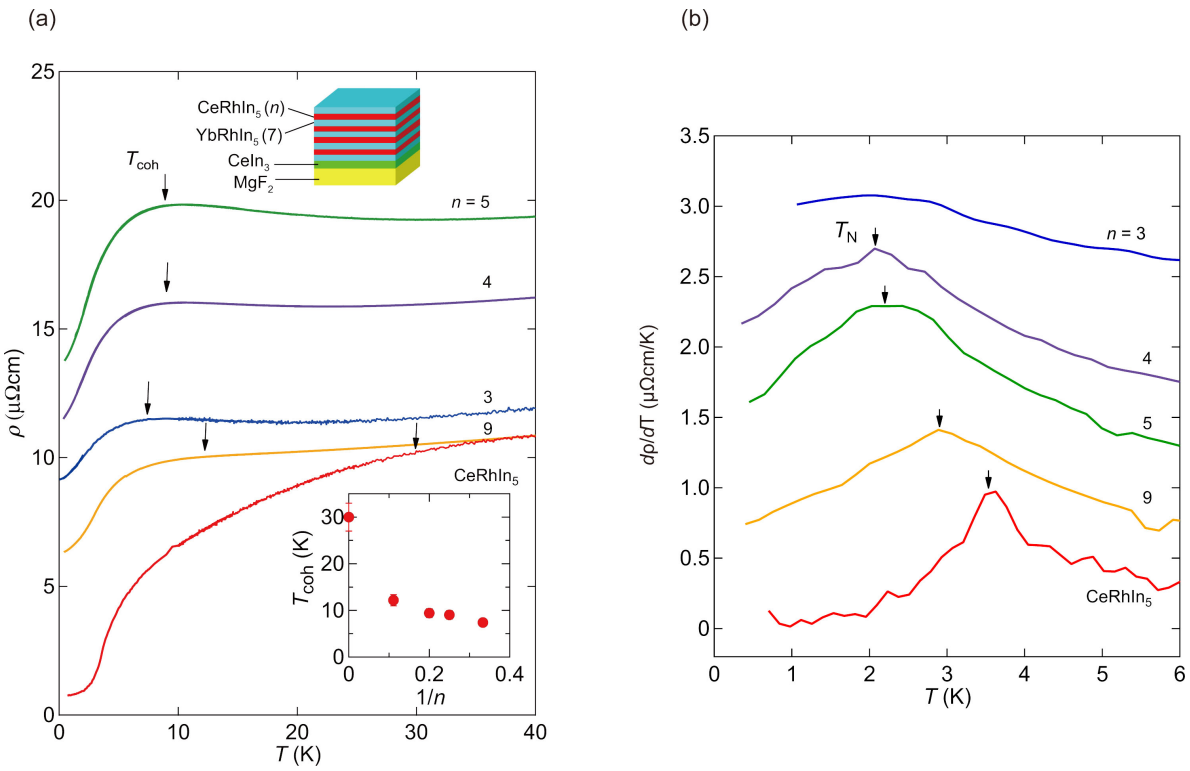

Figure 1.21: Transport properties in $CeRhIn_5/YbRhIn_5$ superlattices. (a) Temperature dependence of resistivity ρ for $CeRhIn_5$ thin film and $CeRhIn_5(n)/YbRhIn_5(7)$ superlattices. The arrows indicate the Kondo coherence temperature $T_{\rm coh}$. Insets: (top) Schematic representation of the superlattice. (bottom) $T_{\rm coh}$ as a function of $1/n$. (b) Temperature derivative of the resistivity, $d\rho/dT$, as a function of T for $CeRhIn_5$ thin film and $CeRhIn_5(n)/YbRhIn_5(7)$ superlattices. Arrows indicate the Néel temperature $T_{\rm N}$.

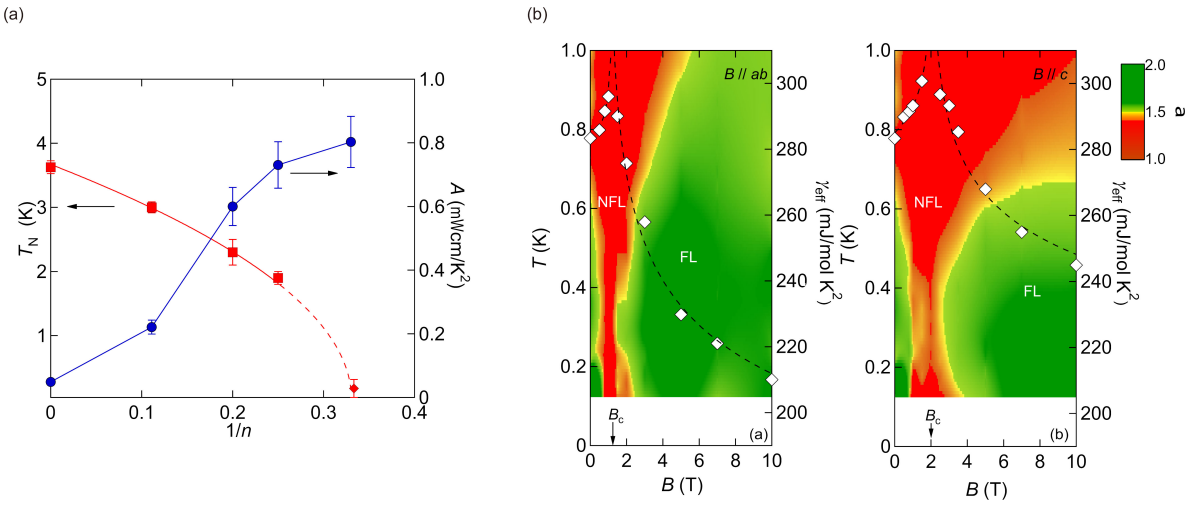

Figure 1.22: Tuning magnetic quantum criticality in $CeRhIn_5/YbRhIn_5$ superlattices. (a) The Néel temperature T_N (left axis) and Fermi liquid coefficient A derived from the expression $\rho = \rho_0 + AT^2$ (right axis) as a function of $1/n$. T_N for the $n = 3$ superlattice (diamond) is estimated by the temperature below which the Fermi liquid behavior is observed. (b) Temperature and magnetic field evolution of the exponent α derived from the expression $\rho(T) = \rho_0 + AT^\alpha$ in the $n = 3$ superlattice for $\boldsymbol{B} \parallel ab$ and $\boldsymbol{B} \parallel c$. The triangles represent the effective specific heat γ_{eff} estimated from the resistivity at the lowest temperatures assuming the T^2-dependent resistivity (right axis).

temperature was found to occur. Thus, the non-Fermi liquid behavior dominates over a fan-shaped region of the B-T phase for both field directions. The field dependence of γ_{eff} for the $n = 3$ superlattice estimated from the T^2-dependent resistivity in the Fermi liquid regime is also plotted in Figure 1.22(b). As the field approaches B_c from either side, γ_{eff} is rapidly enhanced. These results corroborate the emergence of a field-induced QCP at B_c. In bulk $CeRhIn_5$, the critical magnetic field B_{c0} where T_N is suppressed to zero temperature is about 50 T for both $B \parallel a$ and $B \parallel c$. The observed small B_c in the superlattice suggests that the Rashba spin-orbit interaction, arising from the local inversion symmetry breaking at the interface, plays an essential role in tuning the quantum criticality in the 2D Kondo lattice.

In the absence of inversion symmetry, an asymmetric potential gradient $\nabla V \parallel [001]$ yields an Rashba spin-orbit interaction $\alpha_R\, \boldsymbol{g}(\boldsymbol{k}) \cdot \boldsymbol{\sigma} \propto (\boldsymbol{k} \times \nabla V) \cdot \boldsymbol{\sigma}$, where $\boldsymbol{g}(\boldsymbol{k}) = (k_y, -k_x, 0)/k_F$, k_F is the Fermi wave number, and $\boldsymbol{\sigma}$ is the vector of Pauli matrices [83–85]. The Rashba interaction splits the Fermi surface into two sheets with different spin structures. The energy splitting is given by α_R, and the spin direction is tilted into the plane, rotating clockwise in one sheet and anticlockwise in the other. As the noncentrosymmetric interface layers occupy two-thirds of the $CeRhIn_5$ layers in the $n = 3$ superlattice, the local inversion symmetry breaking at the interfaces, which results in Rashba spin-orbit splitting of the Fermi surface, has a significant impact on the magnetic properties. In the presence of the local inversion symmetry breaking at the interfaces, the magnetic anisotropy is expected to be modified. For $\boldsymbol{B} \perp ab$, the Zeeman splitting

$h = g\mu_{\mathrm{B}} J_z B$ enters the energy $\varepsilon_{\mathbf{k}}$ of quasiparticles at the Fermi level quadratically alongside the Rashba interaction: $E_{\pm}(\boldsymbol{k}) = \varepsilon_{\boldsymbol{k}} \pm \sqrt{h^2 + \alpha_{\mathrm{R}}^2 |\boldsymbol{g}(\mathbf{k})|^2}$. Therefore, for weak fields ($h \ll \alpha_{\mathrm{R}}$, which is the case here), the Zeeman effect is quadratic rather than linear in field, and is therefore strongly suppressed. By contrast, for in-plane field $\boldsymbol{B} \parallel ab$, there is a component of $\boldsymbol{B}$ parallel to the Rashba-induced spin $\boldsymbol{g}(\boldsymbol{k})$, and the Zeeman effect is stronger. Therefore, the magnetic susceptibility for $\boldsymbol{B} \perp ab$ is expected to be suppressed more strongly than for $\boldsymbol{B} \parallel ab$. A theoretical evaluation showed that the anisotropy ratio of the magnetic susceptibility, χ_c/χ_{ab}, is $\chi_c/\chi_{ab} \sim (\chi_c/\chi_{ab})_{\mathrm{bulk}} \times 12(\delta^2 + \mathcal{O}(\delta^3))$, where $\delta = h/\alpha_{\mathrm{R}}$. The realistic values using the Rashba interaction and material parameters of $CeRhIn_5$ lead to an estimation of δ in the range $(0.02 - 0.1)$ for field $B = 1$ T, yielding an anisotropy ratio of $1/100 \lesssim \chi_c/\chi_{ab} \lesssim 1/10$. This can be explained by the fact that the anisotropy of the upper critical field is opposite to what is expected from the magnetic susceptibility in bulk $CeRhIn_5$. These results indicate that the Rashba spin-orbit interaction arising from the inversion symmetry breaking at the interface plays a key role in tuning the quantum criticality in the 2D Kondo lattice.

Chapter 2

Purpose of this study

As explained in the previous chapter, artificially engineered superlattices of heavy-fermion compounds are particularly suitable systems to study the interplay between the 2D unconventional superconductivity and magnetically ordered- or conventional metallic-states through the atomic interface in strongly correlated materials. The basics of the fabrication using the state-of-the-art MBE technique and characterization of heavy-fermion superlattices will be described in the following chapter.

In this thesis, we introduce new strategies for controlling unconventional superconductivity by fabricating two kinds of heavy-fermion superlattices, namely the tricolor superlattices of $YbCoIn_5/CeCoIn_5/YbRhIn_5$, and the hybrid superlattices of $CeCoIn_5/CeRhIn_5$ and $CeCoIn_5/CeIn_3$. The first is the noncentrosymmetic (tricolor) superlattice, in which the *d*-wave superconductor $CeCoIn_5$ is sandwiched by two different nonmagnetic metals, $YbCoIn_5$ and $YbRhIn_5$. In Chapter 4, to study the effect of global inversion symmetry breaking on unconventional superconductivity, we will provide a brief introduction, experimental details, and the results and discussion. Based on the detailed discussion of the temperature dependence of the upper critical field, we will demonstrate that the magnitude of the Rashba effect can be tuned by the thickness of the superconducting layers. We will also show a possible emergence of the exotic superconducting state inherent in noncentrosymmetric superconductors.

The second is the hybrid superlattice consisting of alternating atomic layers of *d*-wave superconductor $CeCoIn_5$ and AFM metal $CeRhIn_5$, in which the AFM order can be suppressed by applying pressure. We developed high-pressure measurements for epitaxial thin films and investigated the effect of pressure on heavy-fermion thin films and superlattices. We also performed low-temperature resistivity measurements under a rotated magnetic field. In Chapter 5, we will provide a brief introduction, experimental details, and results and discussion on hybrid superlattices of $CeCoIn_5/CeRhIn_5$. We also studied another kind of hybrid superlattices consisting of alternating atomic layers of $CeCoIn_5$ and AFM metal $CeIn_3$, in which the AFM order can be suppressed by applying pressure, similar to cases involving $CeRhIn_5$. The details of the fabrication and characterization of $CeCoIn_5/CeIn_3$ hybrid superlattices, and results and discussion, along with comparison with $CeCoIn_5/CeRhIn_5$, will be presented in Chapter 6.

We will conclude this thesis in Chapter 7 by summarizing the findings of this work.

Chapter 3

Experimental methods

In this study, heavy-fermion superlattices were fabricated using a molecular beam epitaxy (MBE) technique. The samples were characterized using reflection high-energy electron diffraction (RHEED), atomic force microscopy (AFM), X-ray diffraction (XRD), energy-dispersive X-ray spectroscopy (EDX), and transmission electron microscopy (TEM) and electron energy loss spectroscopy (EELS). To clarify the transport properties, low-temperature resistivity measurements were performed under hydrostatic pressure applied using a piston-cylinder pressure cell. In this chapter, we will introduce these techniques.

3.1 Molecular beam epitaxy (MBE)

MBE is an evaporation technique used to achieve epitaxial growth under ultra-high-vacuum (UHV) conditions ($< 10^{-7}$ Pa). Because, under UHV conditions, the mean free path of the evaporated gas molecules is long, the aligned gas molecular beam reach the substrate surface without colliding with other molecules. The effects of residual gas can also be minimized, which enables us to produce high-purity thin films. As a characteristic feature of MBE, the crystal growth rate is slow and the film thickness can be precisely controlled. In addition, when crystal growth is monitored *in situ* by RHEED, the flux can be adjusted by the feedback function. Because of its precise controllability, MBE is widely used for eptaxial growth for semiconductor thin films and heterostructures.

3.1.1 Knudsen cell

The molecular beam flux J [cm^{-2}sec^{-1}] is given by the following equation.

$$J = \frac{A}{\pi L^2} \frac{p \cos\theta}{(2\pi m k_B T)^{1/2}} \tag{3.1}$$

where p is the equilibrium vapour pressure in the cell, m is the mass of the molecule, k_{B} is the Boltzmann constant, T is the absolute temperature, A is the area of the cell outlet, L is the distance between the cell outlet and substrate, and θ is the angle between

the molecular beam and substrate. Figure 3.1 shows the temperature dependence of the vapor pressure of typical materials used in MBE. For example, the cell diameter is 1 cm, $L = 30$ cm, the material is Ce, and when the cell temperature $T = 1200$ °C, $p = 1.68 \times 10^{-4}$ Pa and the flux is 8.27×10^{15} atoms/cm^{2}s. In reality, the flux changes depending on the shape of the cell aperture and the crucible, and the amount of the atomic element in the crucible. Therefore, when determining the growth rate and composition ratio accurately, we determine the temperature dependence of the flux for each MBE system using a crystal rate monitor installed near the substrate holder in advance.

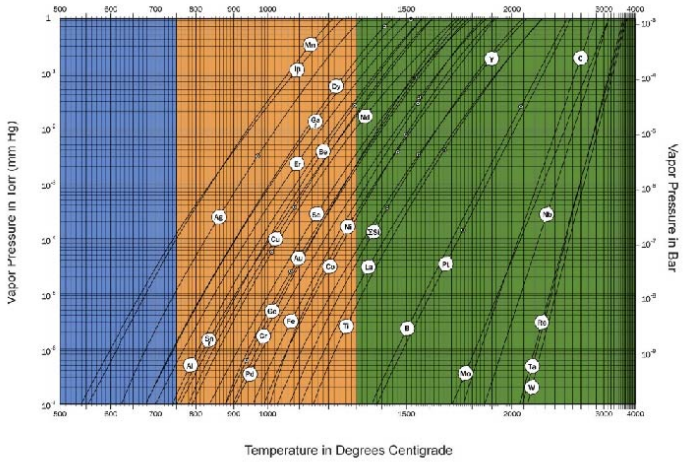

Figure 3.1: Temperature dependence of the vapour pressure typically used in MBE (adopted from [86]).

The MBE machine used in this study is equipped with four Knudsen cells, as shown in Figure 3.2. A Knudsen cell is composed of a carbon heater, crucible, shutter, and various structural components. A thermocouple is placed under the crucible. To control and adjust the deposition rate of the molecular beam, each Knudsen cell employs a specific Proportional-Integral-Differential (PID) temperature controller. Because rare-earth elements are highly reactive, the material choice for the crucible is crucial. We used crucibles made of tantalum (Ta), molybdenum (Mo), beryllium oxide (BeO), and silicon carbide (SiC) for the cerium, ytterbium, cobalt, and indium, respectively. The manufacturer and purity of each element are listed in Table 3.1. We used a shutter placed in front of the crucible to control the on/off mechanism of the molecular beam. To control precisely the chemical composition of a deposited film, the shutters were controlled using a computer, which enabled synchronized control of several shutters simultaneously. The typical crucible temperatures during growth were 1500°C, 420°C, 1300°C, and 870°C for Ce, Yb, Co, and In, respectively.

Table 3.1: Manufacturers and levels of purity of elements used in this study.

Element	Purity(%)	Manufacturer
Ce	99.9	Rare Metallic
Yb	99.9	Rare Metallic
Co	99.99	Rare Metallic
Rh	99.99	Rare Metallic
In	99.9999	Furuuchi Chemical

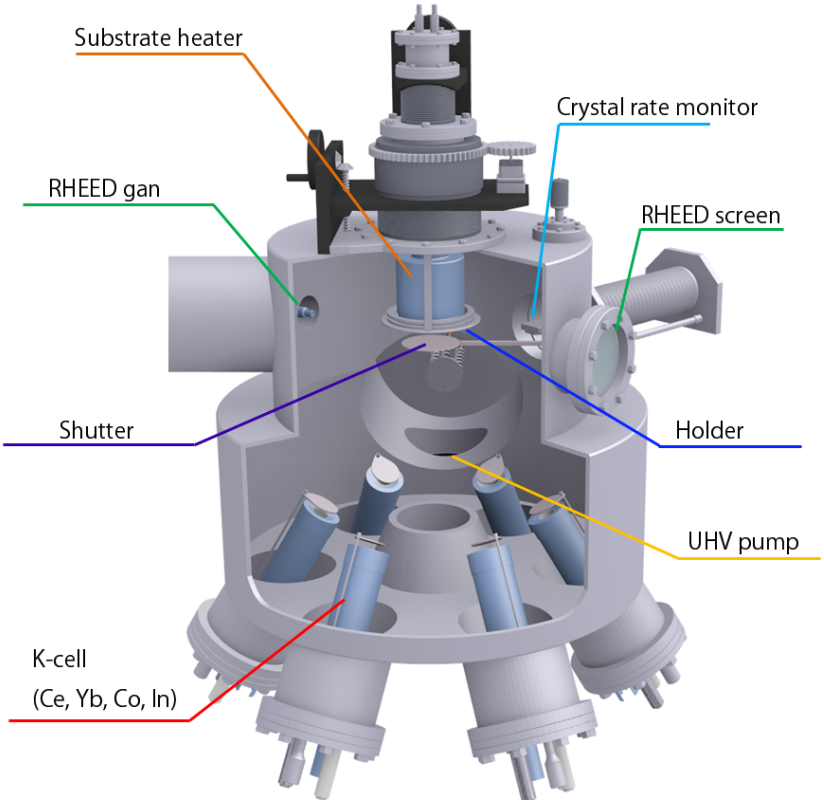

Figure 3.2: Schematic of an MBE machine [87].

3.1.2 Crystal rate monitor

A crystal rate monitor is composed of a thin slice of quartz with gold thin films deposited on both sides. It vibrates at a certain frequency when the ac electronic field is applied to the electrode. The frequency is determined by the thickness of the crystal and is changed when materials are deposited on the crystal. The relationship between a change of frequency Δf and the amount of stuck material Δm is described by the following equation.

$$\Delta f = -\frac{2f_0^2}{A\sqrt{\rho_Q \mu_Q}}\Delta m \tag{3.2}$$

where f_0 is a oscillation frequency of bare crystal, ρ_Q is the density of the crystal, μ_Q is the elastic modulus of the crystal, and A is the area of the gold films deposited on the crystal. When the mass of the stuck material increases, the frequency of the crystal decreases. We can know the deposition rate by monitoring the frequency of the crystal. We used a gold-coated quartz crystal with a resonance frequency of 6 MHz (INFICON, 008-010-G10) and SQC-300 rate controller. Typical growth speed was 0.1–0.2 Å/s for our experiments.

3.1.3 Comparison of thin film growth techniques

Several studies have been conducted on $CeCoIn_5$ heavy-fermion thin films using MBE [88–90], sputtering [91] and pulsed laser deposition (PLD) [92, 93]. Table 3.2 summarizes the techniques and results of previous studies.

Although the superconducting films of $CeCoIn_5$, which showed zero resistivity, were obtained using any of the aforementioned techniques, the quality varies depending on the technique. In the film prepared by sputtering, CeO_2 inclusions of various orientations were detected by XRD. In the film prepared by PLD, in addition to the desired $CeCoIn_5$ $(0\,0\,l)$, additional orientations with $(1\,1\,2)$ were also present. Until now, only the MBE technique has achieved purely c-oriented $CeCoIn_5$ thin films. Based on the residual resistance ratio $RRR = \rho(300\mathrm{K})/\rho_0$, the highest quality of c-oriented $CeCoIn_5$ were grown on the MgF_2 substrate in our laboratory.

Table 3.2: $CeCoIn_5$ thin films fabricated using various techniques

Technique	Target material(s)	Substrate	T_{sub} (°C)	P (Pa)	RRR
MBE [88]	Ce, Co, In	Cr/MgO(001)	350	1×10^{-7}	∼5
MBE [89]	Ce, Co, In	a- and r-cut Al_2O_3	500	4×10^{-7}	∼4
MBE [90]	Ce, Co, In	MgF_2(001)	370	1×10^{-7}	∼11
Sputtering [91]	Ce, Co, In	Cr/MgO(001)	550	3 (Ar gas)	∼2
PLD [92]	$CeCoIn_5$ single crystal	Cr/MgO(001)	400	8×10^{-7}	NA
PLD [93]	$CeCoIn_5$ polycrystal	c-cut Al_2O_3	600	4×10^{-5}	∼3

3.1.4 Substrate and fabrication methods

Lattice matching between the thin film and substrate is an important factor for epitaxial growth. We used (001)-oriented magnesium fluoride (MgF_2) as a substrate. It has a rutile-type tetragonal structure with a similar lattice parameter for the a-axis to those of $CeIn_3$ and $CeCoIn_5$. Table 3.3 lists the lattice constants of the substrate and compounds used in this study. In addition, because MgF_2 does not contain oxygen, the oxidation of Ce compounds during growth could be avoided and is thus another critical factor for the growth of Ce-based compounds.

Table 3.3: Lattice constants

	a (Å)	c (Å)
$CeCoIn_5$	4.613	7.551
$CeRhIn_5$	4.653	7.538
$CeIn_3$	4.690	4.690
$YbCoIn_5$	4.533	7.413
$YbRhIn_5$	4.595	7.442
MgF_2	4.625	3.052

The substrate, which is a 10×5 mm one-sided mechanically polished MgF_2, was purchased from Crystal Base, Ltd. Because the flatness of the surface was insufficient for our purpose, we annealed the substrate under UHV at 750°C for 2 h to improve the flatness. After baking the substrate, a clear streak pattern appears in the RHEED image, indicating that the substrate is atomically flat and has a clean surface. Because MgF_2 is a halide material, it is hollowed when exposed to a strong electron beam. We carefully reduced the RHEED irradiation time not to damage the surface of the substrate. To relax the lattice mismatch and improve the quality of the superlattice, some buffer layers were occasionally used. Initially, 30 nm of $CeIn_3$ buffer layers were grown at 450°C. Subsequently, 15 nm of $YbCoIn_5$ buffer layers were grown at 550°C. On top of these, superlattice layers were grown. At some point following the thin film growth, $\sim$ 5 nm of the cobalt capping layer was deposited at room temperature to avoid the oxidization of samples.

3.1.5 LabVIEW program

The fabrication of thin films and superlattices is controlled with LabVIEW programs. Figure 3.3(a) shows the homemade program for the MBE control. The temperature of the substrate and four Knudsen cells are monitored and controlled from this panel. Also, rate monitor, Knudsen cell temperature control sequence setting, and shutter control can be called as sub-programs. Figure 3.3(b), (c) are the LabVIEW block diagrams, indicating the GPIB communication part with the Knudsen cells and the display part on the graph, respectively. The rate monitor of each Knudsen cell is adjusted using the rate monitor shown in Fig. 3.4. The light blue square indicates the raw rate recorded every 1 second, and a red line indicates the moving average value for 60 seconds. After

confirming that the average rate becomes constant for about 30 minutes, we judge to complete the rate adjustment.

Figure 3.5 shows a LabVIEW program that constitutes a shutter sequence for the growth of a superlattice. By synchronizing the opening and closing of the electromagnetic shutter provided in each Knudsen cell with a program, a superlattice structure with a precisely controlled number of layers is possible. As a demonstration, the shutter sequence for $CeCoIn_5(5)/CeRhIn_5(5)$ superlattice is displayed. During the deposition, the temperature of the substrate and each Knudsen cell and the pressure are recorded, and it is confirmed that the growth conditions did not change during the fabrication.

3.2 Characterization

The structural properties of heavy-fermion thin films and superlattices were investigated by RHEED, AFM, XRD, EDX, TEM, and EELS. The transport properties were examined through resistivity measurements. The in-plane resistivity ρ was measured by a standard ac four-probe method using an LR-700 ac resistance bridge. Measurements were performed by applying 10 μA excitation currents along the a-axis, with a magnetic field parallel to the c-axis at temperatures as low as 300 mK in a ^{3}He cryostat. Electrical contacts were produced using DuPont 4929N silver paint.

3.2.1 Reflection high-energy electron diffraction (RHEED)

RHEED is a simple but powerful tool to study the crystal surface and its growth. An electron gun and fluorescent screen face each other centered on the substrate. Electron beams enter the substrate from the electron gun at a very shallow angle, and the diffracted electrons are received by the fluorescent screen. Because the intensity of RHEED reflects the surface roughness, RHEED oscillations reflecting layer-by-layer epitaxial growth can be observed [94], which are shown in figure 3.6. RHEED is thus an indispensable surface-sensitive technique for in situ monitoring of crystal growth.

3.2.2 Atomic force microscopy (AFM)

Atomic force microscopy (AFM) is a scanning probe microscope that uses the atomic force between the sample and tip. It is a technique that can map the surface state of a wide range of objects such as metals, insulators, and polymers to real space with sub-nano height resolution. In this study, AFM was used to confirm the different degrees of surface flatness and domain sizes of the epitaxial films. For this purpose, we used VN-800 KEYENCE, which employs a resistance type cantilever for the tip as well as a tapping mode. Figure 3.7 is a typical AFM image for a heavy-fermion superlattice. The typical surface roughness is within 0.8 nm, which is comparable to the thickness of one unit-cell along the c-axis of $CeCoIn_5$.

(a)

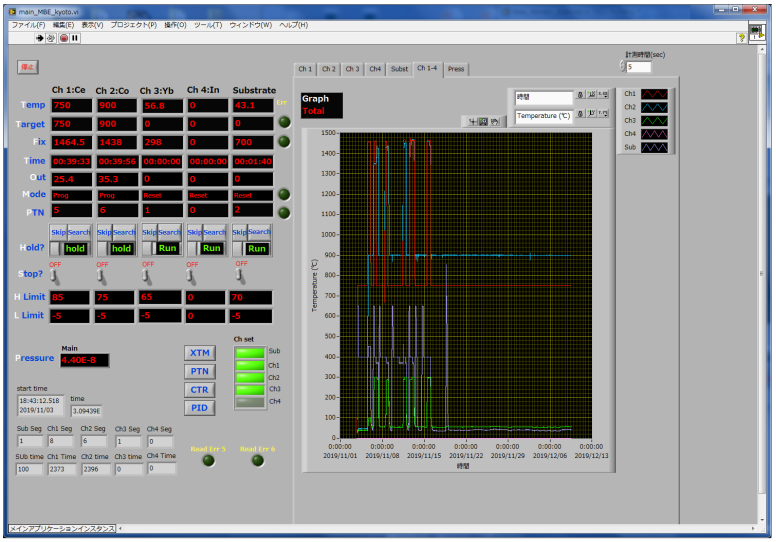

(b)

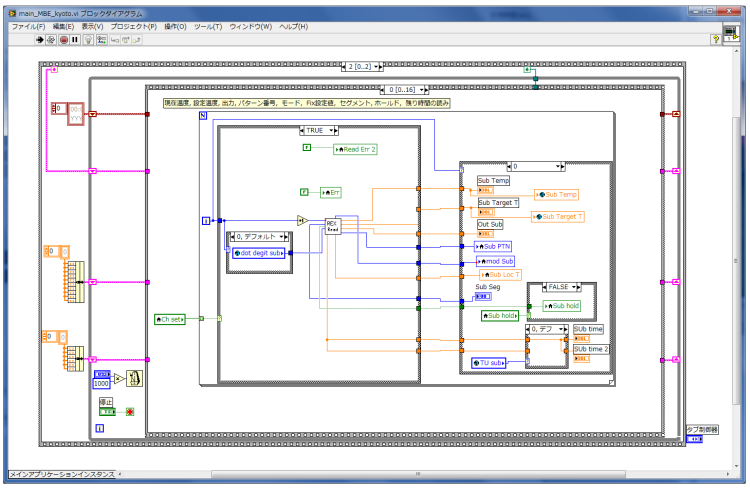

(c)

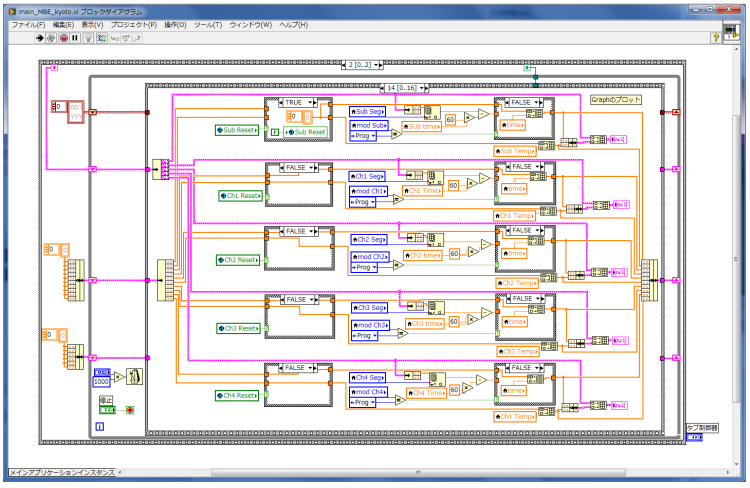

Figure 3.3: LabVIEW program used to control the MBE system. (a) The left side of the screen is used for controlling the temperature of each Knudsen cell. The right side display and records each Knudsen cell temperature and degree of vacuum. (b), (c) Excerpt from the LabVIEW block diagram. Each shows the GPIB communication part with the Knudsen cells and the display part on the graph, respectively.

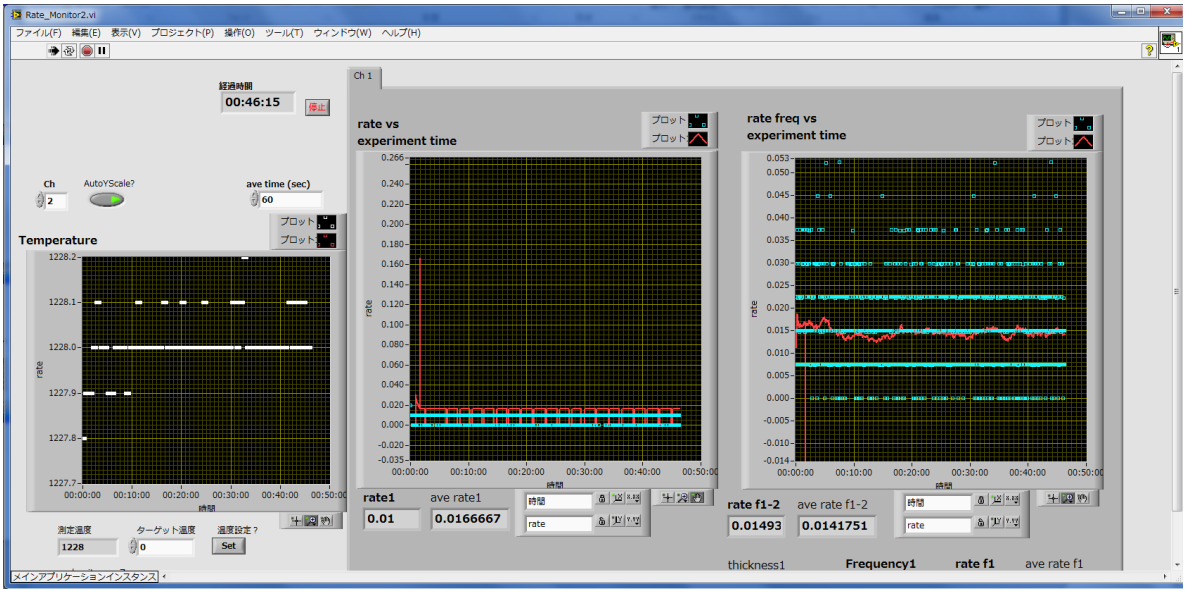

Figure 3.4: The program used for monitoring the deposition rate. The screen shows the rate adjustment for the Co element toward the target of 0.00150 Å. The light blue square indicates the raw rate recorded every 1 second, and a red line indicates the moving average value for 60 seconds.

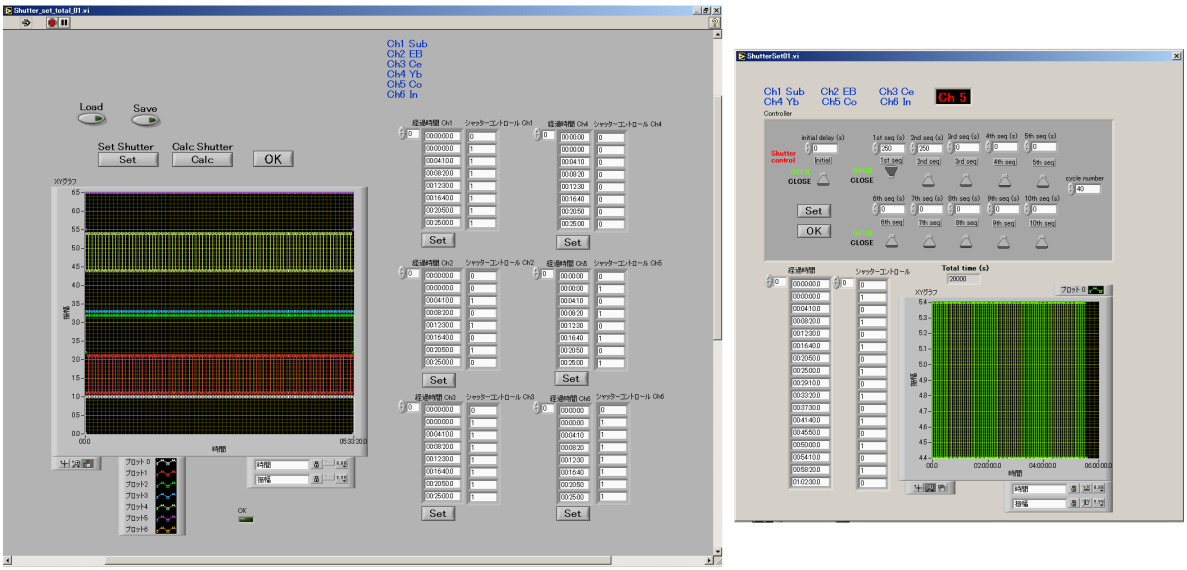

Figure 3.5: The setting screen of shutter sequences for fabrication. As a demonstration, the display shows the setting when the growth of $CeCoIn_5$ block layers is set to 50 seconds, and the growth of $CeRhIn_5$ block layers is set to 50 seconds, repeatedly for 20 times.

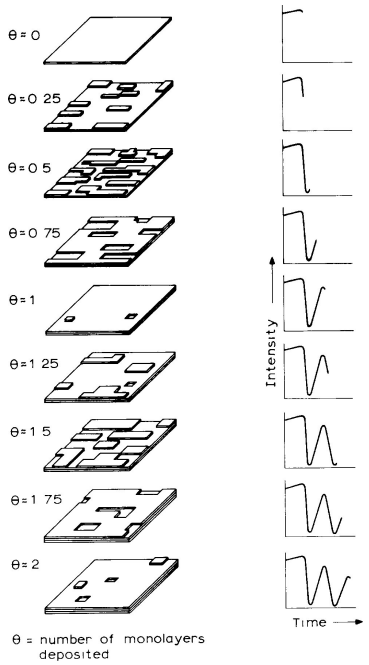

Figure 3.6: Schematic of RHEED oscillations. The left and right panels show the surface of a film and corresponding RHEED intensity as a function of time, respectively [94].

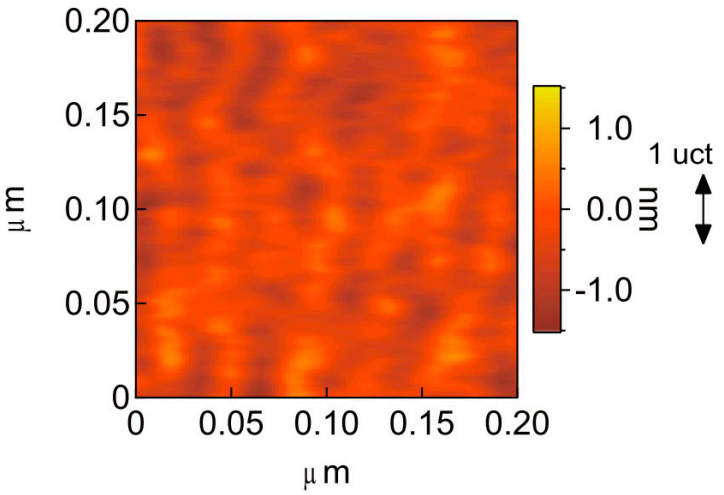

Figure 3.7: Typical AFM image for $YbCoIn_5(3)/CeCoIn_5(8)/YbRhIn_5(3)$ superlattice grown by MBE. The typical surface roughness is within 0.8 nm, which is comparable to the thickness of one unit-cell along the c-axis of $CeCoIn_5$.

3.2.3 Energy-dispersive X-ray spectroscopy (EDX)

Energy-dispersive X-ray spectroscopy (EDX) measures the energy of excited characteristic or fluorescent x-rays by irradiating a sample with an electron beam or x-ray. We can obtain the composed elements on the surface of sample from the EDX spectrum. The depth of analysis depends on the element, and the diffusion region of electrons is approximately several μm. Because a typical film thickness of a thin film used in this study is 300 nm, measured EDX spectrum reflects all information in the film thickness direction such as the buffer layer and substrate. Figure 3.8 shows a typical EDX spectrum and the elements used in mapping $CeIn_3$ thin films. The ratio between Ce and In is 1:3, which is the proper ratio.

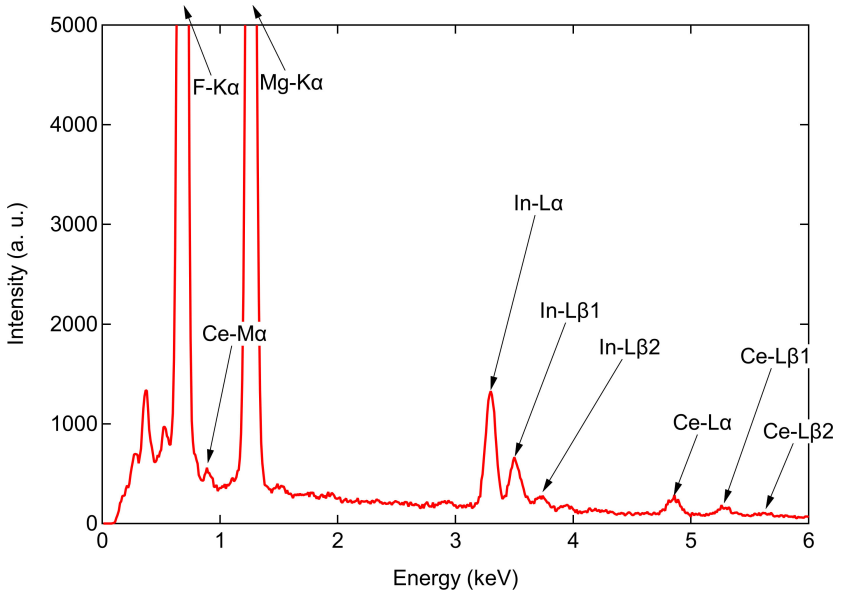

Figure 3.8: EDX spectrum of $CeIn_3$.

3.2.4 Transmission electron microscopy (TEM) and electron energy loss spectroscopy (EELS)

Transmission electron microscopy (TEM) and electron energy loss spectroscopy (EELS) employs spectroscopic measurements with an atomic resolution to determine the structure, composition, and element bonding state according to the energy lost from the incident electron beam. The sub-nanometer spatial resolution of TEM and EELS, which is higher than that of EDX enables us to obtain a cross-sectional image and an element map of the superlattice. To transmit the incident electron beam, thinning the sample is necessary. We sliced up the sample under vacuum and cleaned the surface with ion milling immediately prior to TEM and EELS measurements. Focused ion beam equipment FB2100 or nanoDUET NB5000 were used for sample processing. The acceleration voltage was set to 40 kV and 2 kV for usual processing and surface finishing, respectively. The sample was cooled to approximately -100°C during the finishing

process. The atomic resolution analytical electron microscope JEM-ARM200F was used for observation. All processes and observations were performed by the Kobelco Research Institute.

3.3 Pressure experiment

In-plane resistivity measurements under pressure was performed with a hybrid piston-cylinder-type high pressure cell (Figure 3.9). The pressure cell was purchased from CT Factory, Ltd., Japan. The maximum working pressure for repeated use of this type of pressure cell is as high as approximately 2.6 GPa. The outer cylinder as well as the upper and lower lock nuts are composed of CuBe, and the inner shell is composed of NiCrAl nested inside the outer cylinder. The piston and piston backup are composed of tungsten carbide (WC). Electrical leads were introduced into the sample space through the hole ($0.6\,\phi$) of a plug, and the hole was sealed by Stycast 2850FT epoxy. The diameter and height of the sample holder consisting of a plug and Teflon cap were 4 mm and $\sim$ 20 mm, respectively. One or two samples could be mounted in the sample space perpendicular or parallel to the axial direction of the cell. The sample space was sealed with a Teflon cap and CuBe gasket. We used Daphne7373 oil as the pressure medium. We applied a load with a 20 tons hydraulic pressure machine at room temperature.

The pressure inside the pressure cell was determined by the superconducting transition of lead (Pb), which was obtained by the quasi-four terminal resistivity measurement. The pressure dependence of the superconducting transition temperature T_c of Pb can be well expressed as $T_c(p) = T_c(0) - (0.365 \pm 0.003)p$ for a wide pressure range [95]. Here, the unit of pressure p is GPa. A long and narrow shaped Pb installed inside the sample space is sensitive to the pressure gradient for the axial direction of the cell, which can be known by examining the width of the superconducting transition. In this study, the transition width was within 20 mK, indicating a good hydrostatic condition.

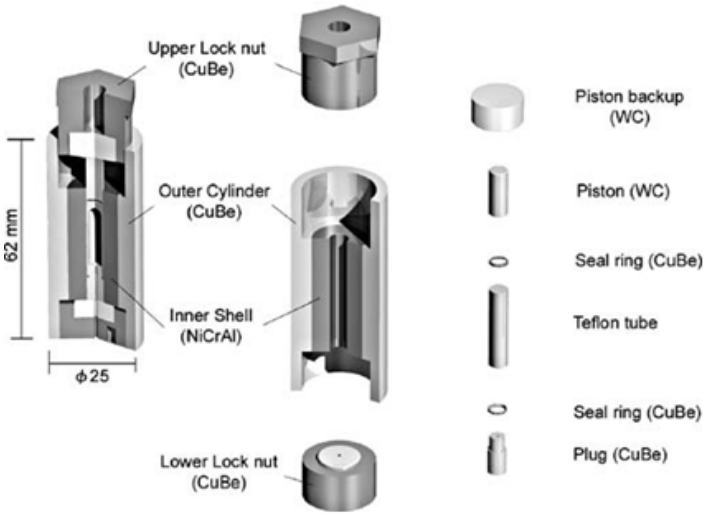

Figure 3.9: Cross-sectional view of the piston-cylinder high-pressure cell designed by Y. Uwatoko [96].

Chapter 4

Emergent exotic superconductivity in $YbCoIn_5/CeCoIn_5/YbRhIn_5$ tricolor superlattices

4.1 Introduction

Spin-orbit coupling (SOC) is a relativistic effect that entangles the spin and orbital degrees of freedom of the electrons. Recently, it has been shown that the SOC and asymmetry of the crystal potential can dramatically affect the electronic properties, leading to several novel phenomena in the various field of condensed matter physics, such as spintronics [97, 98], topological matter [99], and exotic superconductivity [85]. In superconductors, the inversion symmetry important constraint on the pairing states. In the presence of inversion symmetry, Cooper pairs are classified into spin-singlet and triplet states. On the other hand, in the absence of inversion symmetry, an asymmetric potential gradient yields an SOC that gives rise to a parity-violated superconductivity. Such a superconducting state exhibits unique properties including the admixture of spin-singlet and triplet states [102, 103], unusual paramagnetic [103] and electromagnetic response [100, 101], and topological superconducting states [18, 99, 104], which cannot be realized in conventional superconductors with global inversion symmetry. For instance, asymmetric potentials gradient in the direction perpendicular to the two-dimensional (2D) plane induce the Rashba asymmetric spin-orbit coupling (ASOC), $\alpha_{\mathrm{R}}\boldsymbol{g}(\boldsymbol{k})\cdot\boldsymbol{\sigma} \propto (\boldsymbol{k}\times\nabla V)\cdot\boldsymbol{\sigma}$, where $\boldsymbol{g}(\boldsymbol{k}) = (k_y, -k_x, 0)/k_{\mathrm{F}}$, k_{F} is the Fermi wave number, and $\boldsymbol{\sigma}$ is the Pauli matrix. The Rashba ASOC lifts the electron-spin degeneracy and splits the Fermi surface into two sheets with different spin structures [83–85]. The energy splitting is given by α_{R}, and the spin direction is aligned within the plane, rotating clockwise on one sheet and anticlockwise on the other. When the Rashba splitting exceeds the superconducting gap energy ($\alpha_{\mathrm{R}} > \Delta$), the superconducting state is dramatically modified.

It has been pointed out theoretically that the effect of the Rashba ASOC on superconductivity can be more pronounced by strong electron correlations [105, 106]. Al-

though strongly correlated heavy fermion superconductors with broken inversion symmetry, such as $CePt_3Si$ [107], $CeRhSi_3$ [108], and UIr [109], have been reported, the superconductivity is essentially three dimensions and often coexists with magnetic order. Moreover, the magnitude of the ASOC is hard to control, as it is determined by the crystal structure. In heavy transition metal oxides with $4d$ or $5d$ elements, it has been suggested that the cooperative effect of the strong electron correlation and strong spin-orbit interaction gives rise to exotic electronic states such as Weyl semimetal and topological Mott insulator [146], but superconductivity in such materials has not been reported so far. Thus in the superconductors with strong Rashba ASOC, the role of strong electron-electron interaction has remained largely unexplored due to the lack of suitable material systems. Here, using a state-of-the-art molecular beam epitaxy (MBE) technique, we introduce new 2D systems with significant electron correlations and tunable Rashba ASOC, which make such investigations possible.

In the following section, we first describe the basic theory of the superconductivity without inversion symmetry. Second, we introduce the concept of the 'local' ISB at the interfaces and explain the effect of local ISB on the superconductivity. Then, we emphasize the purpose of this study by comparing 'bicolor' and 'tricolor' heavy-fermion superlattices. Next, we show the experimental details, and subsequently, we report and discuss the characterization of the tricolor superlattices. Then, we report and discuss the transport properties of them by comparing the bicolor superlattices. We also discuss a possible exotic superconducting state in a parallel field. Finally, we end with a summary and our conclusions.

4.1.1 Basic theory of non-centrosymmetric superconductivity

In the non-centrosymmetric structure, the asymmetric potential gradient yields asymmetric spin-orbit coupling (ASOC). In general, ASOC is described by the following Hamiltonian using the second quantization representation [103]:

$$H_{\mathrm{ASOC}} = \alpha \sum_{\boldsymbol{k},s,s'} \boldsymbol{g}(\boldsymbol{k}) \cdot \boldsymbol{\sigma}_{ss'} c^{\dagger}_{\boldsymbol{k}s} c_{\boldsymbol{k}s'}. \tag{4.1}$$

Here, $c^{\dagger}_{\boldsymbol{k}s}$ ($c_{\boldsymbol{k}s}$) creats (annihilates) an electron with momentum $\boldsymbol{k}$ and spin s. α is a coupling constant, $\boldsymbol{\sigma}_{ss'}$ are the Pauli matrices., and $\boldsymbol{g}$ is called the g vector that characterizes ASOC. This g vector is determined by the symmetry of the crstal. If the crystal structure belongs to the tetragonal point group (C_{4v}) in which the mirror symmetry along the c-axis is broken, the g vector is given by $\boldsymbol{g}(\boldsymbol{k}) = (-k_y, k_x, 0)$, which is known as Rashba type [83]. If the crystal structure belongs to the cubic point group (T_d), it is given by $\boldsymbol{g}(\boldsymbol{k}) = (k_x(k_y^2 - k_z^2), k_y(k_z^2 - k_x^2), k_z(k_x^2 - k_y^2))$, which is known as Dresselhaus type [110]. The g vector has odd parity regardless of the crystal structure as a consequence of time reversal symmetry and satisfies $\boldsymbol{g}(-\boldsymbol{k}) = \boldsymbol{g}(\boldsymbol{k})$.

To investigate the effect of ASOC on the electronic properties, we introduce the model Hamiltonian for non-centrosymmetric system:

$$H = \sum_{\boldsymbol{k},s} \epsilon(\boldsymbol{k}) c^{\dagger}_{\boldsymbol{k}s} c_{\boldsymbol{k}s} + \alpha_{\mathrm{R}} \sum_{\boldsymbol{k},s,s'} \boldsymbol{g}(\boldsymbol{k}) \cdot \boldsymbol{\sigma}_{ss'} c^{\dagger}_{\boldsymbol{k}s} c_{\boldsymbol{k}s'}. \tag{4.2}$$

Assuming the Rashba ASOC $\alpha_{\mathrm{R}}\boldsymbol{g}(\boldsymbol{k})$ and using $(c^{\dagger}_{\boldsymbol{k},\uparrow}, c^{\dagger}_{\boldsymbol{k}\downarrow})$ as the basis, we see that this Hamiltonian becomes [85, 122],

$$H = \begin{pmatrix} \epsilon(\boldsymbol{k}) & -i\alpha_{\mathrm{R}}\boldsymbol{k}_{-} \\ i\alpha_{\mathrm{R}}\boldsymbol{k}_{+} & \epsilon(\boldsymbol{k}) \end{pmatrix}, \tag{4.3}$$

where $\boldsymbol{k}_{\pm} = \sin \boldsymbol{k}_x \pm i \sin \boldsymbol{k}_y$. We are able to diagonalized this matrix. Therefore, the eigenvalue is given by:

$$E_{\pm}(\boldsymbol{k}) = \epsilon(\boldsymbol{k}) \pm \alpha_{\mathrm{R}}\boldsymbol{g}(\boldsymbol{k}). \tag{4.4}$$

The Rashba ASOC splits the Fermi surface into two sheets with different spin texture as shown in Figure. 4.1: the spin direction is tilted into the plane, rotating clockwise on one Fermi surface and anticlockwise on the other. The Fermi surface splitting is order of α_{R}. In this band, the degree of degeneracy due to inversion symmetry is degenerate, while that due to time reversal symmetry is preserved. The Fermi surface splitting by Rashba ASOC is qualitatively different from Zeeman splitting due to magnetic field.

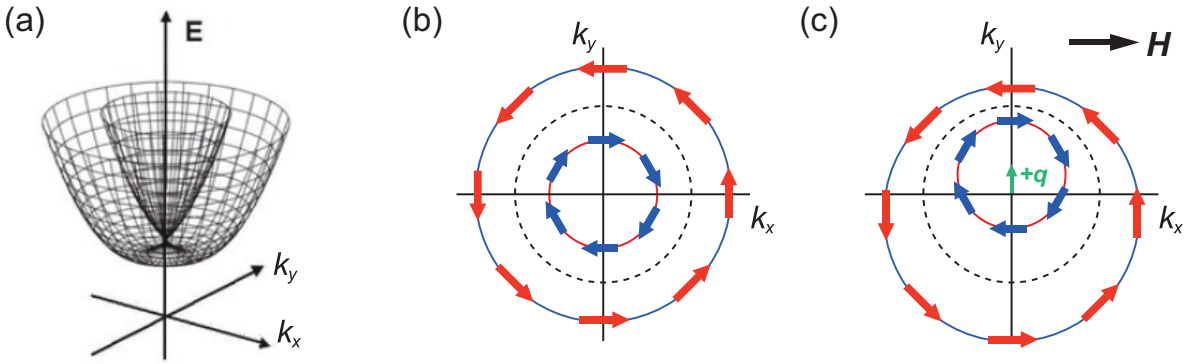

Figure 4.1: (a), (b) 2D Fermi surfaces in the presence of Rashba ASOC and corresponding spin texture for a zero magnetic field. (c) In the presence of an in-plane magnetic field, leading to an off-center shift of the both Fermi surfaces.

The most characteristic effect on the superconducting state due to the lack of space inversion symmetry is a mixture of superconducting states with different parities. When there is spatial inversion symmetry, the superconducting order parameter Δ is an eigenfunction of the parity operator P. Therefore, the pairing state can be classified into the spin siglet state satisfying $\Delta(\boldsymbol{k}) = \Delta(-\boldsymbol{k})$ and the spin triplet state satisfying $\Delta(\boldsymbol{k}) = -\Delta(-\boldsymbol{k})$. However, if the spatial inversion symmetry is broken, the parity operator does not become a good quantum number, so that both even-parity spin-singlet and odd-parity spin-triplet pairing can be mixed.

To see the effect of the magnetic field H on the Fermi surface spin-split by ASOC, we add a Zeeman term ($H_z = \sum \mu_{\mathrm{B}} \boldsymbol{H} \cdot \sigma_{ss'} c^{\dagger}_{\boldsymbol{k}s} c_{\boldsymbol{k}s'}$) to the previous Hamiltonian. Then, the eigenvalue is given by:

$$E_{\pm}(\boldsymbol{k}, \boldsymbol{H}) = \epsilon(\boldsymbol{k}) \pm \sqrt{\alpha_{\mathrm{R}}^2 |\boldsymbol{g}(\boldsymbol{k})|^2 - 2\alpha_{\mathrm{R}}\mu_{\mathrm{B}}\boldsymbol{g}(\boldsymbol{k}) \cdot \boldsymbol{H} + \mu_{\mathrm{B}}^2 |\boldsymbol{H}|^2}. \tag{4.5}$$

Considering the large ASOC limit ($\alpha_{\mathrm{R}} \gg \mu_{\mathrm{B}}|\boldsymbol{H}|$), the energy dissipation due to magnetic field can be expressed as

$$E_{\pm}(\boldsymbol{k}, \boldsymbol{H}) \approx \epsilon(\boldsymbol{k}) \pm \alpha_{\mathrm{R}}|\boldsymbol{g}(\boldsymbol{k})| \mp \alpha_{\mathrm{R}}\mu_{\mathrm{B}}\boldsymbol{g}(\boldsymbol{k}) \cdot \boldsymbol{H}. \tag{4.6}$$

The Zeeman interaction given by $\alpha_{\mathrm{R}}\mu_{\mathrm{B}}\boldsymbol{g}(\boldsymbol{k}) \cdot \boldsymbol{H}$ leads to anisotropic suppression of the Pauli pair-breaking effect. Let us think about the case of the Rashba type $\boldsymbol{g}(\boldsymbol{k}) = (-k_y, k_x, 0)$. When magnetic field is applied to c-axis direction, $\boldsymbol{g}(\boldsymbol{k}) \cdot \boldsymbol{H} = 0$, so a suppression of Pauli pair breaking effect occurs. On the other hand, when magnetic field is applied in-plane, $\boldsymbol{g}(\boldsymbol{k}) \perp \boldsymbol{H}$ is not always satisfied, so suppression of Pauli pair breaking effect is weaker than out-of-plane field. Therefore, Rashba ASOC causes angular dependent suppression of the Pauli pair breaking effect.

In the non-centrosymmetic superconductor, a spatially modulated superconducting state can be stabilized. This superconducting state has a finite momentum of Cooper pairs in similar manner with FFLO state in centrosymmetric superconductor. The superconducting order parameter Δ of well-known FF state and LO state are following,

$$FFstate : \Delta(\boldsymbol{r}) = \Delta e^{i\boldsymbol{q}\cdot\boldsymbol{r}}, \tag{4.7}$$

$$LOstate : \Delta(\boldsymbol{r}) = \Delta \cos(i\boldsymbol{q} \cdot \boldsymbol{r}). \tag{4.8}$$

In non-centrosymmetric superconductor, the change in Fermi surface caused by ASOC stabilizes so-called helical or stripe phases.

These superconducting state called the helical or the stripe phase, are similar to FFLO state in that pairing with spatial modulation and a high upper critical field that exceed the upper critical field determined by Pauli pair breaking effect. In this section, we will see the relationship between spatial inversion symmetry breaking and these specific phases, the stability of these phases, magnetic phase diagrams, and characteristic physical properties.

Let us think about superconducting state with spatial inversion. The band split of spin degeneracy occurs due to Zeeman effect under sufficient magnetic field and the pairing between up spin and down spin within the same band is not able to form. As a consequence, the spin-singlet superconducting state was destroyed. This is called Pauli pair breaking effect. On the other hand, in the case of a non-centrosymmetric system, since the spins have already degenerated, different phenomena occur. Let us think about the non-centrosymmetric system in which the mirror symmetry along z-direction is broken and apply magnetic field along z direction (we will refer this direction as perpendicular direction). In this case, the shape of Fermi surface does not change with magnetic field. Thus, the pairing between k and -k is always preserved. As a consequence, the suppression of the Pauli effect occurs when you apply magnetic field perpendicular direction to a Rashba type non-centrosymmetric superconductor. In this case, the upper critical field is determined by the orbital limiting field. Actually, in the non-centrosymmetric heavy-fermion superconductor $CeRhSi_3$ and $CeIrSi_3$, an upper critical field of 20–30 T, which is huge considering T_c, was observed. In case in-plane magnetic field applied to x direction, the Fermi surface changes as shown in Figure 4.1, in which each center of mass moves opposite y-direction by $q/2$. The helical phase with

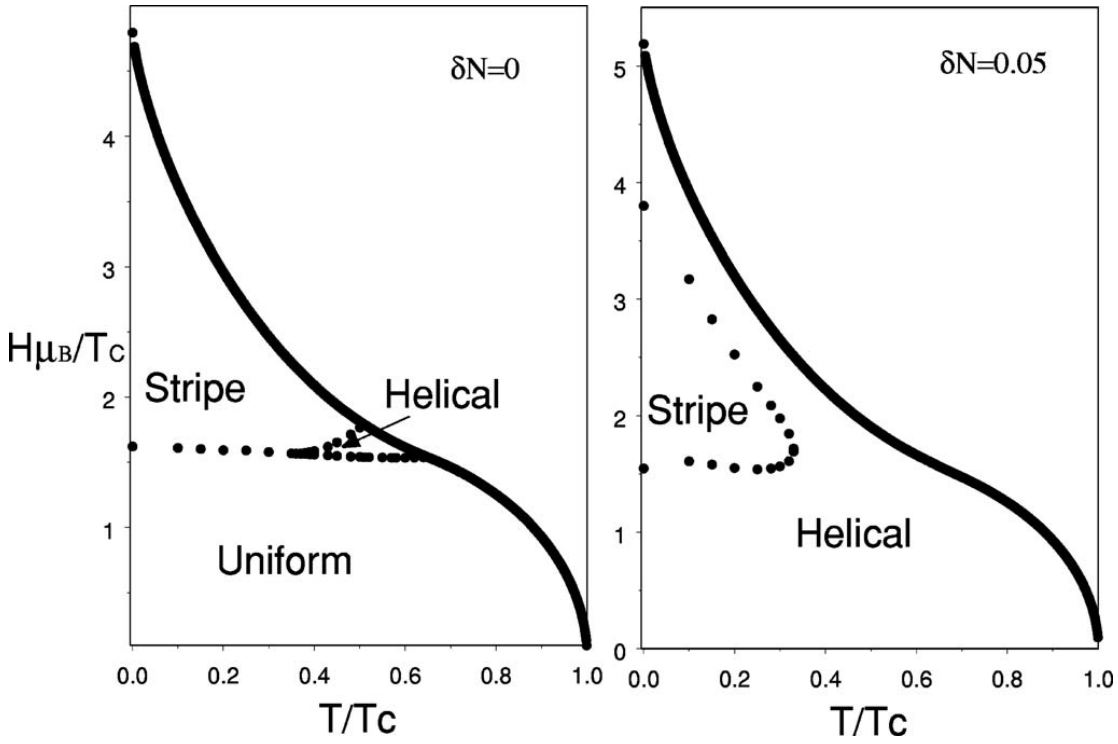

Figure 4.2: Temperature-field phase diagram in non-centrosymmetric Rashba superconductor under in-plane magnetic field [111]. The left graph shows the case of $\delta N = 0$, the right graph shows the case of $\delta N = 0.05$. 'Uniform' indicates the spatially homogenous state. When the small difference δN between the bands $N^+(k)$ and $N^-(k)$ exists, the helical phase dominates the phase diagram.

superconducting gap function $\Delta(R) = \Delta_0 e^{iq\cdot R}$ is stabilized. Since the movements of the center of mass of the Fermi surfaces are the opposite direction, the condensation energy of one of the Fermi surfaces increases, and that of the other decreases. As a result, it causes competition between the helical phase and the stripe phase in which the superconducting gap function is $\Delta(R) = \Delta_0 \cos(q \cdot R)$. The gap amplitude is spatially homogeneous in the helical phase and that is modulated in the stripe phase. So these two phases show different properties. Agterberg and Kaur studied the stability of these phases under in-plane magnetic field. Figure 4.2 depicts the calculated temperature-field phase diagram. We can see that the occupation region of the helical phase become larger in the phase diagram when the difference δN of the density of state for bands $N^+(k)$ and $N^-(k)$. The stripe phase also appears in the phase diagram which is destabilized with increasing δN.

4.1.2 Local inversion symmetry breaking

As we see, the ASOC induced by inversion symmetry breaking (ISB) affects superconducting properties through the change in the Fermi surface. In this section, we will introduce the 'local' ISB.

For example, let us think about the tri-layer system, as shown in Figure. 4.3(b). The inner layer is at the center of inversion, the inversion symmetry of the system is preserved. However, in the top (bottom) layer, inversion symmetry is broken because there are no layers above (below), resulting in the appearance of non-zero ASOC ($\alpha_{\mathrm{R}} \neq 0$). The α_{R} has the same amplitude and the opposite sign in the upper and the lower layers.

Local ISB has a significant effect on physical properties when the ratio of the interface in the whole structure is high, as can be seen by comparing Figures 4.3(a) and 4.3(b). Also, the band structure must have an energy scale that competes with ASOC. In this regard, it is known that local ISB has a significant influence on physical properties in the region where the size of ASOC is larger than inter-layer hopping $t_\perp$ ($\alpha_{\mathrm{R}}/t_\perp > 1$). For real materials, the interlayer coupling can be the same order of Fermi energy ($t_\perp \sim E_{\mathrm{F}}$), whereas ASOC is often $\alpha_{\mathrm{R}} \gg E_{\mathrm{F}}$.

4.1.3 Introduction of global inversion symmetry breaking

Recent technological advances in fabricating heavy-fermion superlattices, where a Ce-based heavy-fermion compound and a nonmagnetic conventional metal are stacked alternatively, open up new playgrounds for investigating 2D strongly correlated superconductors [75, 79]. The spin-orbit interaction in Ce-based compounds is generally significant because of heavy elements. It has been demonstrated that in $CeCoIn_5$/$YbCoIn_5$ superlattices illustrated in Figure 4.4(a), where a heavy-fermion superconductor $CeCoIn_5$ and nonmagnetic metal $YbCoIn_5$ are stacked alternately as '$ABAB\cdots$' the superconducting heavy quasiparticles as well as magnetic fluctuations can be confined within Ce block layers (BLs) with atomic thickness [76, 81, 82]. These 'bicolor' superlattices maintain centrosymmetry, although it has been suggested that the local inversion symmetry

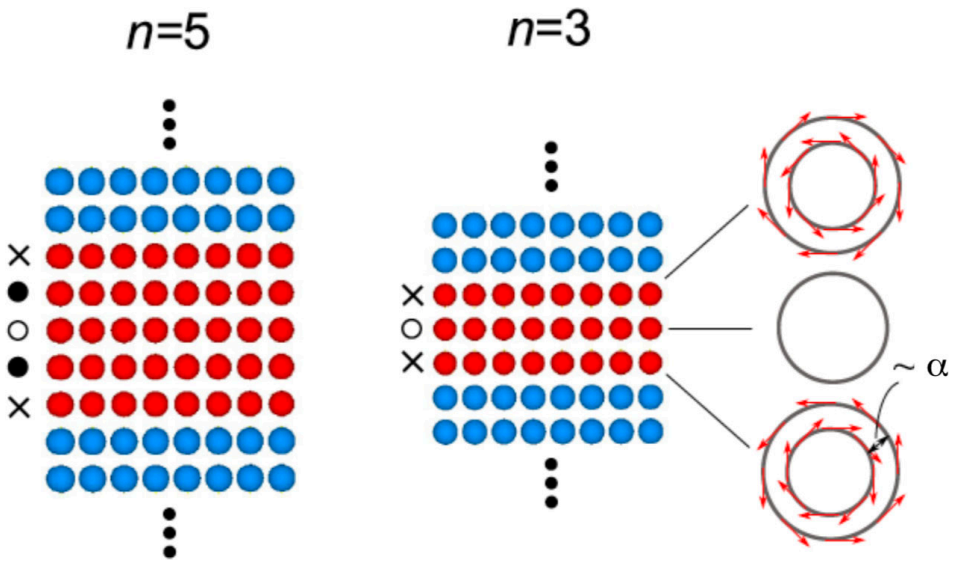

Figure 4.3: Schematic representation of atomic layered structure for $n = 5$ and 3, respectively. Blue dots indicate non-superconducting layers and red dots indicate superconducting layers. Inversion symmetry is broken in the layers ($\times$ or $\bullet$), is preserved in the central layer ($\circ$). At the right most side, Fermi surface of each layer is represented. In the top or bottom layers, Fermi surface is splitted due to Rashba ASOC. After ref. [81].

breaking at the interface between two compounds influences the superconducting and magnetic properties [77,80–82]. It has been shown that the effect of inversion symmetry breaking appears to be pronounced in $ABAB'$-type superlattices, where i-unit-cell-thick (UCT) $CeCoIn_5$ is sandwiched by j- and j'-UCT $YbCoIn_5$ ($j \neq j'$) [Figure 4.4(b)] [112]. In these superlattices, inversion symmetry is not preserved in $CeCoIn_5$ BLs owing to the thickness modulation of the $YbCoIn_5$ BLs, in addition to the local ISB. However, as shown in Figure 4.4(b), mirror planes are present in the $YbCoIn_5$ BLs and hence the global inversion symmetry is preserved in the whole crystals. Therefore, it is still a challenging issue to realize exotic superconducting phenomena associated with the global ISB in the heavy-fermion superlattices.

Here, to introduce a global ISB in these heavy-fermion superlattices, we fabricated 'tricolor' heavy-fermion superlattice with an asymmetric sequence $YbCoIn_5/CeCoIn_5/YbRhIn_5$, in which $CeCoIn_5$ is sandwiched by two different non-magnetic metals, $YbCoIn_5$ and $YbRhIn_5$, as illustrated in Figure 4.4(b). These tricolor superlattices with an asymmetric '$ABCABC\cdots$' arrangement introduces broken inversion symmetry along the stacking direction. Although the crystal structure of bulk $CeCoIn_5$ possesses the inversion symmetry, band structure calculations suggest that even a small degree of ISB can induce a large Rashba splitting of the Fermi surface [112].

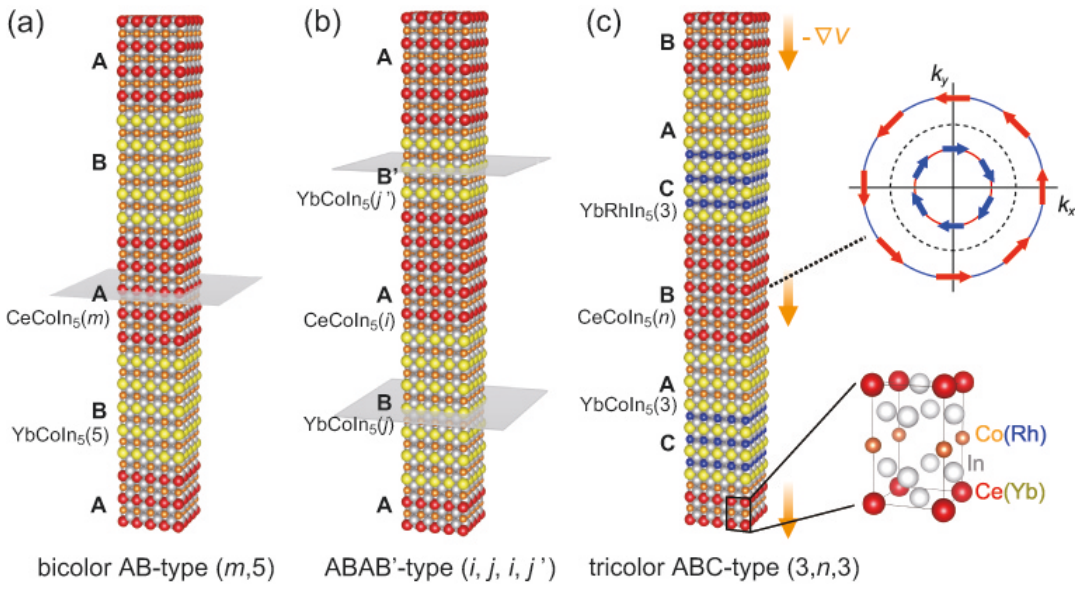

Figure 4.4: Schematic representations of heavy-fermion superlattices. (a) Centrosymmetric bicolor superlattices $CeCoIn_5(m)/YbCoIn_5(5)$. The center of a $CeCoIn_5$ BL (ash plane) is a mirror plane. (b) $ABAB'$-type superlattices $CeCoIn_5(i)/YbCoIn_5(j)/CeCoIn_5(i)/YbCoIn_5(j')$ ($j \neq j'$). The center of a $CeCoIn_5$ BL is not a mirror plane, but the centers of $YbCoIn_5$ BLs (ash planes) are mirror planes. (c) Non-centrosymmetric tricolor superlattices $YbCoIn_5(3)/CeCoIn_5(n)/YbRhIn_5(3)$. Crystal structure of $TMIn_5$ (T: Ce or Yb, M: Co or Rh) with tetragonal symmetry is also shown. In the tricolor superlattices, all layers are not the mirror planes. The orange arrows represent the asymmetric potential gradient $-\nabla V$ due to the broken inversion symmetry. The Rashba ASOC splits the Fermi surface into two sheets; spin direction rotates clockwise on one sheet (blue arrows) and anticlockwise on the other (red arrows).

4.2 Experimental details

The tricolor superlattices $YbCoIn_5/CeCoIn_5/YbRhIn_5$ with c-axis oriented structure were epitaxially grown on MgF_2 substrate using the molecular beam epitaxy (MBE) technique. We first grew $CeIn_3$ ($\sim$ 20 nm) as a buffer layer on MgF_2. Then 3-UCT $YbCoIn_5$, n-UCT $CeCoIn_5$ (n = 5 and 8), and 3-UCT $YbRhIn_5$ were grown alternatively. The sequence of $YbCoIn_5(3)/CeCoIn_5(n)/YbRhIn_5(3)$ was stacked repeatedly 40 times for $n = 5$ and 30 times for $n = 8$ tricolor superlattices, so that the total thickness was about 300 nm. We also fabricated bicolor superlattices consisting of alternating layers of m-UCT $CeCoIn_5$ (m = 5 and 8) and 5-UCT $YbCoIn_5$, $CeCoIn_5(m)/YbCoIn_5(5)$, and those of 5-UCT $CeCoIn_5$ and 5-UCT $YbRhIn_5$, $CeCoIn_5(5)/YbRhIn_5(5)$.

The superlattice structures were confirmed by transmission electron microscopy (TEM), X-ray diffraction (XRD), atomic force microscopy (AFM), and reflection high-energy electron diffraction (RHEED).

Electrical in-plane resistivity measurements were performed by a standard four-probe method. The LR-700 ac resistance bridge and AVS-47B ac resistance bridge were used for the sample and the thermometer, respectively, at temperatures as low as 80 mK in a dilution refrigerator. We used 4 T split maget with a mechanical rotator for the precise angular dependence of the upper critical field H_{c2} and 12 T.

4.3 Results and Discussion

4.3.1 Charaterization

The crystalline quality of tricolor superlattices was evaluated by several techniques. Streak pattern of the RHEED image shown in Figure 4.5(a) was observed during the whole growth of the superlattices, indicating good epitaxy. The AFM image shown in Figure 4.5(b) reveals that the surface roughness is within $\pm$1 nm, which is comparable to one UCT along the c axis of the constituents ($CeCoIn_5$, $YbCoIn_5$, and $YbRhIn_5$). The atomically flat regions extend over distances of $\sim 0.1\,\mu$m, showing that the transport properties are not expected to be seriously influenced by the roughness. The X-ray diffraction patterns are shown in Figure 4.5(c). The position of the lateral satellite peaks and their asymmetric heights can be reproduced by the step-model simulations (red lines) neglecting interface and layer-thickness fluctuations. This indicates the growth with no discernible interdiffusion across the interfaces, confirming that the superlattices were fabricated as designed. Figure 4.5(d) depicts the high-resolution cross-sectional TEM image along the (110) direction for $n = 8$ tricolor superlattice. Clear interface between $CeCoIn_5$ and $YbRhIn_5/YbCoIn_5$ layers is observed. The intensity integrated along the horizontal direction of the image plotted against vertical position shows that the intensities of Ce, Yb, Co, Rh, and In atoms are almost constant within each BLs. A clear difference between the Ce and Yb layers can be seen in the integrated intensity. Although the interface between $YbCoIn_5$ and $YbRhIn_5$ is less visible in the TEM image, there is a discernible difference in the integrated intensity at Co and Rh sites in $YbRhIn_5/YbCoIn_5$ layers. The sharp boundaries at the interfaces between BLs also

demonstrate the absence of the interdiffusion. Because we have 3-UCT $YbCoIn_5$ and 3-UCT $YbRhIn_5$ spacers between $CeCoIn_5$, the RKKY interaction between the adjacent Ce BLs is less than 0.1 % of that between the neighboring Ce atoms in the same layer [113], indicating that $CeCoIn_5$ BLs are magnetically decoupled. Moreover, the superconducting proximity effect between $CeCoIn_5$ layer and neighboring $YbCo(Rh)In_5$ layer is expected to be negligibly small due to the large Fermi velocity mismatch [114]. In fact, it has been shown that in the superlattices with 4–6 UCT $CeCoIn_5$ layers, whose thickness is comparable to the perpendicular coherence length $\xi_c \sim 3$–4 nm, 2D heavy fermion superconductivity is realized [76, 81, 115]. The lattice constants a of $CeCoIn_5$ single crystal, $CeCoIn_5$ thin films, and superlattices are summarized in Table 4.1. The tensile strain along a-axis expected for tricolor superlattices is smaller than that of $CeCoIn_5/YbCoIn_5$.

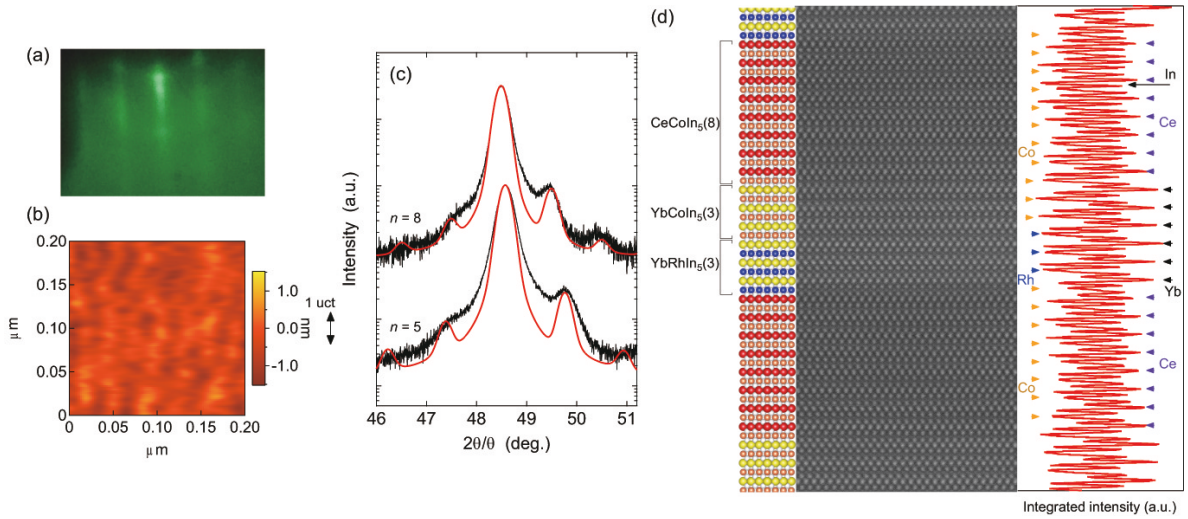

Figure 4.5: (a) Typical RHEED streak patterns for $n = 8$ tricolor superlattice taken during the crystal growth. (b) Typical AFM image for $n = 8$ tricolor superlattice grown by MBE. (c) Cu Kα_1 X-ray diffraction patterns for $n = 5$ and 8 superlattices around the main (0 0 4) peaks. Red lines represent the step-model simulations ignoring the interface and layer-thickness fluctuations. (d) High-resolution cross-sectional TEM image of the $n = 8$ tricolor superlattice with the electron beam aligned along the [1 1 0] direction. The right panel is the intensity integrated over the horizontal width of the image. The positions of Ce, Yb, Co, and Rh atoms can be identified from the dips and peaks as shown by arrows, which are consistent with the designed superlattice structure shown in the left panel.

4.3.2 Rashba spin-orbit interaction in the tricolor superlattices

Figure 4.6 depicts the temperature T dependence of the resistivity $\rho(T)$ for $n = 5$ and 8 tricolor superlattices. The superconducting transition temperature T_c is determined

Table 4.1: Lattice constants a of $CeCoIn_5$ single crystal, thin film, and superlattices. Lattice constant in the superlattice $YbCoIn_5(3)/CeCoIn_5(n)/YbRhIn_5(3)$ are determined by $a = (3a_{YbCoIn5} + na_{CeCoIn5} + 3a_{YbRhIn5})/(6 + n)$ with the same criteria as described in Ref. [76]. The lattice mismatch between a material and the $CeCoIn_5$ single crystal is calculated from the relation $\Delta a = (a - a_{CeCoIn5})/a_{CeCoIn5}$.

	a (Å)	Δa (%)
$CeCoIn_5$ single crystal	4.613	
$CeCoIn_5$ film	4.620	0.2
$n = 8$ tricolor superlattice	4.592	-0.5
$n = 5$ tricolor superlattice	4.586	-0.6
$CeCoIn_5(5)/YbCoIn_5(5)$	4.573	-0.9
$CeCoIn_5(5)/YbRhIn_5(5)$	4.604	-0.2

by the midpoint of the resistive transition. The T_c is 0.4 K and 0.8 K for $n = 5$ and 8, respectively. For comparison, $\rho(T)$ for $m = 5$ and 8 bicolor $CeCoIn_5(m)/YbCoIn_5(5)$ superlattices are also shown in Figure 4.6. The T_c of the tricolor superlattices are suppressed compared with those of the $CeCoIn_5$ thin film ($T_c = 2.0$ K) and the bicolor superlattices with the same $CeCoIn_5$ BL thickness. This reduction of T_c is unlikely due to the difference in the impurity and interface roughness scatterings, since the residual resistivity at $T \to 0$ and residual resistivity ratio at T_c [$\rho(300\,\mathrm{K})/\rho(T_c)$] of the bicolor and tricolor superlattices are comparable. Moreover, T_c of bicolor $CeCoIn_5(5)/YbCoIn_5(5)$ and $CeCoIn_5(5)/YbRhIn_5(5)$ superlattices is higher than T_c of tricolor superlattice with the same $CeCoIn_5$ BL thickness (inset of Figure 4.6). This implies that the strain effect at the interfaces is not important for determining T_c. We point out that the reduction of T_c in the tricolor superlattices can be attributed to the Rashba effect. In fact, the Fermi surface splitting due to the Rashba effect should modify seriously the nesting condition and hence is expected to reduce the commensurate AFM fluctuations with a wave vector $\boldsymbol{Q} = (\pi/a, \pi/a, /\pi/c)$, which is dominant in bulk $CeCoIn_5$ [116]. In addition, the broken inversion symmetry reduces the AFM fluctuations by lifting the degeneracy of the fluctuation modes through the helical anisotropy of the spin configuration [77, 82, 117, 118]. Given that the superconductivity of $CeCoIn_5$ is mediated by AFM fluctuations, the reduction of the AFM fluctuations lead to the suppression of T_c in the tricolor superlattices.

Figures 4.7(a) and 4.7(b) show the resistive transitions in magnetic fields applied parallel to the 2D plane for $n = 8$ and 5 tricolor superlattice, respectively. Figures 4.7(c) and 4.7(d) show the expanded view at low temperatures. As shown in Figures 4.7(c) and 4.7(d), a nearly parallel shift of the resistive transition to lower temperatures with increasing magnetic field is observed in both superlattices. Figures 4.7(e) and 4.7(f) depict in-plane H_{c2} determined by four different criteria [$\rho(T, H) = 0.3\rho_N(T)$, $0.5\rho_N(T)$, $0.7\rho_N(T)$, and $0.9\rho_N(T)$], as a function of temperature for $n = 8$ and 5 tricolor superlattices, respectively. Here we discuss the anisotropy of upper critical field H_{c2} of the tricolor superlattices. Because of rather broad transition temperature width especially for $n = 5$ tricolor superlattice, there is ambiguity in determining H_{c2}. We then de-

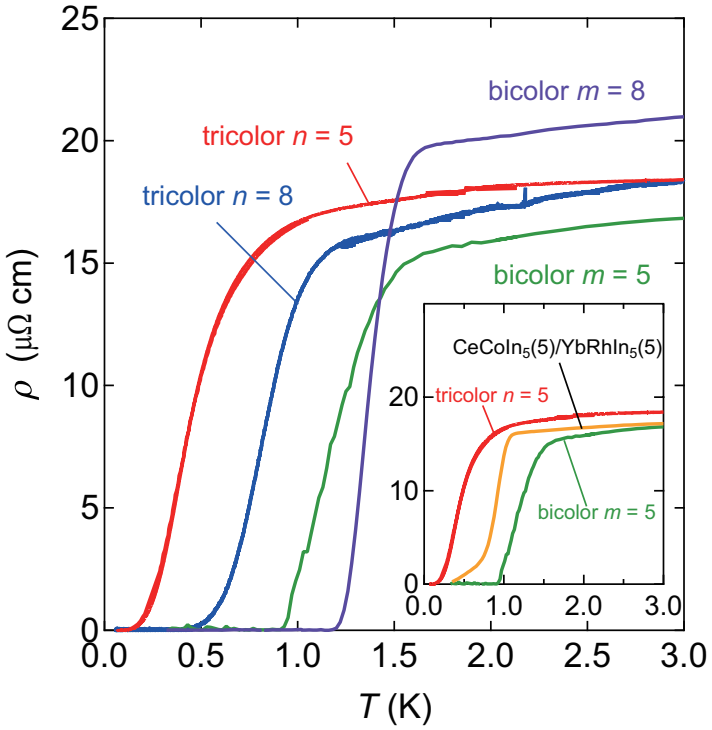

Figure 4.6: Temperature dependence of the resistivity $\rho(T)$ in the $n = 5$ and 8 tricolor $YbCoIn_5(3)/CeCoIn_5(n)/YbRhIn_5(3)$ superlattices and in the $m = 5$ and 8 bicolor $CeCoIn_5(m)/YbCoIn_5(5)$ superlattices. Inset: $\rho(T)$ for the tricolor $YbCoIn_5(3)/CeCoIn_5(n = 5)/YbRhIn_5(3)$, bicolor $CeCoIn_5(m = 5)/YbCoIn_5(5)$, and bicolor $CeCoIn_5(5)/YbRhIn_5(5)$ superlattices.

fined $H_{c2}(T)$ as the magnetic field at which the resistivity drops to 50 % of its normal state value $\rho(T,H) = 0.5\rho_{\rm N}(T)$. Figure 4.8(a) shows the anisotropy of upper critical field $H_{c2\parallel}/H_{c2\perp}$ plotted as a function of T/T_c, where $H_{c2\parallel}$ and $H_{c2\perp}$ are upper critical fields in magnetic fields parallel and perpendicular to the layer, respectively. In sharp contrast to the $CeCoIn_5$ single crystal [119] and thin film with thickness of 120 nm, the temperature dependence of $H_{c2\parallel}/H_{c2\perp}$ of the tricolor superlattices exhibits a diverging behavior upon approaching to T_c. This diverging behavior is a characteristic feature of the 2D superconductivity, which is consistent with the thickness of $CeCoIn_5$ BL comparable or less than ξ_c. We note that the diverging $H_{c2\parallel}/H_{c2\perp}$ near T_c is observed even when H_{c2} is defined by using $\rho(T,H) = 0.3\rho_{\rm N}(T)$, $0.7\rho_{\rm N}(T)$, and $0.9\rho_{\rm N}(T)$, indicating that the 2D nature of the superconductivity is irrespective of the determination of H_{c2}. The magnitude of $H_{c2\parallel}/H_{c2\perp}$ near T_c for $n = 5$ is smaller than that for $n = 8$, which is opposite to the expected behavior in conventional 2D superconductors. We point out that this reduction is explained by the suppression of the Pauli pair-breaking effect owing to the Rashba ASOC, which will be discussed later.

The salient feature of the superconductivity in the tricolor superlattices, which is distinctly different from the bicolor superlattices, is revealed by the angular and temperature dependences of H_{c2}. Figure 4.8(b) shows the angular dependence of the upper critical field $H_{c2}(\theta)$ for $n = 5$ and 8 tricolor superlattices, where θ is the angle between $\boldsymbol{H}$ and ab plane. For comparison, $H_{c2}(\theta)$ of $m = 5$ bicolor $CeCoIn_5(m)/YbCoIn_5(5)$ superlattice is also shown. In Figure 4.8(b), square of the in-plane component of H_{c2}, $[H_{c2}(\theta)\cos\theta]^2$, is plotted as a function of out-of-plane component, $H_{c2}(\theta)\sin\theta$. A cusp appears in the angular dependence near parallel field in the tricolor superlattices, which is in sharp contrast to the result of $m = 5$ bicolor superlattice that shows smooth angular dependence with no cusp. In 2D superconductor and layered superconductors, where superconducting layer thickness d is smaller than ξ_c, $H_{c2}(\theta)$ exhibits a characteristic angle dependence. When the superconductivity is destroyed by the orbital motion of Cooper pairs in the 2D plane, $H_{c2}(\theta)$ obeys the following equation derived by Tinkham [120]:

$$[H_{c2}(\theta)\cos\theta/H_{c2\parallel}]^2 = -|H_{c2}(\theta)\sin\theta/H_{c2\perp}| + 1. \tag{4.9}$$

Therefore $H_{c2}(\theta)$ is not differentiable at $\theta = 0$ and follows a cusp-like dependence at small θ. On the other hand, when the superconductivity is dominated by Pauli paramagnetic pair-breaking effect, the upper critical field is given by $H_{\rm P} = \sqrt{2}\Delta/g\mu_{\rm B}$ [121], where g is the gyromagnetic ratio, Δ is the superconducting gap amplitude, and $\mu_{\rm B}$ is the Bohr magneton. Then angular dependence of H_{c2} is determined by the anisotropy of g-factor, which is smooth for all θ, and can be described by [31]

$$[H_{c2}(\theta)\cos\theta/H_{c2\parallel}]^2 = -[H_{c2}(\theta)\sin\theta/H_{c2\perp}]^2 + 1, \tag{4.10}$$

similar to anisotropic mass model of anisotropic 3D superconductors. As shown by the solid and dashed lines in Figure 4.8(b), $H_{c2}(\theta)$ of $n = 5$ and 8 tricolor superlattices are well fitted by Eq. (4.9), while $H_{c2}(\theta)$ of $m = 5$ bicolor superlattice is well fitted by Eq. (4.10). We note that cusp-like behavior of $H_{c2}(\theta)$ near $\theta = 0$ appears even when H_{c2} is determined by using $\rho(T,H) = 0.3\rho_{\rm N}(T)$, $0.7\rho_{\rm N}(T)$, and $0.9\rho_{\rm N}(T)$, indicating

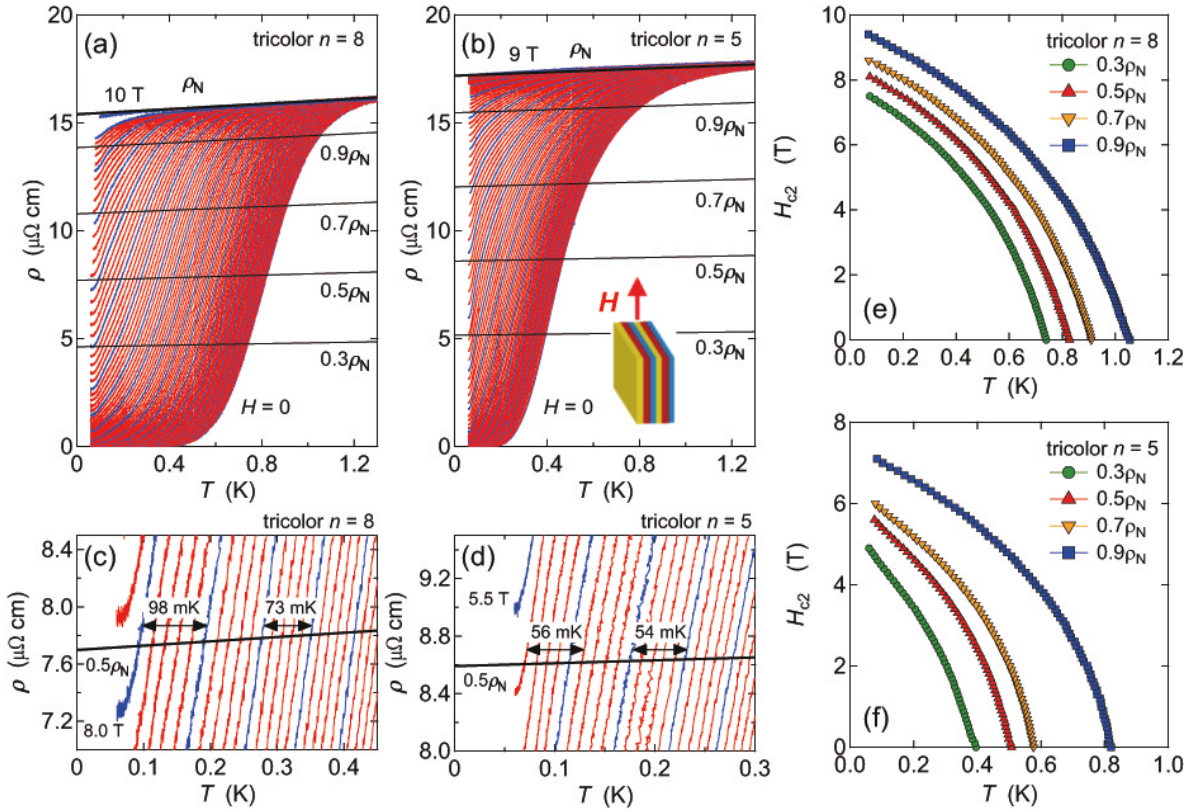

Figure 4.7: Temperature dependence of resistivity for (a) $n = 8$ and (b) $n = 5$ tricolor superlattices, respectively, in applied field parallel to the plane. Red and blue curves are taken in every 0.1 and 0.5 T, respectively. Thin solid black curve represents the normal state resistivity ρ_N, and thin solid lines represent $0.3\rho_N$, $0.5\rho_N$, $0.7\rho_N$, and $0.9\rho_N$. (c) and (d) are expanded views of (a) and (b) around $0.5\rho_N$, respectively. The arrows correspond to the shift of T_c by changing the magnetic field of 0.5 T. (e) and (f) show in-plane upper critical field defined by using four different criteria, $\rho(T, H) = 0.3\rho_N(T)$, $0.5\rho_N(T)$, $0.7\rho_N(T)$, and $0.9\rho_N(T)$, as a function of temperature for $n = 8$ and 5 tricolor superlattices, respectively.

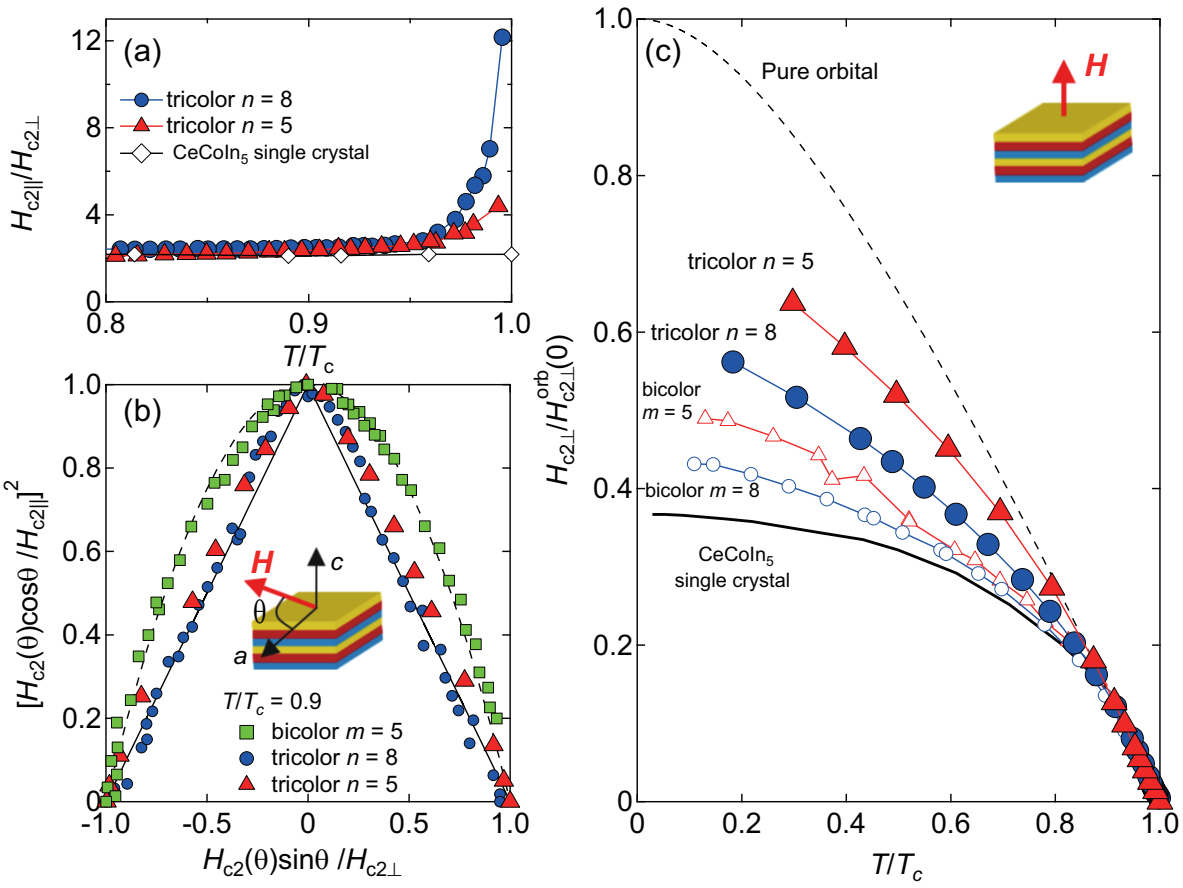

Figure 4.8: (a) The anisotropy of upper critical field H_{c2}, $H_{c2\parallel}/H_{c2\perp}$, plotted as a function of normalized temperature T/T_c for the tricolor superlattices and $CeCoIn_5$ single crystal. (b) Angular dependence of H_{c2}, $H_{c2}(\theta)$, plotted in an appropriate dimensionless form for the tricolor and bicolor $CeCoIn_5(m)/YbCoIn_5(5)$ superlattices. The solid and dashed lines represent the Tinkham's formula for a two-dimensional superconductor and the three-dimensional anisotropic mass model, which are described as $[H_{c2}(\theta)\cos\theta/H_{c2\parallel}]^2 = -|H_{c2}(\theta)\sin\theta/H_{c2\perp}| + 1$ [120] and $[H_{c2}(\theta)\cos\theta/H_{c2\parallel}]^2 = -[H_{c2}(\theta)\sin\theta/H_{c2\perp}]^2 + 1$ [31], respectively. (c) Normalized upper critical field in perpendicular fields, $H_{c2\perp}/H_{c2\perp}^{\rm orb}(0)$, as a function of T/T_c for the tricolor superlattices, compared with that for the bicolor $CeCoIn_5(m)/YbCoIn_5(5)$ superlattices with the same $CeCoIn_5$ block layer thickness. We also plot $H_{c2\perp}/H_{c2\perp}^{\rm orb}$ for $CeCoIn_5$ single crystal [119] with a strong Pauli pair-breaking effect and the WHH curve [34] without the Pauli pair-breaking effect. In (a)–(c), H_{c2} is defined by using $\rho(T,H) = 0.5\rho_{\rm N}(T)$.

the intrinsic properties of the tricolor superlattices. These results strongly suggest that the Pauli paramagnetic pair-breaking effect is dominant in the bicolor superlattices, whereas the orbital pair-breaking effect is dominant in the tricolor superlattices.

More direct evidence for the suppression of the Pauli pair-breaking effect in the tricolor superlattices is provided by $H_{c2\perp}$ normalized by the orbital limited upper critical field without Pauli effect $H_{c2\perp}^{\rm orb}$. Figure 5(c) displays $H_{c2\perp}(T)/H_{c2\perp}^{\rm orb}(0)$ of the bicolor and tricolor superlattices plotted as a function of T/T_c. Here $H_{c2\perp}^{\rm orb}(0)$ is calculated by the initial slope of $H_{c2\perp}$ at T_c by using Werthamer-Helfand-Hohenberg (WHH) formula [34], $H_{c2\perp}^{\rm orb}(0) = -0.69T_c(dH_{c2\perp}/dT)_{T_c}$. For comparison, we include the two extreme cases, $H_{c2\perp}/H_{c2\perp}^{\rm orb}(0)$ for $CeCoIn_5$ single crystal [119], in which superconductivity is dominated by Pauli pair-breaking effect [55, 119], and the WHH curve without the Pauli effect. For the bicolor superlattices, $H_{c2\perp}/H_{c2\perp}^{\rm orb}(0)$ is enhanced from that of bulk $CeCoIn_5$ only slightly, indicating that the superconductivity is still dominated by Pauli effect, consistent with the angular variation of $H_{c2}(\theta)$. What is remarkable is that $H_{c2\perp}/H_{c2\perp}^{\rm orb}(0)$ of the tricolor superlattices is dramatically enhanced from that of the bicolor superlattices with the same $CeCoIn_5$ BL thickness. In particular, $H_{c2\perp}/H_{c2\perp}^{\rm orb}(0)$ of $n = 5$ tricolor superlattice is close to the WHH curve with no Pauli effect. This is again consistent with $H_{c2}(\theta)$. The enhancement of $H_{c2\perp}/H_{c2\perp}^{\rm orb}(0)$ is attributed to the enhancement of the Pauli limiting field, leading to the increase of the relative importance of the orbital pair-breaking effect compared to the Pauli pair-breaking effect.

There are several possible origins for the enhancement of the Pauli limiting field in the tricolor superlattices, including (1) reduction of g-value, (2) enhancement of Δ/T_c, and (3) the Rashba effect. We point out that both (1) and (2) are unlikely because of the following reasons. Since the g-value is determined by the crystalline electric field, the g-value of the tricolor superlattices should be close to the value of the bicolor superlattices with very similar crystal structure. Moreover, in $CeRhIn_5$ with similar crystal and electronic structure, g-value is insensitive to the applied pressure [33]. Recent site-selective-nuclear magnetic resonance experiments of the bicolor superlattices reveal that the AFM fluctuations in $CeCoIn_5$ BLs are suppressed with decreasing m [82], implying that pairing interaction is expected to be weakened with decreasing $CeCoIn_5$ layer thickness. However, this tendency is opposite to the observed enhancement of Pauli limiting field in the bicolor and tricolor superlattices with thinner BL thickness. We stress that the dramatic suppression of the Pauli effect in the tricolor superlattices is naturally explained by the Rashba effect [85, 122].

The Zeeman interaction given by $\mu_{\rm B}\boldsymbol{g}(\boldsymbol{k})\cdot\boldsymbol{H}$ leads to anisotropic suppression of the Pauli pair-breaking effect; Strong suppression of the Pauli effect occurs for $\boldsymbol{H} \parallel [0\,0\,1]$ where $\boldsymbol{g}(\boldsymbol{k})\cdot\boldsymbol{H} = 0$ [100, 102, 103], while the suppression is weaker for $\boldsymbol{H} \parallel ab$ since $\boldsymbol{g}(\boldsymbol{k}) \perp \boldsymbol{H}$ is not always satisfied. Therefore, $H_{c2\perp}$ is more strongly enhanced than $H_{c2\parallel}$ by the Rashba effect, giving rise to the reduction of $H_{c2\parallel}/H_{c2\perp}$. Since the fraction of the noncentrosymmetric interface increases rapidly with decreasing n, the magnitude of $H_{c2\parallel}/H_{c2\perp}$ near T_c for $n = 5$ tricolor superlattices is smaller than that for $n = 8$.

Thus both the angular and temperature dependences of H_{c2} indicate that the Pauli paramagnetic pair breaking effect, which is dominant not only in $CeCoIn_5$ single crystal but also in the centrosymmetric bicolor superlattices, can be substantially reduced in

the tricolor superlattices. Here we comment on the slight enhancement of $H_{c2\perp}/H_{c2\perp}^{\rm orb}(0)$ from bulk $CeCoIn_5$ value in the bicolor superlattices. This has been attributed to the local inversion symmetry breaking at the top and bottom interfaces of $CeCoIn_5$ layers at the immediate proximity to $YbCoIn_5$ BLs [80, 81]. In tricolor superlattices, $H_{c2\perp}/H_{c2\perp}^{\rm orb}(0)$ approaches orbital limit with decreasing n. This demonstrates that the Rashba ASOC incorporated into 2D $CeCoIn_5$ BLs due to the built-in broken inversion symmetry is largely tunable by changing the BL thickness in the present tricolor superlattices.

4.3.3 A possible exotic superconducting state in parallel field

Next, we investigate the superconducting state of the tricolor superlattices in parallel field ($\boldsymbol{H} \parallel ab$). Figure 6(a) shows the T-dependence of $H_{c2\parallel}/T_c$ for the tricolor superlattices, along with the data for $CeCoIn_5$ single crystal and the bicolor superlattices with the same $CeCoIn_5$ BL thickness. It is obvious that $H_{c2\parallel}/T_c$ of the tricolor superlattices is largely enhanced from those of the bicolor superlattices and single crystal. Similar to the perpendicular field case, this enhancement can be attributed to the Rashba effect, because in-plane field component which satisfies $\boldsymbol{H} \perp \boldsymbol{g}(\boldsymbol{k})$ for certain momenta $\boldsymbol{k}$ does not cause the Zeeman splitting, giving rise to the reduction of the Pauli paramagnetic effect.

Figure 4.9(a) shows that each system exhibits characteristic T-dependence of $H_{c2\parallel}$. This can be seen clearly in Fig. 4.9(b), which plots $r = -d(H_{c2\parallel}/T_c)/d(T/T_c)$ against $t = T/T_c$. In $CeCoIn_5$ single crystal, $r(t)$ decreases linearly with decreasing t and goes to zero at $t \to 0$, indicating that $H_{c2\parallel}$ tends to saturate at low temperatures. In $m = 5$ and 8 bicolor superlattices, $r(t)$ decreases linearly with finite residual value at $t \to 0$. Markedly different temperature dependence of $H_{c2\parallel}$ is observed in the tricolor superlattices. In $n = 8$ superlattice, $r(t)$ shows a deviation from T-linear behavior below $t \approx 0.25$. For $n = 5$, $r(t)$ increases after showing a distinct minimum at $t \approx 0.28$ as t is lowered. These results indicate the upturn behavior of $H_{c2\parallel}(T)$ at low temperatures in the tricolor superlattices (see red and blue arrows in Figs. 4.9(a) and 4.9(b)). We stress that the observed upturn behavior of $H_{c2\parallel}(T)$ is intrinsic because of the following reasons. First of all, Figs. 4.9(c) and 4.9(d) show $r(t)$ determined by four different criteria [$\rho(T, H) = 0.3$, 0.5, 0.7, and $0.9\rho_{\rm N}(T)$] for $n = 8$ and 5 tricolor superlattices, respectively. For $n = 8$, all $r(t)$ data collapse into a single curve, indicating that the deviation from T-linear behavior is independent of the criteria used. Although the data for $n = 5$ do not collapse into a single curve, the fact that all $r(t)$ curves exhibit increasing behavior at low temperature suggests that the upturn of $H_{c2\parallel}(T)$ occurs at the onset, middle, and tail parts of the resistive transition. Secondly, as shown in Fig. 4.7(d), the resistive transition taken from 4 T to 5.5 T with an interval of $\Delta H = 0.1$ T around $\rho(T, H) = 0.5\rho_{\rm N}(T)$ exhibits a parallel shift with similar change in T_c, ΔT_c, indicating that $\Delta T_c/\Delta H$ is constant even at low T. This is in sharp contrast to the other superconductors in which $\Delta T_c/\Delta H$ increases rapidly as $T \to 0$. Thirdly, in Figs. 4.9(c) and 4.9(d), $r(t)$ of tricolor superlattices is compared with that of the WHH curve with no Pauli pair-breaking effect. We note that $r(t)$ of conventional

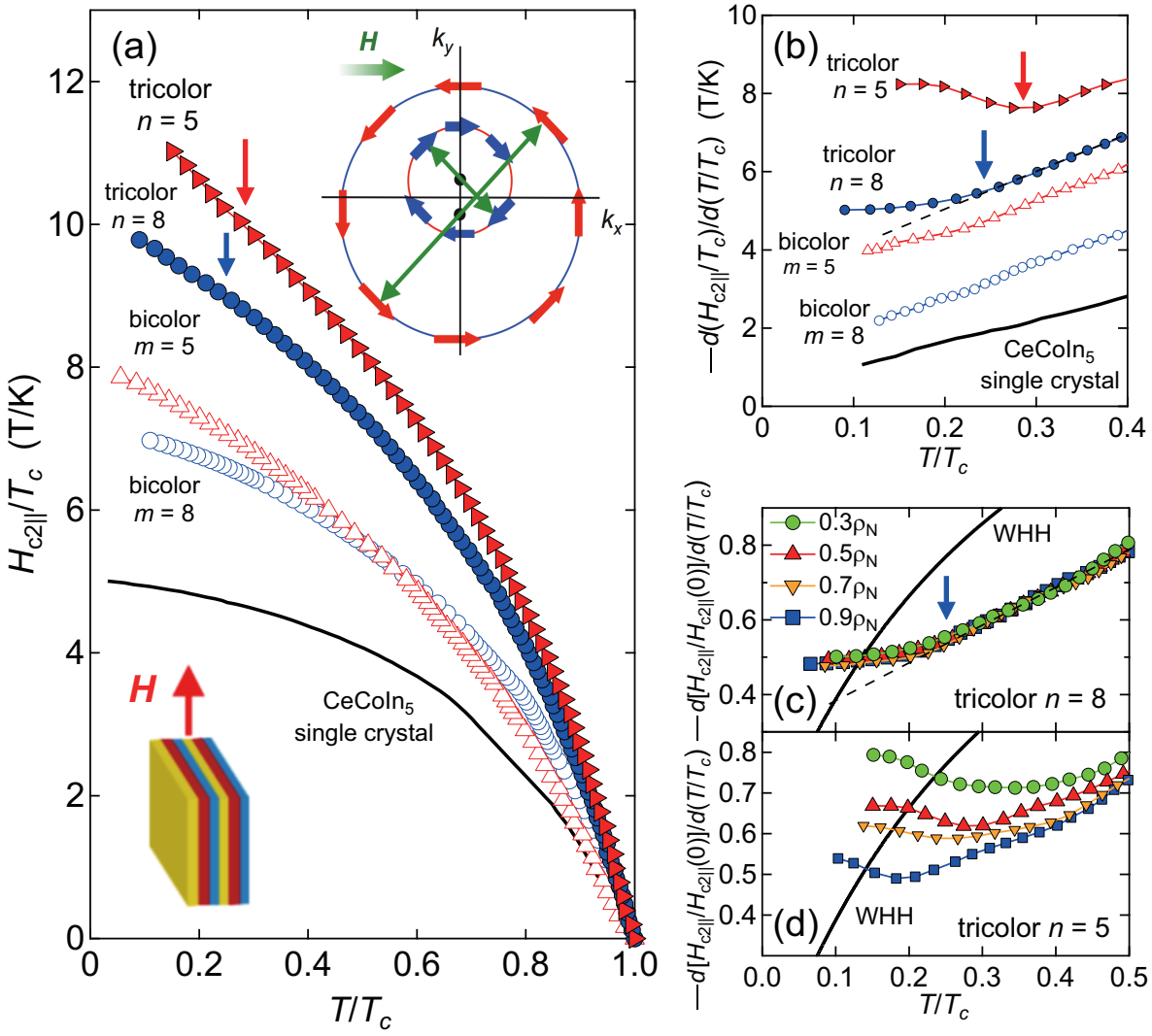

Figure 4.9: (a) Reduced upper critical field in parallel fields, $H_{c2\parallel}/T_c$, as a function of T/T_c for the tricolor superlattices, compared with that for the bicolor $CeCoIn_5(m)/YbCoIn_5(5)$ superlattices with the same $CeCoIn_5$ block layer thickness. $H_{c2\parallel}$ is determined by using $\rho(T,H) = 0.5\rho_N(T)$. We also plot $H_{c2\parallel}/T_c$ for $CeCoIn_5$ single crystal. Inset illustrates schematic figure of the Fermi surfaces under parallel magnetic fields. Arrows on the Fermi surfaces indicate spins. Fields parallel to x axis shifts the center of the Rashba-split small and large Fermi surfaces by $\boldsymbol{q_M}$ along $+y$ and $-y$ directions, respectively. Pairing occurs between the states of $\boldsymbol{k}+\boldsymbol{q_M}$ and $-\boldsymbol{k}+\boldsymbol{q_M}$, leading to a gap function with spatial modulation, e.g., in a form of $\Delta(\boldsymbol{r}) = \Delta_0 e^{i\boldsymbol{q_M}\cdot\boldsymbol{r}}$ [111]. (b) Temperature derivative of $H_{c2\parallel}$, represented as $r = -d(H_{c2\parallel}/T_c)/d(T/T_c)$, is plotted as a function of $t = T/T_c$. $r(t)$ shows a minimum for the $n = 5$ tricolor superlattice (red arrow). For $n = 8$, $r(t)$ shows a deviation from T-linear temperature dependence (dashed line) below $t \sim 0.25$ (blue arrow). (c) and (d) shows $r(t)$, replotted as $-d[H_{c2\parallel}/H_{c2\parallel}(0)]/d(T/T_c)$, for (c) $n = 5$ and $n = 8$ tricolor superlattices, respectively. Here we use $H_{c2\parallel}$ determined by using different criteria, $\rho(T,H) = 0.3\rho_N(T)$, $0.5\rho_N(T)$, $0.7\rho_N(T)$ and $0.9\rho_N(T)$. Solid lines are $r(t)$ calculated from the WHH formula.

superconductors cannot exceed $r(t)$ of the WHH curve. Remarkably, in both $n = 8$ and 5 tricolor superlattices, $r(t)$ exceeds that of the WHH curve irrespective of the H_{c2} criteria. Based on these results, we conclude that the upturn behavior of $H_{c2\parallel}(T)$ is a unique property of the tricolor superlattices.

We note that the upturn behavior of $H_{c2\parallel}(T)$ is not caused by the multiband or strong coupling effect, because both of them give positive curvature of upper critical field immediately below T_c [123,124]. We point out that the upturn of upper critical field at low temperature may be a signature of new superconducting phase. It is well known that such an upturn occurs by a formation of the Fulde-Ferrell-Larkin-Ovchinnikov (FFLO) state [125], in which the pairing occurs between the Zeeman-split part of the Fermi surface, as reported in layered organic superconductors in parallel field [126]. The FFLO state is characterized by the formation of Cooper pairs with nonzero total momentum ($\boldsymbol{k} + \boldsymbol{q} \uparrow$, $-\boldsymbol{k} + \boldsymbol{q} \downarrow$) instead of the ordinary BCS pairs ($\boldsymbol{k} \uparrow$, $-\boldsymbol{k} \downarrow$). In the lowest Landau level solution, superconducting order parameter is spatially modulated as $\cos(\boldsymbol{q} \cdot \boldsymbol{r})$ with $\boldsymbol{q} \parallel \boldsymbol{H}$ [125]. However, the FFLO state is highly unlikely to be the origin of upturn because the Rashba splitting well exceeds the Zeeman energy ($\alpha_R \gg \mu_{\rm B} H$) in the present tricolor superlattices.

Recently the helical and stripe superconducting states have been proposed in 2D superconductors with global ISB in magnetic field parallel to the 2D plane [111, 127]. These states appear as a result of the shift of the Fermi surface with the Rashba ASOC by the external magnetic field. When the magnetic field is applied along the $\hat{\boldsymbol{x}}$ axis ($\boldsymbol{H} = H\hat{\boldsymbol{x}}$), the centers of the two Fermi surfaces with different spin helicity are shifted along $\hat{\boldsymbol{y}}$ in opposite directions, as illustrated in the inset of Fig. 4.9(a). Similar to the FFLO state, these states are characterized by the formation of Cooper pairs ($\boldsymbol{k}+\boldsymbol{q}_M$, $-\boldsymbol{k}+\boldsymbol{q}_M$), where $\boldsymbol{q}_M = m_q \mu_{\rm B} H \hat{\boldsymbol{y}}/|\boldsymbol{k}|$ ($\perp \boldsymbol{H}$) with m_q the mass of the quasiparticles. The phase of superconducting order parameter is modulated as $\Delta(\boldsymbol{r}) = \Delta_0 e^{i\boldsymbol{q_M}\cdot\boldsymbol{r}}$ in the helical superconducting state and $\Delta(\boldsymbol{r}) = \Delta_1 e^{i\boldsymbol{q_M}\cdot\boldsymbol{r}} + \Delta_2 e^{-i\boldsymbol{q_M}\cdot\boldsymbol{r}}$ in the stripe state. It has been shown that the formation of helical and stripe superconducting states enhances $H_{c2\parallel}$ at low temperature, giving rise to the upturn behavior of $H_{c2\parallel}$ [111, 127].

Although the presence of helical or stripe phases should be scrutinized, the facts that anomalous upturn of $H_{c2\parallel}$ is observable only in the tricolor superlattices and is more pronounced in the superlattices with smaller n imply that the Rashba ASOC induced by the global ISB plays an essential role in producing a high field superconducting phase. More direct measurements which sensitively detect the change of superconducting order parameter, such as scanning tunneling microscope [53, 54] and site-selective nuclear magnetic resonance [82, 128, 129], are strongly desired.

4.4 Summary

In this study, using a state-of-the-art MBE technique, we have designed and fabricated tricolor heavy-fermion superlattice, in which strongly correlated 2D superconductor $CeCoIn_5$ is sandwiched by nonmagnetic metals $YbCoIn_5$ and $YbRhIn_5$ with different electronic structure. By stacking three compounds repeatedly in an asymmetric sequence such as $YbCoIn_5/CeCoIn_5/YbRhIn_5$, we can introduce the global ISB along

the stacking direction. We find that the Rashba ASOC induced by the global ISB in these tricolor heavy-fermion superlattices leads to profound changes in the superconducting properties of $CeCoIn_5$ with atomic thickness. The upper critical field exhibits unusual temperature and angular dependence, which are essentially different from those in $CeCoIn_5$ single crystals. These results indicate that the Rashba ASOC induced in the tricolor superlattices leads to the strong suppression of the Pauli paramagnetic pair-breaking effect. We also demonstrate that the magnitude of the Rashba ASOC incorporated into the 2D $CeCoIn_5$ BLs is largely controllable by changing the thickness of $CeCoIn_5$ BLs.

Bulk $CeCoIn_5$ has 3D anisotropic electronic structure and hosts an abundance of fascinating superconducting properties. The $d_{x^2-y^2}$ symmetry is well established [53–56, 64, 116]. At low temperature in magnetic field applied parallel to the *ab* plane, a possible appearance of exotic superconducting phase, such as FFLO [125, 128–130, 147], π-triplet pairing state [131], and coexistence of superconductivity and field-induced magnetically ordered phase (Q-phase) [141, 148] has attracted intense attention in recent years in an effort to search for exotic pairing states. It has been recently pointed out that in 2D noncentrosymmetric superconductors with nodes in the superconducting gap, the topological superconducting state is stabilized with no fine tuning of parameters, in contrast to those without nodes [132, 133]. Therefore, the fabrication of tricolor superlattices containing *d*-wave superconducting layers offers the prospect of achieving even more fascinating pairing states than bulk $CeCoIn_5$, such as helical and stripe superconducting states [111], a pair-density-wave state [134], complex stripe state [135], a topological crystalline superconductivity [136], and Majorana fermion excitations [133], in strongly correlated electron systems.

Chapter 5

Tuning the pairing interaction through interfaces in $CeCoIn_5/CeRhIn_5$ hybrid superlattices

5.1 Introduction

In diverse families of strongly correlated electron systems, including cuprates, iron pnictides, and heavy-fermion compounds, superconductivity is often found near a quantum critical point (QCP) where a magnetic phase vanishes in the limit of zero temperature. In these materials, it is established that Cooper pairs are not bound together through phonon exchanges but instead through exchanges of some other kind, such as spin fluctuations [1, 2, 7]. One of the unusual emergent electronic states near the QCP is the microscopic coexistence of superconducting and magnetically ordered phases both involving the same charge carriers. Moreover, superconductivity is frequently the strongest near the QCP, suggesting that the proliferation of critical magnetic excitations emanating from the QCP plays a vital role in Cooper pairing. Despite tremendous research, however, the entangled relationship between superconductivity and magnetism has mainly remained elusive.

Recently, the realization that interactions between superconducting electrons and bosonic excitations through an atomic interface can have a profound influence on Cooper pairing has raised the exciting possibility of a new way of controlling superconductivity. For example, when a monolayer FeSe film grown on a $SrTiO_3$ substrate, the coupling between the FeSe electrons and $SrTiO_3$ phonons enhance the Cooper pairing, giving rise to the superconducting transition temperature T_c which is almost an order of magnitude higher than that of the bulk FeSe and highest among all known iron-based superconductors [137–140].

This discovery raises the possibility of a magnetic analog in which the pairing interaction is influenced by magnetic fluctuations though an interface between an unconventional superconductor and a magnetic metal. This concept is illustrated schematically

in Figs. 5.1(a) and 5.1(b). Besides allowing a new approach to revealing the entangled relationship between magnetism and unconventional superconductivity, this concept has the advantage that magnetic excitations are tunable as a magnetic transition is driven toward zero temperature, unlike phonon excitations in $SrTiO_3$. The state-of-the-art molecular beam epitaxy (MBE) technique enables the realization of this idea through the fabrication of artificial heavy-fermion superlattices with alternating layers of Ce-based heavy fermion superconductors and magnets that are atomic layer thick [75, 76, 79]. These artificially engineered materials are particularly suitable systems to elucidate the mutual interaction through the interface, providing a new platform to study the interplay of competing orders.

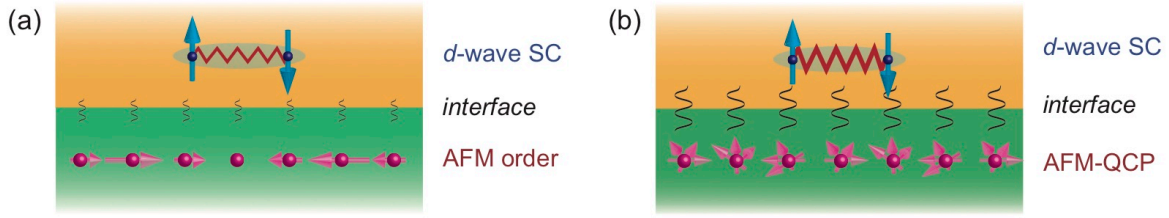

Figure 5.1: (a) Schematic figure of the interaction between d-wave superconducting (SC) state and static antiferromagnetic (AFM) order via the interface. (b) Interaction between two competing orders under pressure near a QCP, where AFM order disappears.

As shown in the introduction of this thesis, the layered heavy fermion compounds $CeMIn_5$ (M = Co, Rh) are ideal model systems in which the interplay between magnetism and superconductivity can be explored, because of their high purity and small energy scales [59, 141, 142]. They have similar Fermi surface structures and similar pressure-temperature (p-T) phase diagrams. At ambient pressure, $CeCoIn_5$ is a superconductor ($T_c = 2.3\,\mathrm{K}$) with $d_{x^2-y^2}$-wave symmetry [53–55]. The normal state possesses non-Fermi-liquid properties in zero fields, including T-linear resistivity, indicative of a nearby underlying QCP [37, 143]. In contrast, $CeRhIn_5$ orders antiferromagnetically at atmospheric pressure ($T_N = 3.8\,\mathrm{K}$) [62]. Its magnetic transition is suppressed by applying pressure and the ground state becomes purely superconducting state at $p > p^* \approx 1.7$ GPa, indicating the presence of a pressure-induced QCP [16,33,36,64]. As disorder may seriously influence physical properties especially near a QCP, there is a great benefit in examining quantum critical systems which are stoichiometric, and hence, relatively disorder free; both compounds are ones of a small number of such systems. Both host a wide range of fascinating superconducting properties including an upper critical field H_{c2} that is limited by extremely strong Pauli pair-breaking [33, 55].

5.2 Experimental details

To realize hybrid heterostructures of a d-wave superconductor and an antiferromagnet, we fabricated the hybrid superlattices $CeCoIn_5(n)/CeRhIn_5(m)$ with c-axis

oriented structure are grown on a MgF_2 substrate by the MBE technique. The substrate temperature was pre-annealed at 650 °C for 2 hours, then kept at 450 °C during the growth of the buffer layer $CeIn_3$ (30 nm). Subsequently, 15-unit-cell-thick (UCT) $YbCoIn_5$ was grown at 550 °C. After these buffer layers, n-UCT $CeCoIn_5$ and m-UCT $CeRhIn_5$ were grown alternatingly, forming a $CeCoIn_5(n)/CeRhIn_5(m)$ superlattice with a typical total thickness of 300 nm. The repetitions of superlattices are 28, 40, and 66 times for $n = m = 7$, 5, and 3, respectively. The deposition rate was monitored by a crystal rate monitor and the typical growth rate was 0.1–0.2Å/s.

To control the magnitude of magnetic fluctuations in antiferromagnetic BLs in the hybrid superlattices as described in 5.1(a) and (b), we established pressure experiments on heavy-fermion thin films and superlattices for the first time, to our knowledge. Using a piston-cylinder cell with Daphne oil 7373 as the pressure transmitting medium, we have successfully performed high-pressure resistivity measurements under hydrostatic pressure up to 2.4 GPa. The pressure inside the cell was determined by the superconducting transition temperature of Pb, measured by quasi-4 wire resistivity. Electrical in-plane resistivity was measured with a standard four-probe method with LR-700 ac resistance bridge in a hand-made ^{4}He pumping probe for 1.6–300 K at zero magnetic fields and ^{3}He-cryostat (Heliox VL) system for 0.3–300 K under magnetic fields up to 7 T for field perpendicular direction and up to 1 T for parallel direction.

5.3 Results and Discussion

5.3.1 Characterization

We fabricated hybrid superlattices with alternating block layers (BLs) of n-UCT $CeCoIn_5$ and m-UCT $CeRhIn_5$, $CeCoIn_5(n)/YbCoIn_5(m)$ with $n = m = 7$, 5, 3. In this section, we focus on the characterization of these superlattices. The superlattice structures were confirmed by transmission electron microscopy (TEM) and electron energy loss spectroscopy (EELS), X-ray diffraction (XRD), and reflection high-energy electron diffraction (RHEED). The details are given in the following sections.

TEM and EELS

Figure 5.2(a) display high-resolution cross-sectional TEM image along the (1 0 0) direction for the $CeCoIn_5(5)/CeRhIn_5(5)$ superlattice. A stacking structure of 5-UTC $CeCoIn_5$ BLs and 5-UTC $CeRhIn_5$ BLs is clearly resolved from the difference of the brightness of $CoIn_2$ layers and $RhIn_2$ layers. Figure 5.2(b) display an EELS image of the same superlattice. The intensities of Ce and In atoms are almost constant within both $CeCoIn_5$ and $CeRhIn_5$ BLs. Rh and Co atoms are confined in $CeRhIn_5$ and $CeCoIn_5$ BLs, respectively, demonstrating sharp interfaces with no discernible atomic inter-diffusion between the neighboring BLs.

XRD

Figure 5.3(a) shows XRD pattern around (0 0 4) peak for $CeCoIn_5(5)/CeRhIn_5(5)$

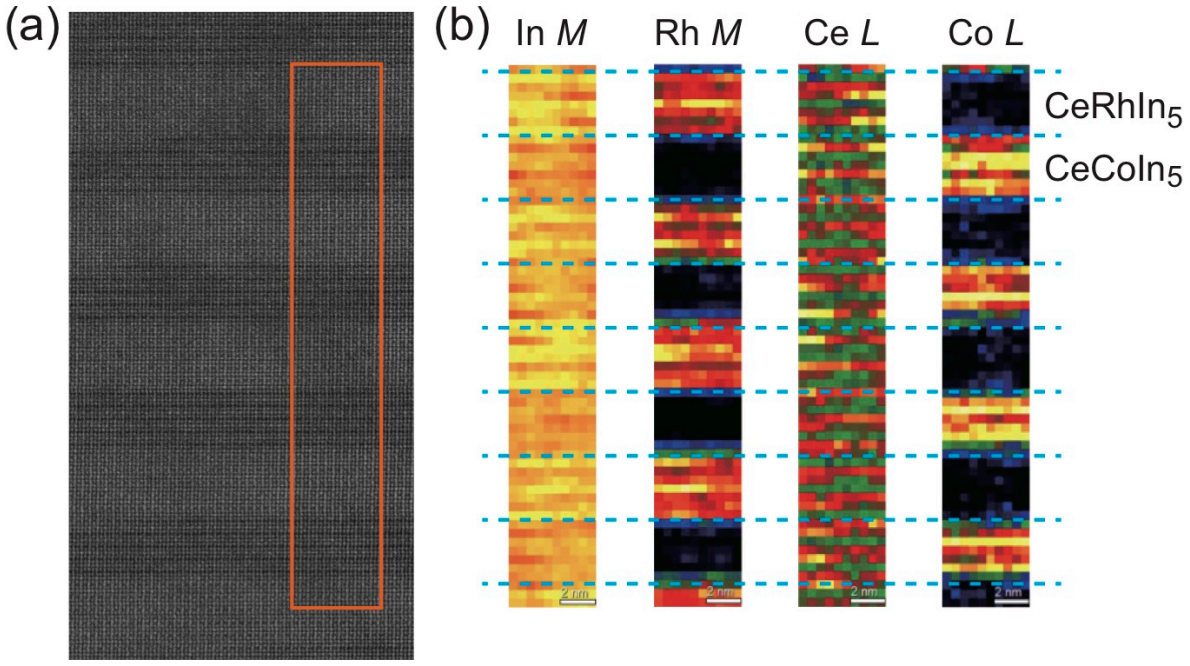

Figure 5.2: (a), (b) High-resolution cross-sectional (a) TEM and (b) EELS images for $CeCoIn_5(5)/CeRhIn_5(5)$ superlattice. The EELS images were measured in the boxed area in the TEM image for In M, Rh M, Ce L, and Co L edges.

superlattice and the step-model simulations ignoring interface and layer thickness fluctuations. In the simulation, only the instrumental resolution of 0.18° is taken into account as a broadening factor by using a Gaussian distribution function. The width of the main (0 0 4) peak is comparable to that of the simulation, demonstrating a high quality of the crystal. Although a satellite peak at $2\theta \sim 49.5°$ is not clearly resolved, the position and height of a satellite peak at $2\theta \sim 47°$ are well reproduced by the simulation. We obtain the c-axis lattice constant of 7.536 Å, which is 0.2% smaller than that of $CeCoIn_5$ single crystal (7.551 Å). The a-axis lattice constant estimated by $a = (a_{CeCoIn5} + a_{CeRhIn5})/2$ is 4.633 Å, which is 0.4% larger than that of $CeCoIn_5$ single crystal (4.613 Å).

RHEED

Figure 5.3(b) shows RHEED image of $CeCoIn_5(5)/CeRhIn_5(5)$. A clear RHEED pattern is observed during the growth, demonstrating the epitaxial growth of each layer with an atomically flat surface. Similar RHEED patterns were also observed for other superlattices, regardless of the thickness modulation of $CeCoIn_5$ BLs and $CeRhIn_5$ BLs.

5.3.2 $CeCoIn_5$ and $CeRhIn_5$ thin films

Figures 5.4(a) and 5.4(b) depict the temperature (T) dependence of resistivity for $CeCoIn_5$ and $CeRhIn_5$ thin films, under pressure. We used the same criterion for determining T_c and T_N as in thin films and superlattices. The superconducting transi-

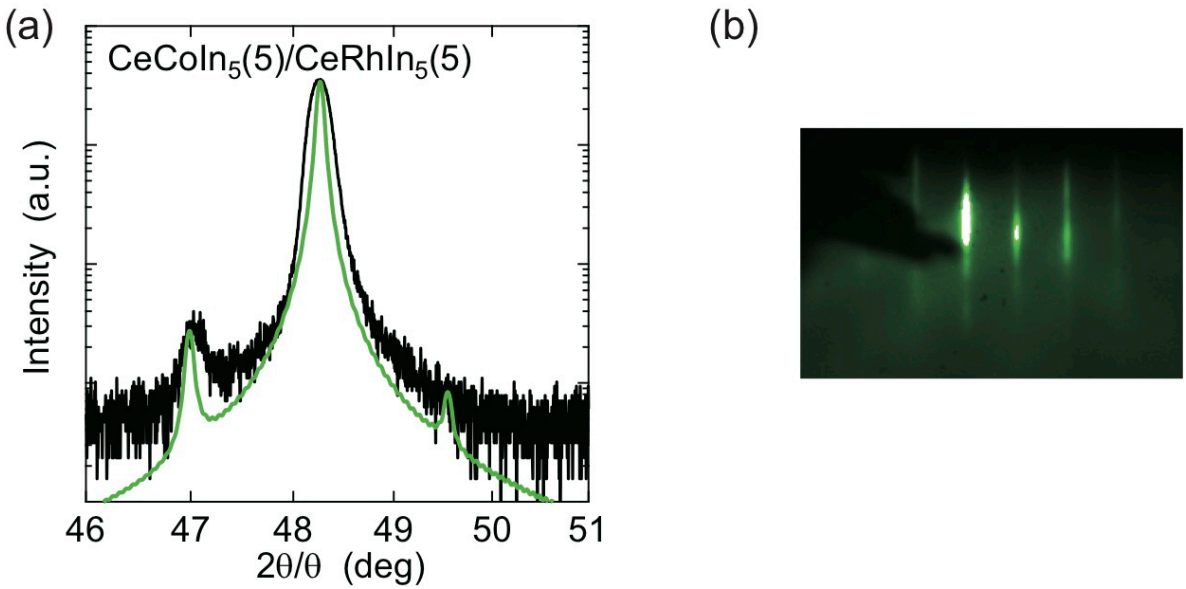

Figure 5.3: (a) Cu $K\alpha_1$ X-ray diffraction pattern for $CeCoIn_5(5)/CeRhIn_5(5)$ superlattice with a total thickness of 300 nm. In addition to the (0 0 4) main peak at $2\theta \sim 48°$, satellite peaks are observed. The positions of the satellite peaks and their asymmetric heights can be reproduced by the step-model simulations (green line) ignoring interface and layer-thickness fluctuations. (b) The reflection high-energy electron diffraction (RHEED) image taken after the crystal growth. The streak patterns in the RHEED image indicate the epitaxial growth of each layer with atomic flatness. The streak patterns are observed during crystal growth.

tion temperature T_c is determined by the midpoint of the resistive transition. In bulk $CeRhIn_5$, it has been reported that the temperature derivative of resistivity, $d\rho(T)/dT$, exhibits a sharp peak at T_N. Figure 5.4(c) depicts $d\rho(T)/dT$ at low temperatures for $CeRhIn_5$ thin film. At ambient pressure, a distinct peak is observed, indicating the AFM transition at $T_N = 3.7$ K. Such a peak structure is also observed at $p = 0.9$, 1.6, and 1.8 GPa. T_N initially increases with pressure, but it decreases with increasing pressure following a maximum at ~ 1.1 GPa. On the other hand, the signature of AFM transition vanishes at 2.4 GPa. Superconductivity develops with broad resistive transition at $p > 1$ GPa where it coexists with the AFM order. Sharp superconducting transition is observed at 2.4 GPa.

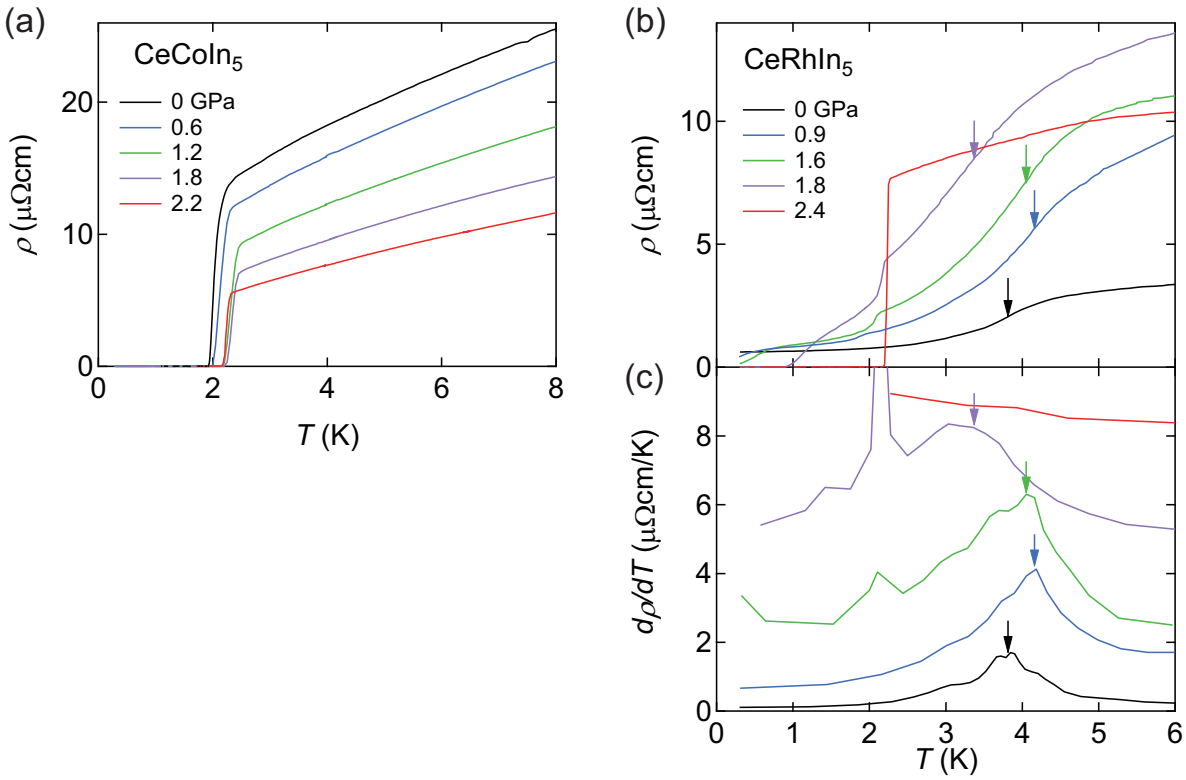

Figure 5.4: (a) Temperature dependence of the resistivity of $CeCoIn_5$ thin films with thickness of 300 nm for different pressures. (b) Temperature dependence of the resistivity of $CeRhIn_5$ thin films with thickness of 300 nm for different pressures. Sharp superconducting transition is observed at 2.4 GPa (c) Temperature derivative of the resistivity for $CeRhIn_5$ thin films.The distinct peak accompanied by the AFM transition appears, indicated by arrows.

Figures 5.5(a) and 5.5(b) depict the p-T phase diagrams of thin films of $CeCoIn_5$ and $CeRhIn_5$. The p-T phase diagrams of both films are essentially those of single crystals. T_c (= 2.0 K) in the $CeCoIn_5$ thin film, however, is slightly reduced from the bulk value, whereas T_N (= 3.7 K) of $CeRhIn_5$ thin film is almost the same as that in a single crystal. With pressure, T_c of the $CeCoIn_5$ thin film increases and shows a broad peak near $p \sim 1.7$ GPa. Similar to $CeRhIn_5$ single crystals [33,64], superconductivity in

the thin films develops at $p \gtrsim 1$ GPa, where it coexists with magnetic order. In analogy to $CeRhIn_5$ single crystals, there appears to be a purely superconducting state at $p \gtrsim 2.1$ GPa, which is a slightly higher pressure than that required to remove evidence for AFM order in single crystals.

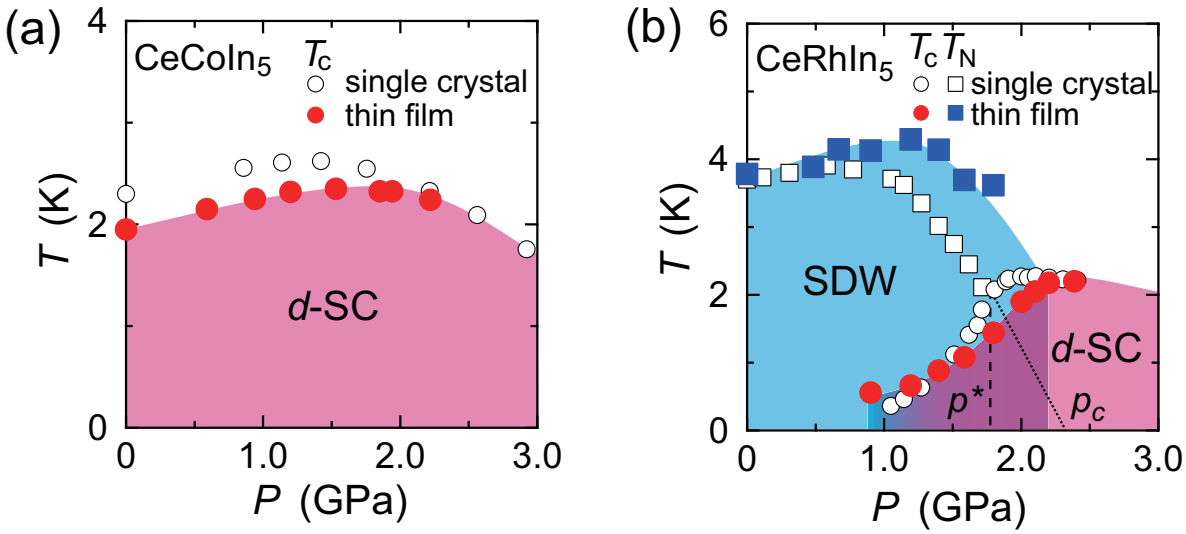

Figure 5.5: (a), (b) p-T phase diagrams of thin films and single crystals of (a) $CeCoIn_5$ and (b) $CeRhIn_5$. (c) Temperature dependence of the resistivity of $CeCoIn_5$ thin film at ambient pressure and at $p = 2.1$ GPa. (d), (e) Temperature dependence of the resistivity (solid lines, left axes) and its temperature derivative $d\rho(T)/dT$ (dotted lines, right axes) for $CeRhIn_5$ thin film and $CeCoIn_5(5)/CeRhIn_5(5)$ superlattice at ambient pressure and $p = 2.1$ GPa, respectively.

5.3.3 $CeCoIn_5/YbCoIn_5$ and $CeRhIn_5/YbRhIn_5$ superlattices

Figures 5.6(a) and 5.6(b) shows the T-dependence of $\rho(T)$ and $d\rho(T)/dT$, respectively, for $CeRhIn_5(5)/YbRhIn_5(7)$ superlattice under pressure in zero magnetic field. The resistive transition due to superconductivity is observed above 1.6 GPa. However, zero resistivity is not attained even when the AFM order is suppressed. Figure 5.6(c) and 5.6(d) shows the p-T phase diagrams of the $CeRhIn_5(5)/YbRhIn_5(7)$ and $CeCoIn_5(5)/YbCoIn_5(5)$ superlattices, respectively. Although T_N and T_c are suppressed compared with single crystals [76,77], the pressure dependences are mostly those of single crystals.

5.3.4 $CeCoIn_5(5)/CeRhIn_5(5)$ hybrid superlattices

Figures 5.7(a) and 5.7(b) shows the T-dependence of $\rho(T)$ and $\mathrm{d}\rho(T)/\mathrm{d}T$, respectively, for $CeCoIn_5(5)/CeRhIn_5(5)$ superlattice under pressure in zero magnetic field. A distinct peak in $\mathrm{d}\rho/\mathrm{d}T$ associated with the AFM transition can be seen in addition

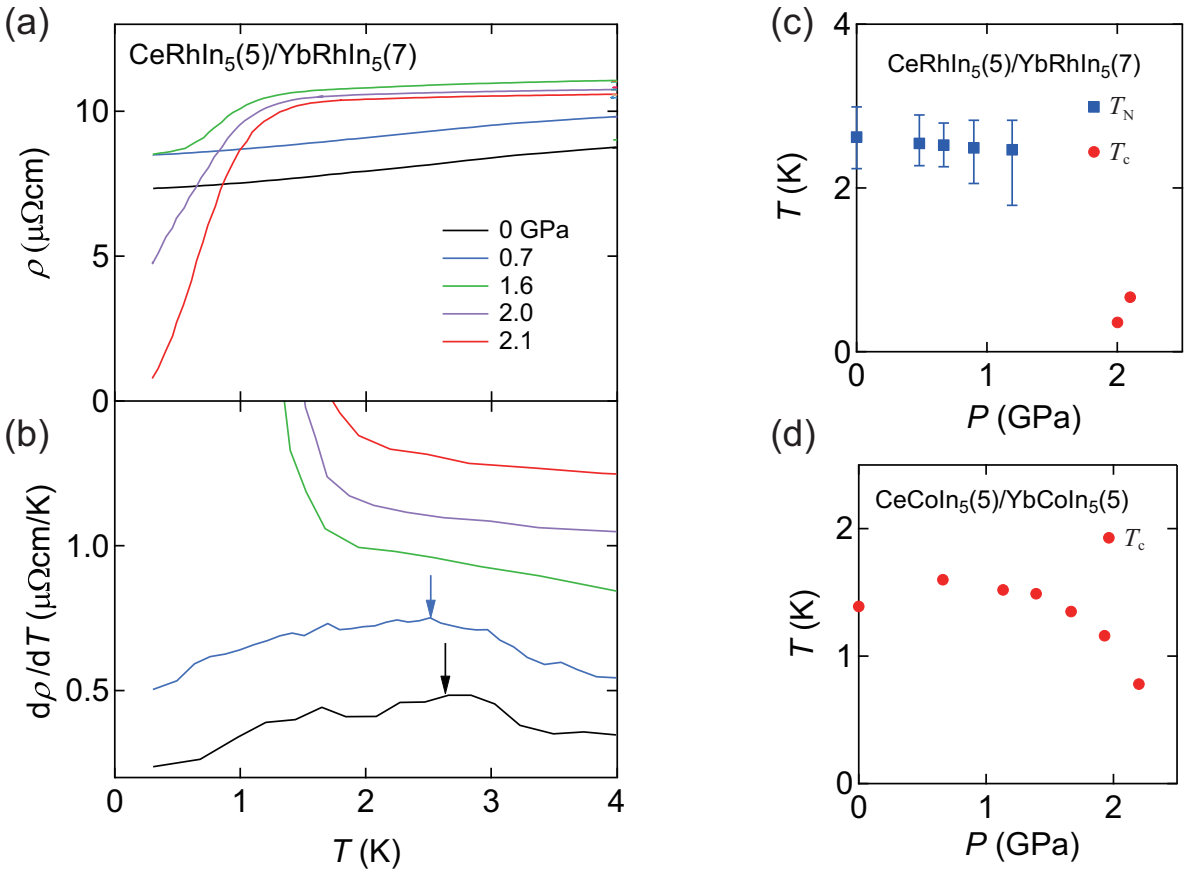

Figure 5.6: (a) Temperature dependence of the resistivity of $CeRhIn_5(5)/YbRhIn_5(7)$ superlattice under pressure. (b) Temperature derivative of the resistivity $d\rho(T)/dT$. The AFM transition temperature is determined by the peak of $d\rho(T)/dT$. (c) p-T phase diagram of $CeRhIn_5(5)/YbRhIn_5(7)$ determined by the resistivity. Blue squares and red circles represent the AFM and superconducting transition temperatures, respectively. (d) p-T phase diagram of $CeCoIn_5(5)/YbCoIn_5(5)$ determined by the resistivity.

to the superconducting transition up to 0.9 GPa. With pressure, T_N is gradually suppressed. At 1.6 GPa, the signature of the AFM transition is unclear in zero fields, and thus, the determination of T_N is ambiguous. However, with suppressing superconductivity by a magnetic field of 8 T applied perpendicular to the plane, we observe a peak in $d\rho/dT$ at ~ 2 K as shown in the inset of Fig. 5.7(b), indicating that the AFM transition is masked by the onset of superconducting transition. Since H_{c2} is very high at higher pressure, it is difficult to suppress the superconductivity, and hence, the precise estimation of the critical pressure, where the AFM transition vanishes, is difficult.

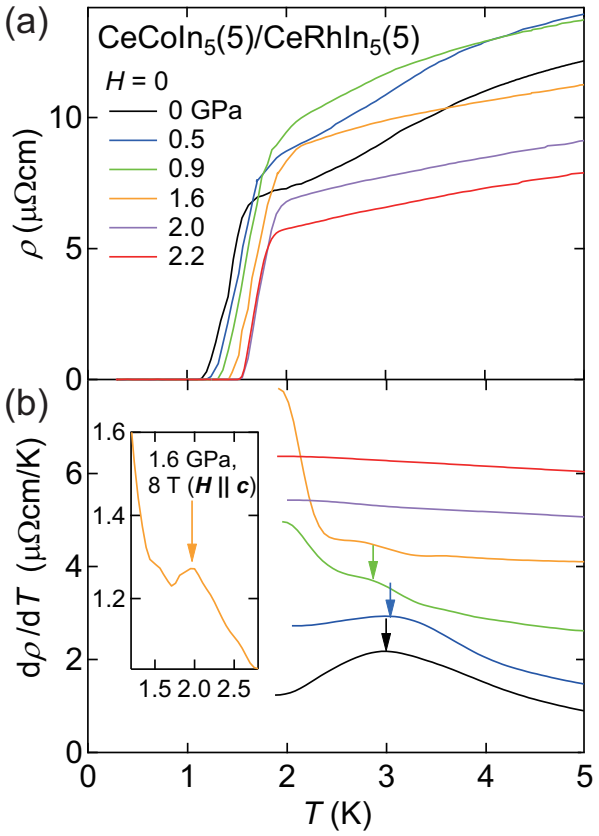

Figure 5.7: (a) Temperature dependence of the resistivity of $CeCoIn_5(5)/CeRhIn_5(5)$ superlattice under pressure. (b) Temperature derivative of the resistivity $d\rho/dT$. The inset shows $d\rho/dT$ at 1.6 GPa in perpendicular field of 8 T. The AFM transition temperature is determined by the peak of $d\rho/dT$.

In Fig. 5.8(a), we plot the p-dependence of T_c and T_N determined by the peak in $d\rho(T)/dT$. At $p \sim 2$ GPa, T_c is at a maximum, forming a dome-shaped p dependence. With pressure, T_N is suppressed gradually at low p, followed by a rapid suppression at $p \gtrsim 1$ GPa. At $p \gtrsim 1.6$ GPa, evidence for magnetic order is hidden beneath the superconducting dome. Although there is a large ambiguity in determining a critical pressure p_c, a simple extrapolation of $T_N(p)$ gives $p_c \sim 2$ GPa, where T_c is maximized. Further, this critical value is very close to that of p_c in $CeRhIn_5$ single crystals.

T_c and T_N of the hybrid superlattice are lower than that of the $CeCoIn_5$ and

$CeRhIn_5$ thin films, respectively, suggesting that they are influenced by dimensionality and electronic structures. However, they are still larger than that of respective $CeCoIn_5/YbCoIn_5$ and $CeRhIn_5/YbRhIn_5$ superlattices [76, 77], indicating the importance of mutual interaction between the $CeCoIn_5$ and $CeRhIn_5$ BLs.

5.3.5 Two-dimensional superconducting and magnetic states

We demonstrate that 2D superconductivity is realized in $CeCoIn_5$ BLs in the whole pressure regime. Figures 5.8(b) and 5.8(c) depict the T-dependence of the upper critical field determined by the midpoint of the resistive transition in a magnetic field H applied parallel ($H_{c2\parallel}$) and perpendicular ($H_{c2\perp}$) to the ab plane and the T-dependence of the anisotropy of upper critical fields, $H_{c2\parallel}/H_{c2\perp}$, respectively. The anisotropy diverges on approaching T_c, in sharp contrast to the $CeCoIn_5$ thin film whose anisotropy shows little T-dependence up to T_c. This diverging anisotropy in the superlattice is a characteristic feature of 2D superconductivity, in which $H_{c2\parallel}$ increases as $\sqrt{T_c - T}$ due to the Pauli paramagnetic limiting, but $H_{c2\perp}$ increases as $T_c - T$ due to orbital limiting near T_c. This result, along with the fact that the thickness of the $CeCoIn_5$-BL is comparable to the perpendicular superconducting coherence length $\xi_\perp \sim 3$–$4\,\mathrm{nm}$, indicates that each 5-UCT $CeCoIn_5$ BL effectively acts as a 2D superconductor [76]. The 2D superconductivity is reinforced by the angular variation of $H_{c2}(\theta)$. Figure 5.8(d) and its inset show $H_{c2}(\theta)$ below and above p^*. For both pressures, at temperature well below T_c, $H_{c2}(\theta)$ in the regime $|\theta| \lesssim 30^\circ$ is enhanced with decreasing $|\theta|$ and exhibits a sharp cusp at $\theta = 0$. This cusp behavior is typical for a Josephson coupled layered superconductor [31].

We note that in stark contrast to $CeRhIn_5$ single crystal and our thin film, each $CeRhIn_5$ BL in $CeCoIn_5(5)/CeRhIn_5(5)$ superlattice is not fully superconducting even when the AFM order is suppressed under pressure, which leads to the realization of 2D superconductivity in a wide range of pressure. In fact, as shown in Fig. 5.8(d), overall angle dependence of $H_{c2}(\theta)$ including the cusp structure near $\theta = 0$ is observed at $p = 1.8\,\mathrm{GPa}$, where the bulk superconductivity is not observed in $CeRhIn_5$ thin film (Fig. 5.4(b) and Fig. 5.5(b)). Essentially very similar angle dependence of $H_{c2}(\theta)$ is observed at $p = 2.1\,\mathrm{GPa}$ above p_c. These results imply that 2D superconductivity occurs in $CeCoIn_5$ BLs even above p_c. Moreover, in $CeRhIn_5(5)/YbRhIn_5(5)$ superlattice zero resistivity is not attained under pressure (Fig. 5.6(a) and (c)). With the reduction of BL thickness, the superconductivity of $CeRhIn_5$ is strongly suppressed, in stark contrast to $CeCoIn_5$. This may be related to the incommensurate magnetic structure of $CeRhIn_5$ with ordering vector $\boldsymbol{q} = (0.5, 0.5, 0.297)$ [62], in which the long-wavelength AFM fluctuations perpendicular to the layers are suppressed in $CeRhIn_5$ BLs with atomic layer thickness. In $CeCoIn_5$, on the other hand, AFM fluctuations with different $\boldsymbol{q} = (0.45, 0.45, 0.5)$ are dominant [144]. This commensurability along the c-axis would be better compatible with the superlattice structure, and as a result, the superconductivity is robust against the reduction of BL thickness [82].

Recent site-selective NMR measurements on a $CeCoIn_5(5)/CeRhIn_5(5)$ superlattice at ambient pressure report that the AFM order is not induced in $CeCoIn_5$ BLs [152]. As pressure suppresses the magnetic ordering in $CeRhIn_5$ and tunes $CeCoIn_5$ toward a

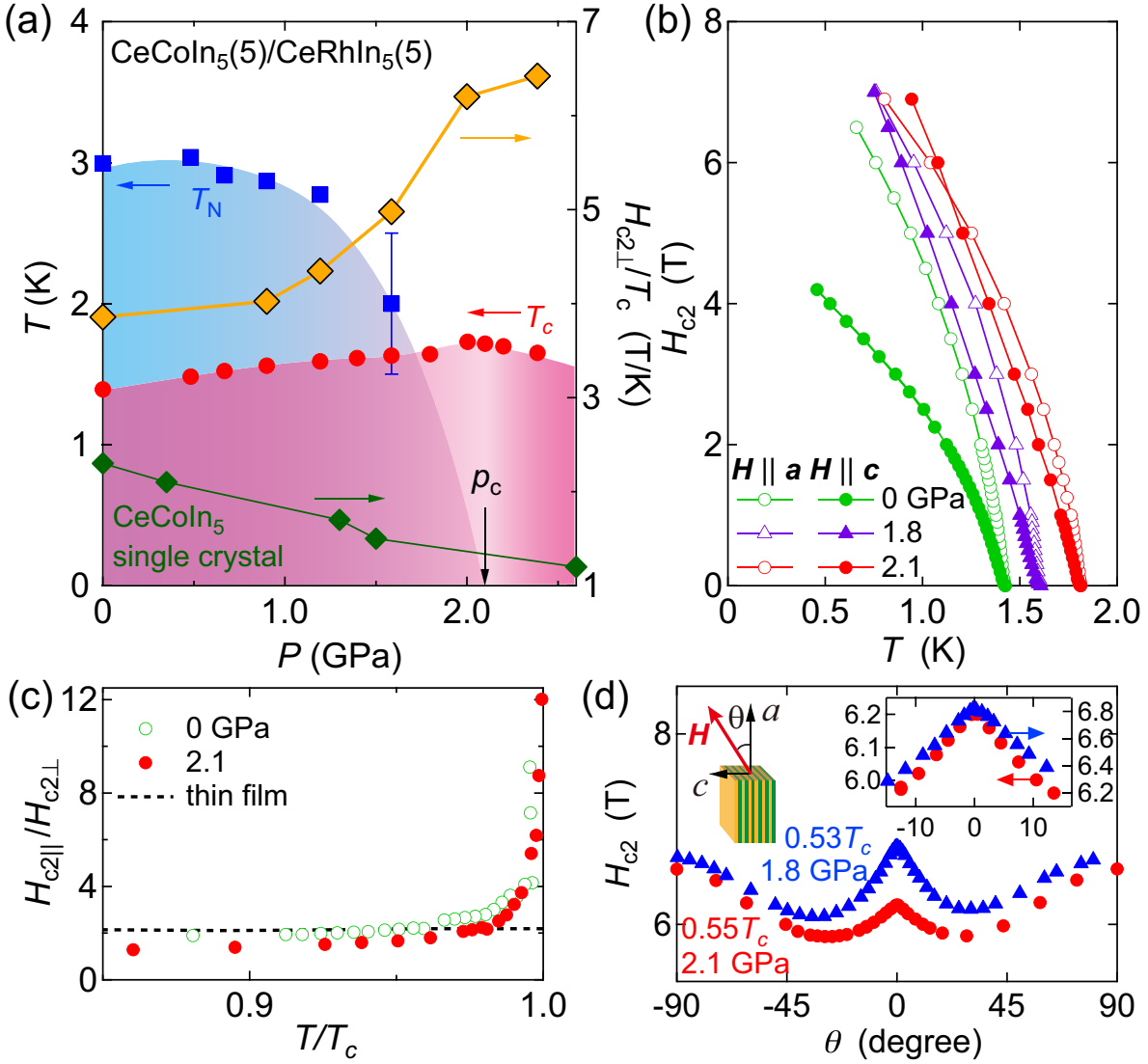

Figure 5.8: (a) p-T phase diagram of $CeCoIn_5(5)/CeRhIn_5(5)$ superlattice. Out-of-plane upper critical field $H_{c2\perp}$ normalized by T_c, $H_{c2\perp}/T_c$, measures the coupling strength of the superconductivity. (b) Temperature dependence of in-plane and out-of-plane upper critical fields at ambient pressure and at $p = 1.8$ and 2.1 GPa. (c) Anisotropy of upper critical field, $H_{c2\parallel}/H_{c2\perp}$, near T_c of superlattices at ambient pressure and at 2.1 GPa, along with the data of $CeCoIn_5$ thin film. (d) Angular dependence of upper critical field of superlattice at $p = 1.8$ and 2.1 GPa. (Inset) An expanded view of low angle region.

Fermi liquid state, it is unlikely that AFM order is induced in the $CeCoIn_5$ BLs under pressure.

We here comment on the low temperature anisotropy of H_{c2} of the $CeCoIn_5(5)/CeRhIn_5(5)$ superlattice (Fig. 5.8(b)). At $p = 2.1\,\mathrm{GPa}$, $H_{c2\perp}$ exceeds $H_{c2\parallel}$ at low temperatures. Such a reversed anisotropy of H_{c2} has been reported in $CeRhIn_5$ single crystal above the pressure where the AFM order disappears [59, 64]. However, similar reversed anisotropy ($H_{c2\perp} > H_{c2\parallel}$) is preserved at $p = 1.8\,\mathrm{GPa}$, where $H_{c2\parallel}$ exceeds $H_{c2\perp}$ in $CeRhIn_5$ single crystal and thin film. This indicates that anisotropy reversal of H_{c2} occurs under pressure in 5-UCT $CeCoIn_5$ BLs. Based on these results, we conclude that 2D superconducting $CeCoIn_5$ BLs in $CeCoIn_5(5)/CeRhIn_5(5)$ are coupled by the Josephson effect in the whole pressure regime.

5.3.6 Effect of local inversion symmetry breaking

Figure 5.9 displays $H_{c2\perp}(T)/H_{c2\perp}(0)$ of $CeCoIn_5(n)/CeRhIn_5(n)$ and $CeCoIn_5(n)/YbCoIn_5(5)$ superlattices plotted as a function of T/T_c. Here $H^{\mathrm{orb}}_{c2\perp}(0)$ is calculated by the initial slope of $H_{c2\perp}(T)$ at T_c by using Werthamer-Helfand-Hohenberg (WHH) formula, $H^{\mathrm{orb}}_{c2\perp}(0) = -0.69T_c(dH_{c2\perp}/dT)_{T_c}$. For comparison, we also include two extreme cases: $H_{c2\perp}/H^{orb}_{c2\perp}(0)$ for bulk $CeCoIn_5$ [119], in which H_{c2} is dominated by Pauli paramagnetism, and the WHH curve with no Pauli effect. In $CeCoIn_5(n)/YbCoIn_5(5)$, $H_{c2\perp}/H^{\mathrm{orb}}_{c2\perp}(0)$ increases with decreasing n. This is ascribed to the suppression of the Pauli pair-breaking effect at the interfaces, due to local ISB at the interface. With the reduction of n, the interface contribution increases, leading to the enhancement of the relative importance of the orbital pair-breaking effect compared to the Pauli pair-breaking effect. On the other hand, in $CeCoIn_5(n)/CeRhIn_5(n)$, $H_{c2\perp}/H^{\mathrm{orb}}_{c2\perp}$ is almost independent on n, indicating that the effect of local ISB is of little importance in $CeCoIn_5(n)/CeRhIn_5(n)$ superlattice.

5.3.7 Enhancement of superconducting pairing strength

The application of the pressure leads to a drastic change in the nature of superconductivity in the hybrid superlattices. Figure 5.10(a) depicts the T-dependence of $H_{c2\perp}/H^{\mathrm{orb}}_{c2\perp}(0)$ of $CeCoIn_5(5)/CeRhIn_5(5)$ for several pressures. What is remarkable is that near the critical pressure $p_c \sim 2\,\mathrm{GPa}$ at which evidence for magnetic order disappears, $H_{c2\perp}/H^{\mathrm{orb}}_{c2\perp}$ nearly coincides with the WHH curve, indicating that $H_{c2\perp}$ is limited solely by orbital pair-breaking.

The fact that $H_{c2\perp}$ approaches the orbital limit provides important insight on superconductivity of the hybrid superlattice. In $CeCoIn_5/YbCoIn_5$, where $YbCoIn_5$ is a conventional metal, Pauli pair-breaking effect is weakened in the superlattice compared with the bulk due to local ISB at the interfaces, which splits the Fermi surfaces with spin texture and thus effectively suppresses the Zeeman effect [80, 81]. This leads to the Rashba-induced anisotropic suppression of the Zeeman effect [79], which may be partly responsible for the observed reversed anisotropy $H_{c2\parallel}/H_{c2\perp} < 1$ at low temperatures (Fig. 5.8(d)). However, this effect is less important in $CeCoIn_5(n)/CeRhIn_5(n)$

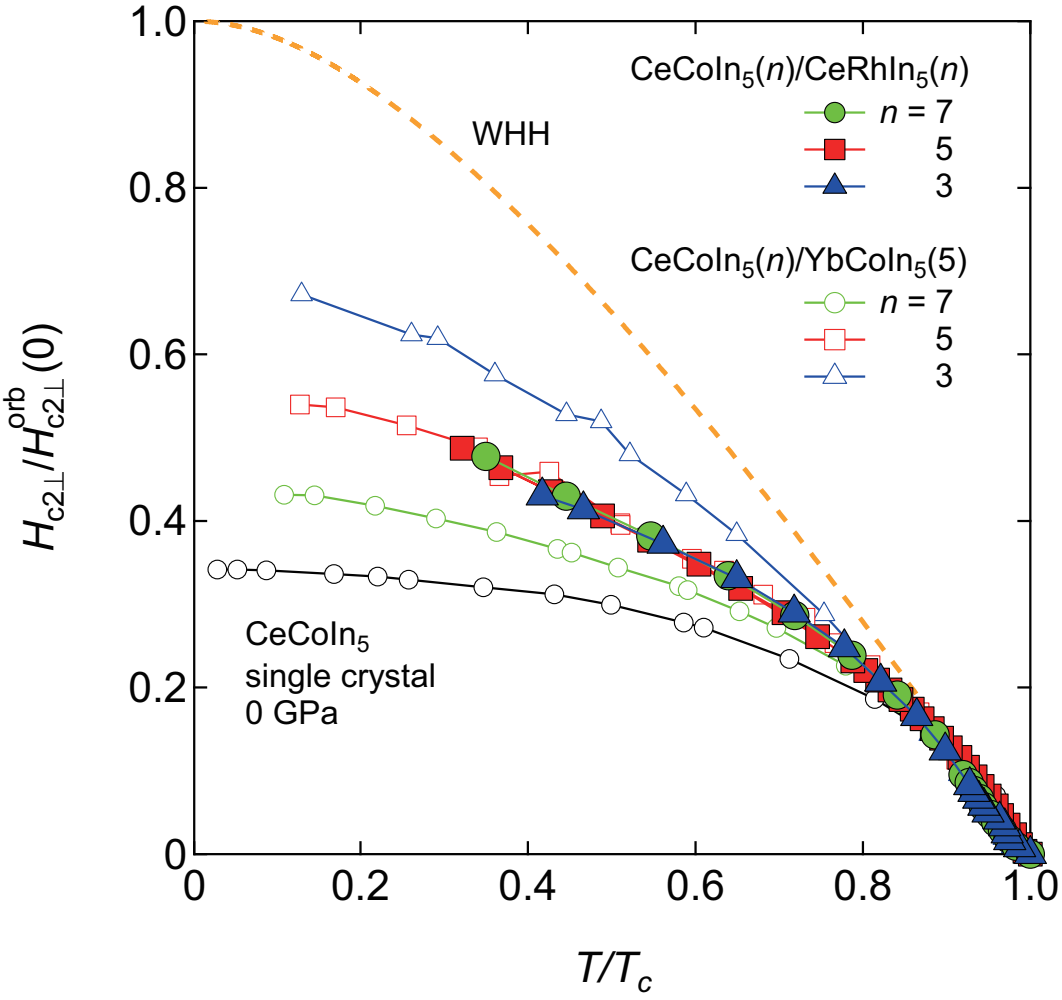

Figure 5.9: Out-of-plane upper critical field $H_{c2\perp}$ normalized by the orbital-limited upper critical field at $T = 0\,\mathrm{K}$, $H_{c2\perp}/H_{c2\perp}^{orb}(0)$, for $CeCoIn_5(n)/CeRhIn_5(n)$ and $CeCoIn_5(n)/YbCoIn_5(5)$ superlattices with $n = 7$, 5, and 3 are plotted as a function of the normalized temperature T/T_c. Two extreme cases, i.e., the result of the bulk $CeCoIn_5$ dominated by Pauli paramagnetic effect and the WHH curve with no Pauli effect, are also shown. The effect of local ISB is of little important in $CeCoIn_5(n)/CeRhIn_5(n)$.

superlattices compared with $CeCoIn_5/YbCoIn_5$, which is evidenced by the fact that $H_{c2\perp}/H_{c2\perp}^{\rm orb}(0)$ does not strongly depend on n (Fig. 5.9). Moreover, such an effect is not expected to have significant pressure dependence. Therefore, there must be a different mechanism that significantly enhances the Pauli-limiting field $H_{c2\perp}^{\rm Pauli} = \sqrt{2}\Delta/g\mu_{\rm B}$, where g is the g-factor of electrons and $\mu_{\rm B}$ is the Bohr magneton. An enhancement of $H_{c2\perp}^{\rm Pauli}$ is not due to a dramatic suppression of g by pressure, because it is highly unlikely that the Ce crystalline electric field state, which determines g-factor, strongly depends on pressure. Therefore the enhancement of $H_{c2\perp}^{\rm Pauli}$ is attributed to a strong increase in the superconducting gap Δ. This is supported by the observed enhancement of $H_{c2\perp}/T_c$ upon approaching p_c shown in Fig. 5.8(a). Because $H_{c2\perp} \approx H_{c2\perp}^{\rm Pauli} \ll H_{c2\perp}^{\rm orb}(0)$ in the low p regime and $H_{c2\perp} \approx H_{c2\perp}^{\rm orb}(0) \ll H_{c2\perp}^{\rm Pauli}$ near $p \sim p_c$, the enhancement of $H_{c2\perp}/k_{\rm B}T_c$ directly indicates an enhancement of $H_{c2\perp}^{\rm Pauli}/T_c$ and hence $\Delta/k_{\rm B}T_c$. This behavior contrasts with observations on $CeCoIn_5$ single crystals, in which H_{c2}/T_c decreases with pressure. The enhancement of $\Delta/k_{\rm B}T_c$ is caused as a consequence of the enhancement of pairing interaction. In the spin fluctuation mediated scenario, the pairing interaction is mainly provided by high energy spin fluctuations whose energy scale is well above Δ and low energy fluctuations cause the pair-breaking. Since the high energy fluctuations enhance T_c while low energy ones reduce T_c, the enhancement of pairing interaction can give rise to the increase of $\Delta/k_{\rm B}T_c$ without accompanying a large enhancement of T_c, which is consistent with the observed behavior. Thus, the present results demonstrate that the pairing interaction in $CeCoIn_5$ BLs is strikingly enhanced as a result of the quantum critical magnetic fluctuations that develop in $CeRhIn_5$ BLs, which are injected into $CeCoIn_5$ BLs through the interface.

It is well established that quantum fluctuations strongly influence normal and superconducting properties in many classes of unconventional superconductors. One of the most striking is a diverging effective quasiparticle mass m^* upon approaching the QCP, as reported in cuprate, pnictide and heavy-fermion systems [2, 36, 145]. Such a mass enhancement gives rise to a corresponding enhancement of $H_{c2}^{\rm orb}$, which is proportional to $(m^*\Delta)^2$. Here we stress that there is a fundamental difference in the present hybrid superlattices. Figure 5.10(b) depicts the p-dependence of $H_{c2\perp}^{\rm orb}$ of the $CeCoIn_5(n)/CeRhIn_5(n)$ superlattices with $n = 4$ and 5, along with the result for $CeCoIn_5$ and $CeRhIn_5$ single crystals [64, 142]. In contrast to a $CeRhIn_5$ single crystal which shows a sharp peak at the critical pressure, $H_{c2\perp}^{\rm orb}$ of the superlattices depends weakly on pressure with no significant anomaly at p_c. Compared to the monotonic decrease observed in single crystal $CeCoIn_5$, this weak dependence is consistent with an enlarged gap Δ, but the results suggest the absence of mass enhancement in the $CeCoIn_5$ BL. Such behavior is in contrast to usual expectations for quantum criticality, details of which deserve further studies.

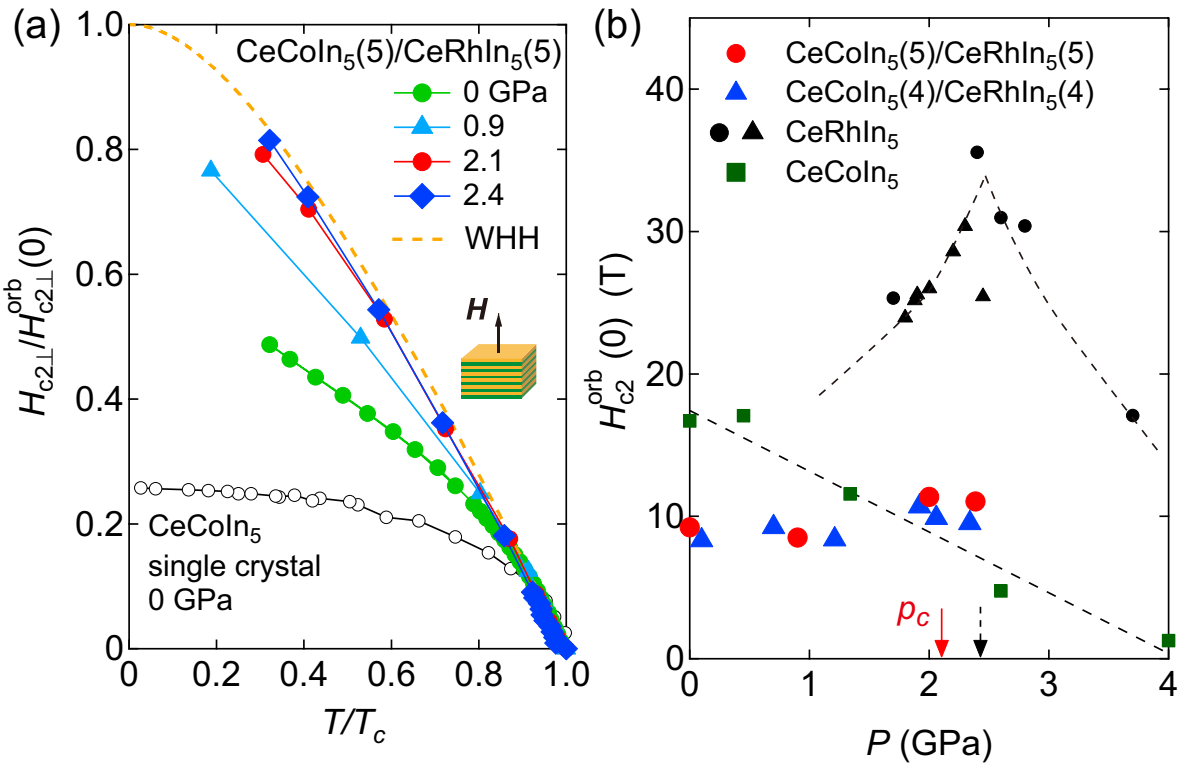

Figure 5.10: (a) Out-of-plane upper critical field $H_{c2\perp}$ normalized by the orbital-limited upper critical field at $T = 0\,\mathrm{K}$, $H_{c2\perp}/H_{c2\perp}^{\mathrm{orb}}(0)$, for $CeCoIn_5(5)/CeRhIn_5(5)$ superlattice is plotted as a function of the normalized temperature T/T_c. Two extreme cases, i.e., the result of the bulk $CeCoIn_5$ dominated by Pauli paramagnetic effect and the WHH curve with no Pauli effect, are also shown. (b) Pressure dependence of $H_{c2}^{\mathrm{orb}}(0)$ of $CeCoIn_5(n)/CeRhIn_5(n)$ superlattices with $n = 4$ and 5 for $\boldsymbol{H}\|c$. For comparison, $H_{c2}^{\mathrm{orb}}(0)$ of $CeRhIn_5$ single crystals for $\boldsymbol{H}\|a$ and that of $CeCoIn_5$ single crystal for $\boldsymbol{H}\|c$ are shown. Solid and dashed arrows represent p_c for $CeCoIn_5(n)/CeRhIn_5(n)$ superlattices and $CeRhIn_5$ single crystal, respectively.

5.4 Summary

In summary, we have designed and fabricated the hybrid superlattice $CeCoIn_5/CeRhIn_5$ formed by alternating atomically thick layers of a d-wave heavy-fermion superconductor $CeCoIn_5$ and an AFM metal $CeRhIn_5$. The present results demonstrate the importance of the interface between which unconventional superconducting and non-superconducting magnetic layers can interact with each other. In particular, the strength of the pairing interaction can be tuned by magnetic fluctuations, or paramagnons, injected through the interface, highlighting that the pairing interaction can be maximized by the critical fluctuations emanating from the magnetic QCP without an accompanying mass enhancement. The fabrication of a wide variety of hybrid superlattices paves a new way to study the entangled relationship between unconventional superconductivity and magnetism, offering a route to exploring the emergence of novel superconducting systems and the roles of their interface.

Chapter 6

Coupling between d-wave superconductivity and antiferromagnetism in $CeCoIn_5/CeIn_3$ hybrid superlattices

6.1 Introduction

In Chapter 5, we have studied that in superlattices consisting of alternating layers of $CeCoIn_5$ and the antiferromagnetic (AFM) metal $CeRhIn_5$ [Fig. 6.1(a)], the superconducting and AFM state coexist in spatially separated layers. In these hybrid superlattices, the influence of local inversion symmetry breaking at the interface has been shown to be less critical compared to $CeCoIn_5/YbCoIn_5$. In sharp contrast to $CeCoIn_5/YbCoIn_5$, NMR measurements have revealed that magnetic fluctuations in $CeCoIn_5$ BLs of $CeCoIn_5/CeRhIn_5$ superlattices are enhanced compared to bulk $CeCoIn_5$ single crystal, highlighting the importance of the magnetic proximity effect [152]. In particular, it has been pointed out that in the vicinity of the QCP of $CeRhIn_5$ block layers (BLs), AFM fluctuations are enhanced, and the force binding superconducting electron-pairs acquires an extremely strong-coupling nature. This indicates that superconducting pairing can be manipulated by magnetic fluctuations injected through the interface [90].

To obtain further insight into the mutual interactions between unconventional superconductivity and magnetic order, we here fabricate superlattices consisting of alternating layers of $CeCoIn_5$ and the AFM metal $CeIn_3$ [Fig. 6.1(b)]. $CeIn_3$ is an isotropic Kondo lattice material with a cubic crystal structure. In bulk $CeIn_3$ single crystals, AFM order with the ordered magnetic moment of $0.48\,\mu_B$ occurs with a commensurate wave vector $\boldsymbol{q} = (0.5, 0.5, 0.5)$ at $T_N = 10\,\mathrm{K}$, where μ_B is the Bohr magneton [69]. With applying pressure, T_N decreases and vanishes at $\sim 2.6\,\mathrm{GPa}$, indicating an AFM QCP. Superconductivity with a maximum $T_c \approx 200\,\mathrm{mK}$ is induced in a very narrow pressure range around the QCP [1, 70].

In this section, we will design and fabricate the hybrid superlattices of

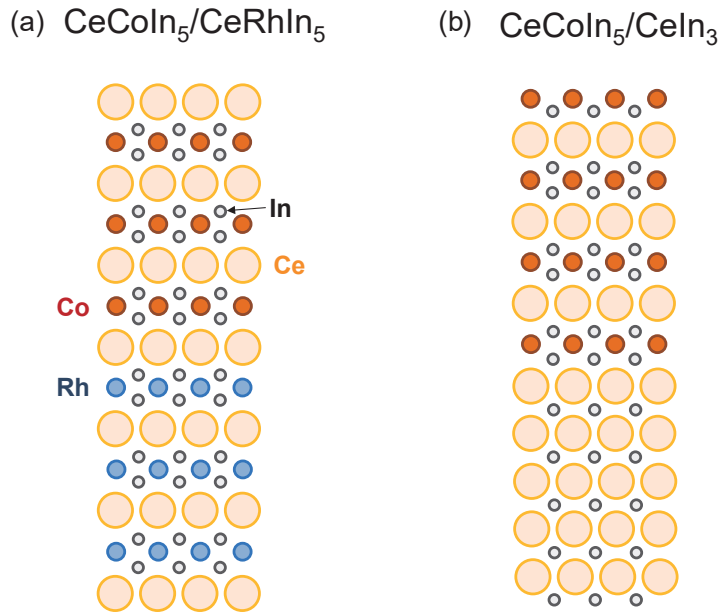

Figure 6.1: Schematic representations of three types of heavy-fermion superlattices, (a) $CeCoIn_5/CeRhIn_5$, and (b) $CeCoIn_5/CeIn_3$, where $CeCoIn_5$ is a heavy-fermion d-wave superconductor, and $CeRhIn_5$ and $CeIn_3$ are heavy-fermion AFM metals. The atomic views of the (1 0 0) plane are shown.

$CeCoIn_5/CeIn_3$ and confirm the superlattice structures using the same methods we used in previous sections. We will show the transport measurements at ambient pressure and under high pressure where AFM order in $CeIn_3$ layers expected to be suppressed. We will see the dimensionality of superconductivity and magnetism. Then, we will discuss the effect of magnetic fluctuations in $CeIn_3$ BLs on d-wave superconductivity. Finally, we end with a summary and our conclusions.

6.2 Experimental details

The hybrid superlattices $CeCoIn_5(7)/CeIn_3(n)$ (n = 3, 4, 6 and 13) with c axis oriented structure are grown on a MgF_2 substrate by MBE technique. We first grow $\sim$ 20 unit-cell-thick (UCT) $CeIn_3$ ($\sim$ 10 nm) as a buffer layer on MgF_2. Then 7-UCT $CeCoIn_5$ and n-UCT $CeIn_3$ (n = 3, 4, 6 and 13) are grown alternatively with total thicknesses of approximately 200 nm. As the epitaxial growth temperature of $CeCoIn_5$ and $CeIn_3$ layers are different, $CeCoIn_5$ and $CeIn_3$ BLs were grown at 570 and 420 °C, respectively. The superlattice is capped with $\sim$ 5 nm Co to prevent oxidation. The deposition rate was monitored by a crystal rate monitor. The typical growth rate was 0.1–0.2Å/s.

Using a piston-cylinder cell with Daphne oil 7373 as the pressure transmitting medium, we performed high-pressure resistivity measurements under hydrostatic pressure up to 2.4 GPa. The pressure inside the cell was determined by the superconducting transition temperature of Pb, measured by quasi-four wire resistivity. Electrical in-plane

resistivity was measured with a standard four-probe method with LR-700 ac resistance bridge in a hand-made ^{4}He pumping probe for 1.6–300 K at zero magnetic fields and ^{3}He-cryostat (Heliox VL) system for 0.3–300 K.

6.3 Results

6.3.1 Characterization

We fabricated hybrid superlattices with alternating block layers (BLs) of n-UCT $CeCoIn_5$ and m-UCT $CeRhIn_5$, $CeCoIn_5(n)/YbCoIn_5(m)$ with $n = m = 7$, 5, 3. In this section, we focus on the characterization of these superlattices. The superlattice structures were confirmed by transmission electron microscopy (TEM) and electron energy loss spectroscopy (EELS), X-ray diffraction (XRD), and reflection high-energy electron diffraction (RHEED). The details are given in the following sections.

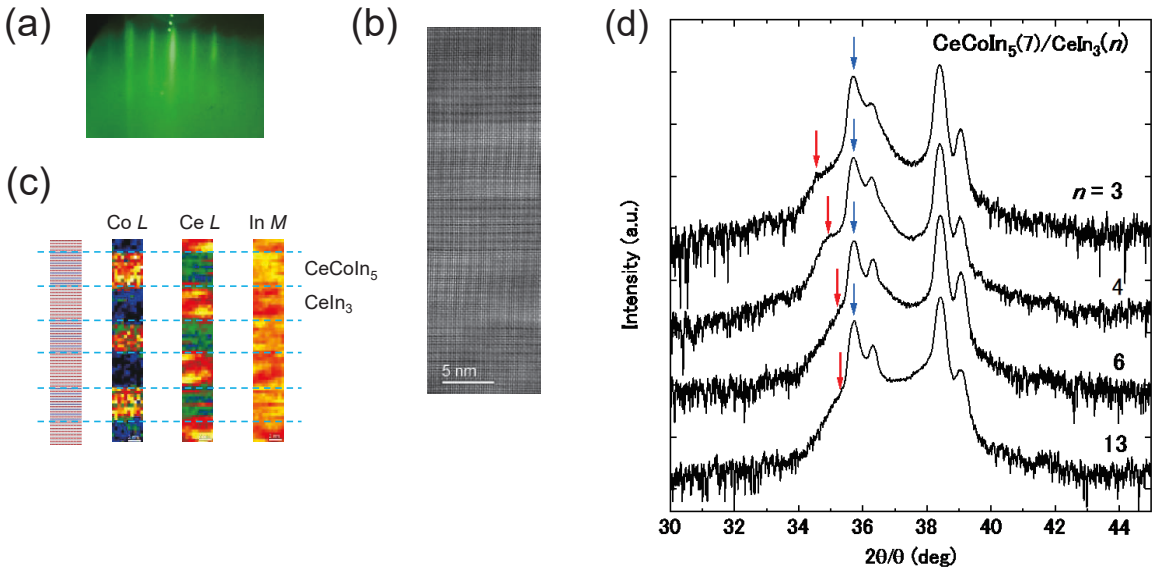

Figure 6.2: (a) Typical RHEED streak patterns for $CeCoIn_5(7)/CoIn_3(13)$ superlattice taken during the crystal growth. (b), (c) High-resolution cross-sectional (b) TEM image and (c) EELS images for the $CeCoIn_5(7)/CoIn_3(13)$ superlattice with the electron beam alined along the (100) direction. The EELS images were taken for Co L, Ce L, and In M edges. (d) Cu $K\alpha_1$ x-ray diffraction patterns for $CeCoIn_5(7)/CoIn_3(n)$ superlattices ($n = 3$, 4, 6, and 13). The blue and red arrows indicate the (0 0 3) peaks of $CeCoIn_5$ and satellite peaks due to the superlattice structure, respectively.

TEM and EELS

Figure 6.2(b) displays a high-resolution cross-sectional TEM image along the (1 0 0) direction for the $CeCoIn_5(7)/CeIn_3(13)$ superlattice. A clear interface between the $CeCoIn_5$ and the $CeIn_3$ layers is observed. 6.2(c) displays an EELS image of the same

superlattice. The EELS images clearly resolve the 7-UCT $CeCoIn_5$ and the 13-UCT $CeIn_3$ BLs, demonstrating sharp interfaces with no atomic interdiffusion between the neighboring $CeCoIn_5$ and $CeIn_3$ BLs.

XRD

Figure 6.2(d) shows the X-ray diffraction patterns for $CeCoIn_5(7)/CeIn_3(n)$ superlattices. The shoulder structure shown by the red arrows near the (0 0 3) peak of $CeCoIn_5$ (blue arrows) is consistent with the superlattice structure. The obtained c-axis lattice constants of $CeCoIn_5$ BLs is 7.532 Å, which well coincides with that in $CeCoIn_5/CeRhIn_5$ (7.536 Å).

RHEED

Figure 6.2(a) shows RHEED image of $CeCoIn_5(7)/CeIn_3(13)$. A clear streak pattern has been observed during the growth, demonstrating the epitaxial growth of each layer with an atomically flat surface. Similar RHEED patterns were also observed for other superlattices, regardless of the thickness modulation of $CeCoIn_5$ BLs and $CeIn_5$ BLs.

6.3.2 Transport measurements

Figure 6.3(a) depicts the temperature dependence of the resistivity ρ of $CeCoIn_5(7)/CeIn(n)$ superlattices with $n = 3$, 4, 6 and 13. We also show ρ of $CeCoIn_5$ and $CeIn_3$ thin films grown by MBE. The mean free path of these superlattices is difficult to estimate because of the parallel conductions of $CeCoIn_5$ and $CeIn_3$ BLs. However, the mean free path in each BL is expected to be shorter than the atomically flat regions extending over distances of ~ 0.1 μm, because of the following reasons. In $CeCoIn_5$ and $CeIn_3$ single crystals, the mean free path determined by the de Haas-van Alphen oscillations is $\sim 0.2\mu$m [153, 154]. The residual resistivity ratio of $CeCoIn_5$ and $CeIn_3$ thin films with 100 nm thickness is 4–5 times smaller than that of the single crystals. Therefore, the mean free path of $CeCoIn_5$ and $CeIn_3$ BLs in the superlattices is expected to be much shorter than 0.1 μm, suggesting that the transport properties are not seriously influenced by the surface roughness. The resistivity of $CeCoIn_5(7)/CeIn(n)$ superlattices follows the typical heavy-fermion behavior. With decreasing temperature, $\rho(T)$ increases below ~ 150 K due to the Kondo scattering but then begins to decrease due strong c-f hybridization between f-electrons and conduction (c) band electrons, leading to the narrow f-electron band at the Fermi level. The Kondo coherence temperature T_{coh}, at which the formation of heavy-fermion occurs, is estimated from the maximum in $\rho(T)$. As shown in 6.3(a), T_{coh} of $CeCoIn_5(7)/CeIn(n)$ superlattices is nearly independent of n and is closer to T_{coh} of $CeCoIn_5$ thin film than T_{coh} of $CeIn_3$ thin film, suggesting that T_{coh} is mainly determined by $CeCoIn_5$ BLs. 6.3(b)-(f) depict $\rho(T)$ at low temperatures. All superlattices show the superconducting transition at $T \approx 1.5$ K. For the $n = 3$- and 4-superlattices, $\rho(T)$ decreases with increasing slope, $d\rho(T)/dT$, as the temperature is lowered below 12 K down to T_c.

The lattice parameters along the a-axis of $CeCoIn_5$, $CeRhIn_5$, and $CeIn_3$ is 4.613, 4.653, and 4.69 Å, respectively. Therefore, large tensile strain along the a-axis is

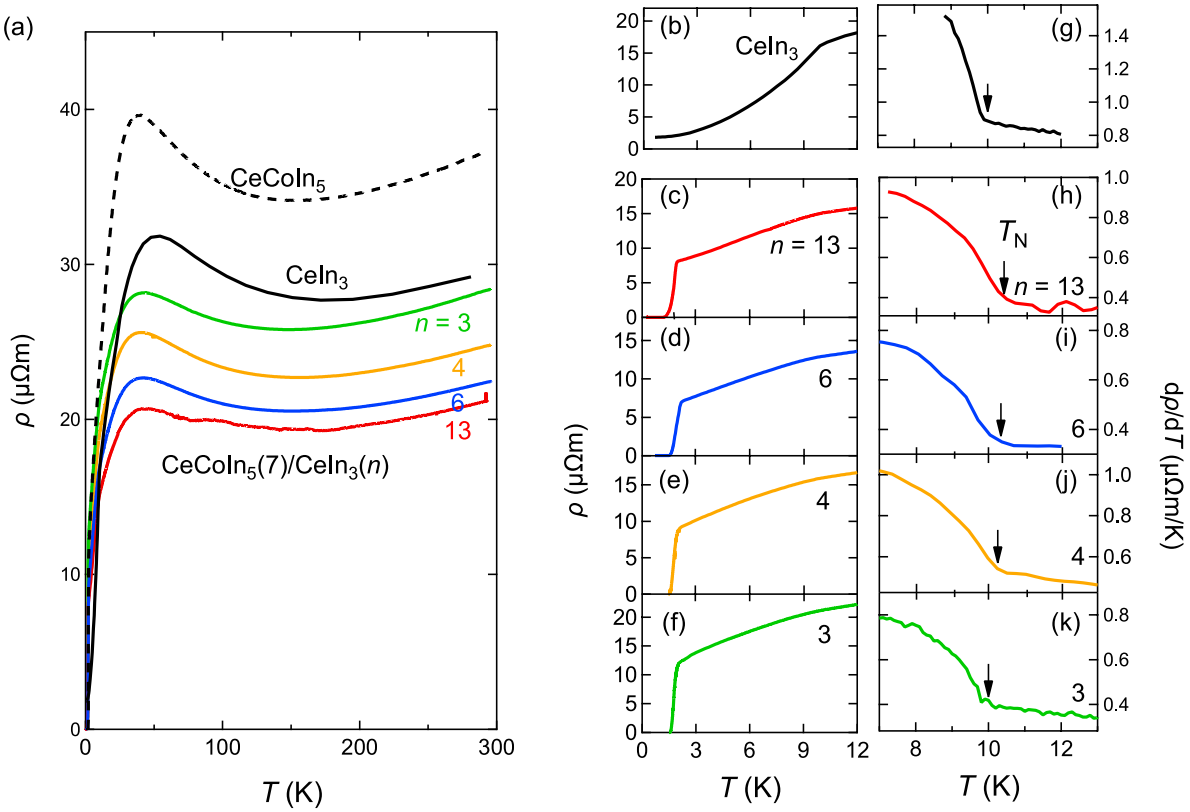

Figure 6.3: (a) Temperature dependence of the resistivity $\rho(T)$ in $CeCoIn_5(7)/CeIn_3(n)$ superlattices for $n = 3$, 4, 6, and 13, along with $\rho(T)$ for $CeIn_3$ (black solid line) and $CeCoIn_5$ (black dashed line) thin films. Inset illustrates the schematics of $CeCoIn_5(7)/CeIn_3(n)$ superlattice. (b)-(f) $\rho(T)$ at low temperatures. (g)-(f) Temperature derivative of the resistivity, $d\rho(T)/dT$, as a function of temperature. The arrows indicate the Néel temperature T_N.

expected in $CeCoIn_5$ BLs of $CeCoIn_5/CeIn_3$ compared to $CeCoIn_5/CeRhIn_5$. It has been shown that the uniaxial pressure dependence of T_c along the a-axis for $CeCoIn_5$ is $dT_c/dp_a = 290$ mK/GPa ([155]), indicating that T_c decreases by tensile strain. However, T_c of $CeCoIn_5/CeIn_3$ ($T_c \sim 1.5$ K) is larger than that of $CeCoIn_5/CeRhIn_5$ ($T_c \sim 1.4$ K). We note that the lattice parameter along the c-axis for $CeCoIn_5$ BLs in $CeCoIn_5/CeIn_3$, which is estimated from x-ray diffraction, well coincides with that in $CeCoIn_5/CeRhIn_5$. These results suggest that the strain effect at the interfaces is not important for determining T_c. 6.3(g)–(k) display the temperature derivative of the resistivity $d\rho(T)/dT$. As shown by the arrows in 6.3(g), $d\rho(T)/dT$ of $CeIn_3$ thin film exhibits a distinct kink at $T_N = 10$ K [69]. Similar kink structures are observed in all superlattices at the temperatures indicated by arrows, showing the AFM transition.

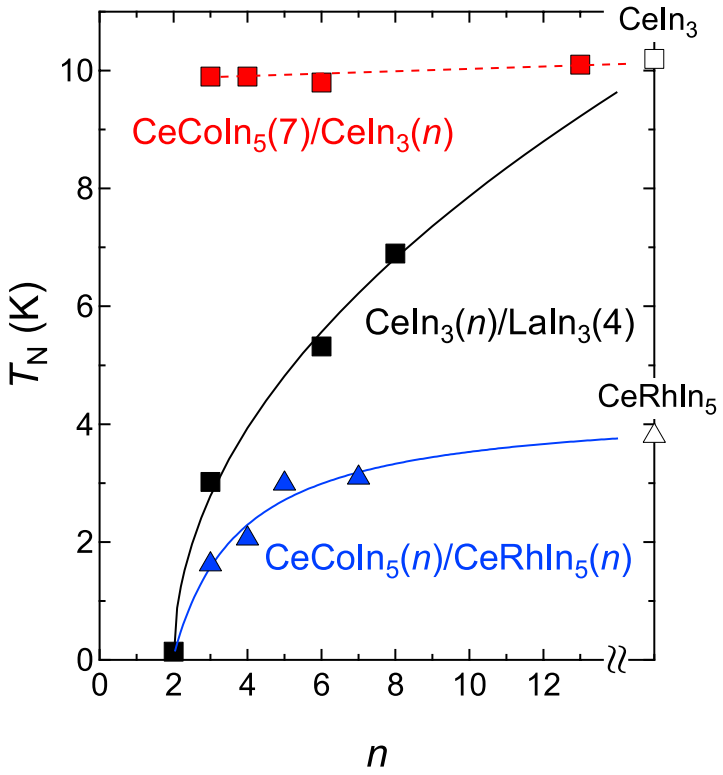

Figure 6.4: The Néel temperature T_N for $CeCoIn_5(7)/CeIn_3(n)$ as a function of n. For comparison, T_N for $CeIn_3(n)/LaIn_3(4)$ and $CeCoIn_5(n)/CeRhIn_5(n)$ are shown. Open square and triangle are T_N of bulk $CeIn_3$ and $CeRhIn_5$ single crystals, respectively.

Figure 6.4 shows the thickness dependence of T_N of the $CeCoIn_5(7)/CeIn_3(n)$ superlattices. For comparison, the data sets of $CeIn_3(4)/LaIn_3(n)$, where $LaIn_3$ is a nonmagnetic conventional metal with no f-electrons [75], and $CeCoIn_5(n)/CeRhIn_5(n)$ are also included in the figure. Remarkably, the observed thickness dependence of T_N in $CeCoIn_5/CeIn_3$ is in striking contrast to that in $CeIn_3/LaIn_3$; While T_N is strongly suppressed with decreasing n and vanishes at $n = 2$ in $CeIn_3/LaIn_3$, T_N is nearly independent of n in $CeCoIn_5(7)/CeIn_3(n)$. This suggests that $CeIn_3$ BLs are coupled weakly by the RKKY interactions through the adjacent $LaIn_3$ BL, but they can

strongly couple through the adjacent $CeCoIn_5$ BL. This is even more surprising, as the distance between different $CeIn_3$ BLs is larger in the $CeCoIn_5(7)/CeIn_3(n)$ superlattices than in the $CeIn_3(n)/LaIn_3(4)$ superlattices. We thus conclude that small but finite magnetic moments are induced in $CeCoIn_5$ BLs in $CeCoIn_5/CeIn_3$, which mediate the RKKY-interaction. On the other hand, because of the absence of strongly interacting f-electrons in $LaIn_3$, which can form magnetic moments, the RKKY interaction in $CeIn_3/LaIn_3$ can be expected to be much weaker. To clarify this, a microscopic probe of magnetism, such as NMR measurements, is required. We note that as shown in 6.4, the reduction of T_N is also observed in $CeCoIn_5(n)/CeRhIn_5(n)$ superlattices [90], suggesting that the RKKY interaction between $CeRhIn_5$ BLs through adjacent $CeCoIn_5$ BL is negligibly small. This is supported by the recent site-selective NMR measurements which report no discernible magnetic moments induced in the $CeCoIn_5$ BLs while magnetic fluctuations are injected from $CeRhIn_5$ BLs into one or two layers of $CeCoIn_5$ BLs in $CeCoIn_5/CeRhIn_5$ [152].

The pressure dependence of the superconducting and magnetic properties provide crucial information on the mutual interaction between superconductivity and magnetism through the interface. 6.5(a) and (b) and their insets show the temperature dependence of $\rho(T)$ under pressure for $CeCoIn_5(7)/CeIn_3(n)$ for $n = 13$ and 6, respectively. With the application of pressure, the temperature at which $\rho(T)$ shows its maximum increases due to the enhancement of the c-f hybridization [143]. This is caused by the enhancement of bandwidth of the conduction electron. As shown in the insets, both superlattices undergo a superconducting transition under pressure. 6.5(c)-(e) and (f)-(h) show $d\rho(T)/dT$ under pressure for $n = 13$ and 6, respectively. Clear kink structure associated with the AFM transition can be seen in the data.

Figure 6.6(a) depicts the pressure dependence of T_N and T_c for $CeCoIn_5(7)/CeIn_3(n)$ superlattices for $n = 6$ and 13. With applying pressure, T_N decreases rapidly. For comparison, T_N of a single crystal $CeIn_3$ is also shown by the solid line [1]. The pressure dependence of T_N of both superlattices is very similar to that of the bulk $CeIn_3$ single crystal. In bulk $CeIn_3$ crystal, the AFM QCP is located at $p_c \approx 2.6\,\mathrm{GPa}$. It is natural to expect, therefore, that the AFM QCP of the superlattices is close to 2.6 GPa. Thus, at 2.4 GPa, the superlattices are in the vicinity of the AFM QCP. This is supported by the temperature dependence of the resistivity under pressure. The resistivity can be fitted as

$$\rho(T) = \rho_0 + AT^{\varepsilon}. \tag{6.1}$$

Figure 6.6(b) shows the pressure dependence of ε obtained from $d\ln\Delta\rho/d\ln T$, where $\Delta\rho = \rho(T) - \rho_0$. The magnitude of ε decreases with pressure. In bulk $CeIn_3$ single crystal, ε decreases with pressure and exhibits a minimum at the AFM QCP [1, 70]. On the other hand, applying pressure to $CeCoIn_5$ leads to an increase of ε, which is attributed to the suppression of the non-Fermi liquid behavior, $\rho(T) \propto T$, and the development of a Fermi liquid state with its characteristic $\rho(T) \propto T^2$ dependence [37, 143]. Therefore, the reduction of ε with pressure arises from the $CeIn_3$ BLs, indicating that the $CeIn_3$ BLs approach the AFM QCP.

As shown in 6.6(a), T_c increases, peaks at $\sim 1.8\,\mathrm{GPa}$, and then decreases when applying pressure. This pressure dependence bears a resemblance to that of $CeCoIn_5$ bulk

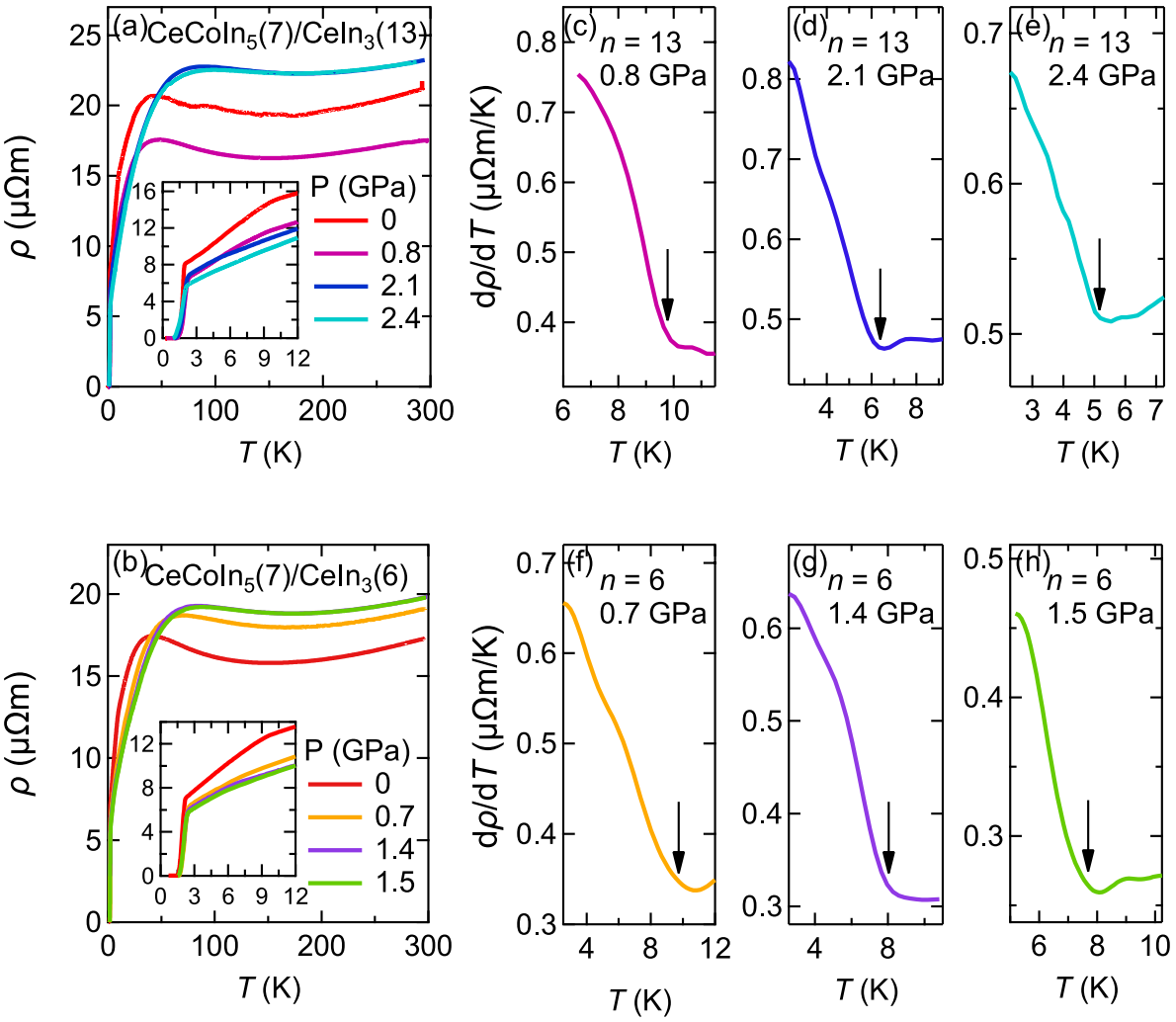

Figure 6.5: (a), (e) Temperature dependence of the resistivity $\rho(T)$ under pressure for $CeCoIn_5(7)/CeIn_3(n)$ for (a) $n = 13$ and (e) $n = 6$. Inset: $\rho(T)$ at low temperatures. (b)–(d) and (f)–(h) show the temperature derivative of the resistivity, $d\rho(T)/dT$, as a function of temperature under pressure for $n = 13$ and $n = 6$, respectively. The arrows indicate the Néel temperature T_N.

single crystals [37]. An analysis of the upper critical field provides important information about the superconductivity of $CeCoIn_5$ BLs. Figure 6.7 depicts the temperature dependence of the upper critical field determined by the midpoint of the resistive transition in a magnetic field $\boldsymbol{H}$ applied parallel ($H_{c2\parallel}$) and perpendicular ($H_{c2\perp}$) to the layers. The inset of Fig. 6.7 shows the anisotropy of the upper critical fields $H_{c2\parallel}/H_{c2\perp}$ at ambient pressure. The anisotropy diverges on approaching T_c. This is in sharp contrast to the $CeCoIn_5$ thin film, whose anisotropy is nearly temperature independent up to T_c. The observed diverging anisotropy indicates that the superconducting electrons are confined in the 2D $CeCoIn_5$ BLs. In fact, in 2D superconductivity, $H_{c2\parallel}$ is limited by Pauli paramagnetic pair breaking and increases as $\sqrt{T_c - T}$, while $H_{c2\perp}$ increases as $T_c - T$ due to the orbital pair breaking near T_c [76]. Moreover, the thickness of the $CeCoIn_5$ BL is comparable to the coherence length perpendicular to the layer, $\xi_c \sim 4\,\mathrm{nm}$. Thus each 7-UCT $CeCoIn_5$ BL effectively behaves as a 2D superconductor.

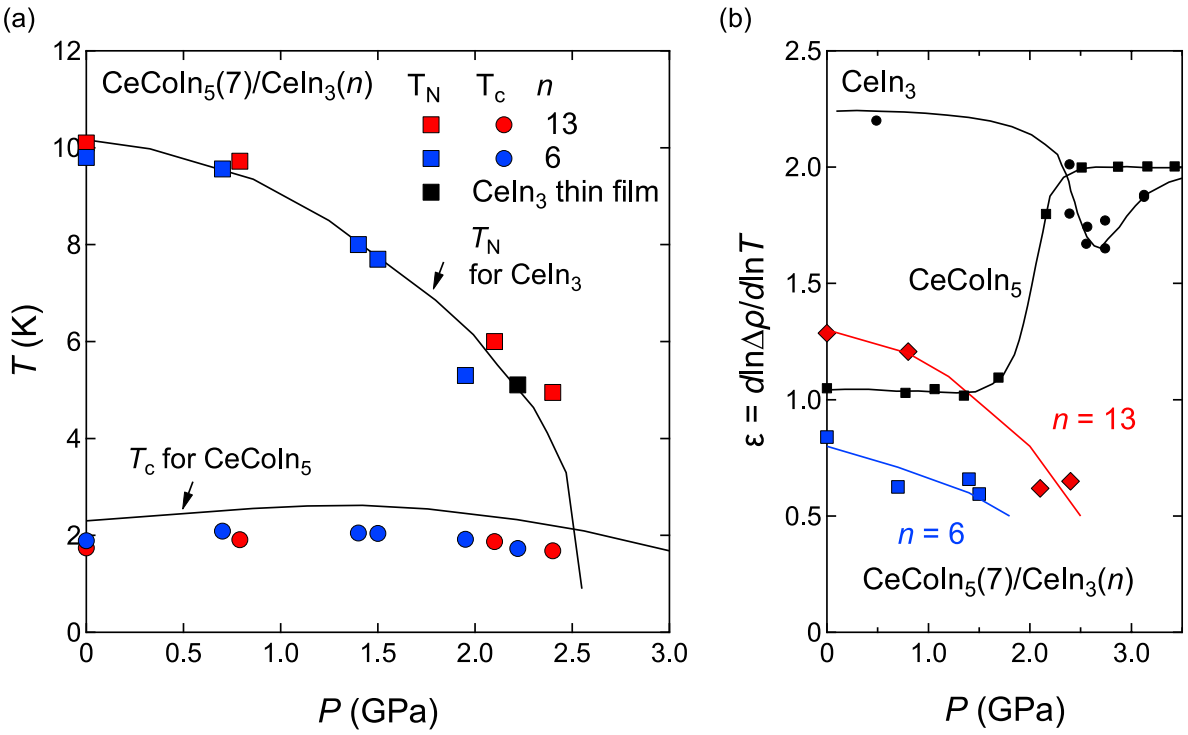

Figure 6.6: (a) Pressure dependence of T_N and T_c of $CeCoIn_5(7)/CeIn_3(n)$ superlattices for $n = 13$ and 6. For comparison, T_N of $CeIn_3$ and T_c of $CeCoIn_5$ single crystals are shown by solid lines. (b) Pressure dependence of the exponent ε in $\rho(T) = \rho_0 + AT^{\varepsilon}$, obtained from $d\ln\Delta\rho/d\ln T$ ($\Delta\rho = \rho(T) - \rho_0$), for the $CeCoIn_5(7)/CeIn_3(n)$ superlattices for $n = 13$ and 6. For comparison, ε for bulk $CeIn_3$ and $CeCoIn_5$ single crystals is shown.

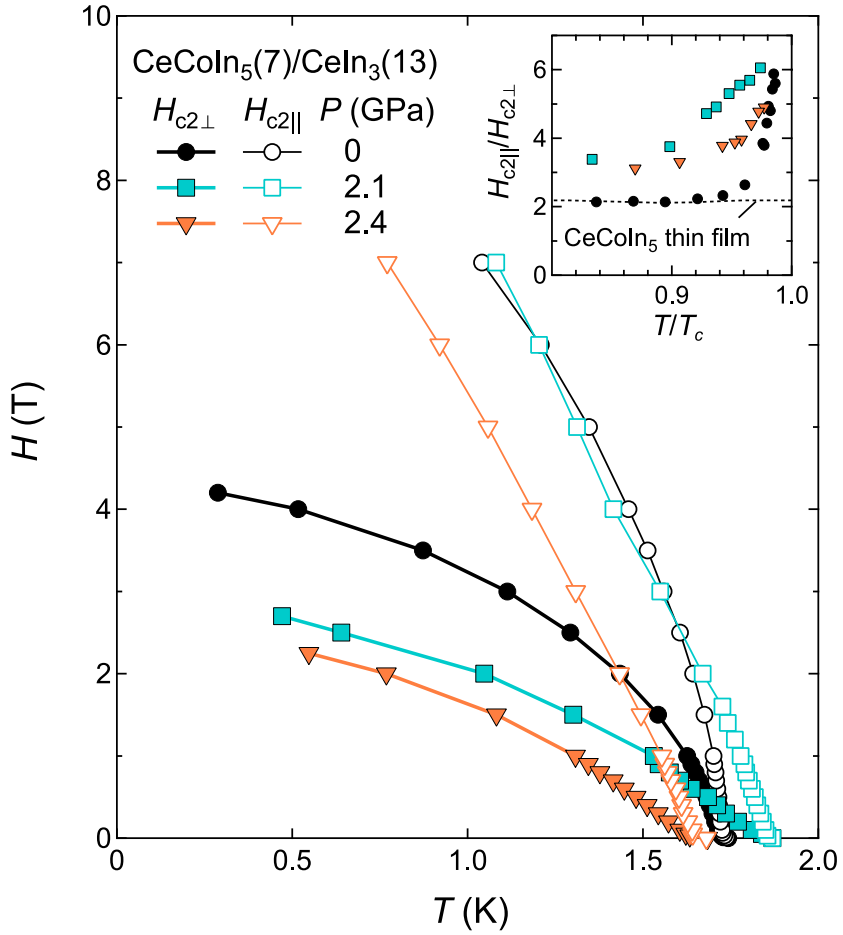

Figure 6.7: Temperature dependence of upper critical fields in magnetic fields parallel ($H_{c2\parallel}$, open symbols) and perpendicular ($H_{c2\perp}$, closed symbols) to the ab-plane for $CeCoIn_5(7)/CeIn_3(13)$ superlattice at ambient pressure and at 2.1 and 2.4 GPa. The inset shows anisotropy of the upper critical field, $H_{c2\parallel}/H_{c2\perp}$. The data of $CeCoIn_5$ thin film at ambient pressure is shown by dotted line.

6.4 Discussion

6.4.1 Upper critical field H_{c2}

It has been revealed that the temperature dependence of $H_{c2\perp}$ provides crucial information about the impact of the interface on the superconductivity in $CeCoIn_5$ BLs. In particular, the modification of the Pauli paramagnetic effect in the superlattice, which dominates the pair breaking in bulk $CeCoIn_5$ single crystals, gives valuable clues [81, 90, 112, 149]. 6.8(a) and (b) depict the T dependence of the $H_{c2\perp}$ of $CeCoIn_5(7)/CeIn_3(13)$ superlattice, normalized by the orbital-limited upper critical field at zero temperature, $H_{c2\perp}^{\rm orb}(0)$, which is obtained from the Werthamer-Helfand-Hohenberg (WHH) formula, $H_{c2\perp}^{\rm orb}(0) = -0.69T_c(dH_{c2\perp}/dT)_{T_c}$ [34]. In 6.8(a) and (b), two extreme cases are also included; the WHH curve with no Pauli pair-breaking and $H_{c2}/H_{c2\perp}^{\rm orb}(0)$ for bulk $CeCoIn_5$ single crystal [119]. For comparison, $H_{c2\perp}^{\rm orb}(0)$ for $CeCoIn_5/YbCoIn_5$ and $CeCoIn_5/CeRhIn_5$ are also shown [76, 90].

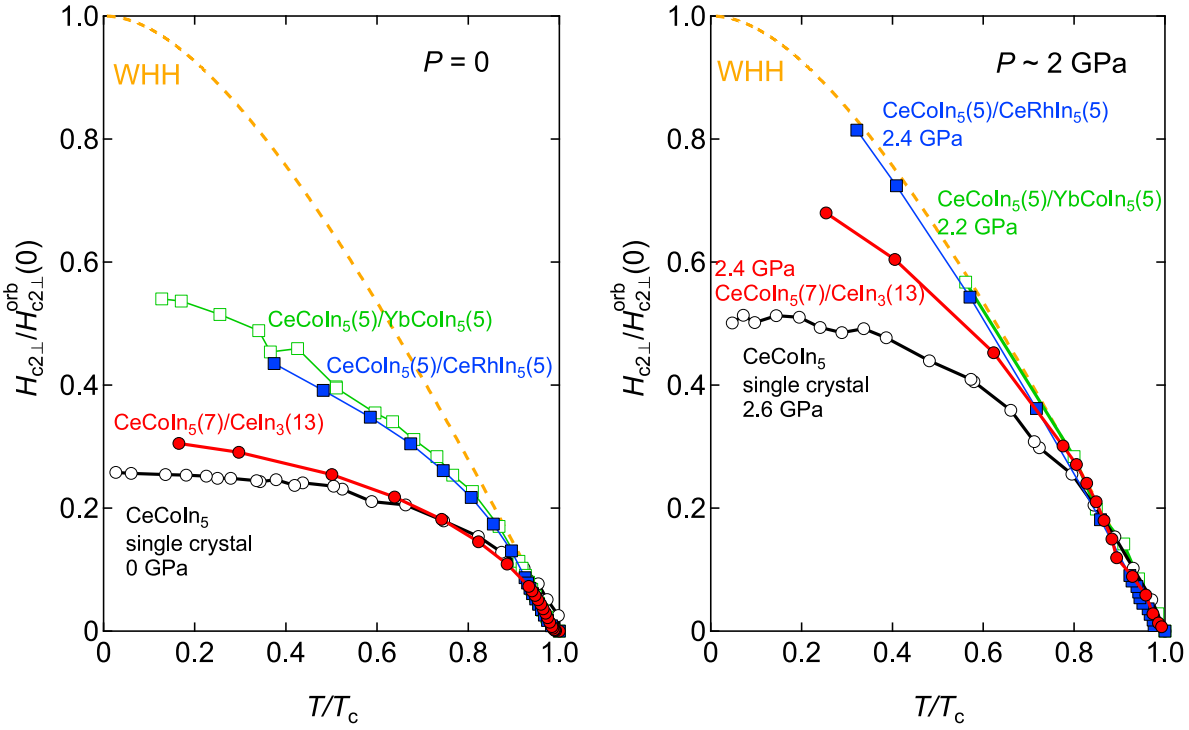

Figure 6.8: (a) Upper critical field in perpendicular field normalized by the orbital limiting upper critical field, $H_{c2\perp}/H_{c2\perp}^{\rm orb}(0)$, plotted as a function of T/T_c (a) at ambient pressure and (b) under pressure about 2 GPa for $CeCoIn_5(7)/CeIn_3(13)$ superlattices. For comparison, $H_{c2\perp}/H_{c2\perp}^{\rm orb}(0)$ for bulk $CeCoIn_5$ single crystal, $CeCoIn_5(5)/YbCoIn_5(5)$ and $CeCoIn_5(5)/CeRhIn_5(5)$ are shown. Orange dotted lines represent the WHH curve, which is upper critical field for purely orbital limiting.

At ambient pressure, $H_{c2\perp}/H_{c2\perp}^{\rm orb}(0)$ of $CeCoIn_5/YbCoIn_5$ and $CeCoIn_5/CeRhIn_5$ are strongly enhanced from that of $CeCoIn_5$ bulk single crystals, indicating the suppression of the Pauli paramagnetic pair-breaking effect. However, it has been pointed out that

the mechanisms of this suppression in these two systems are essentially different. In $CeCoIn_5/YbCoIn_5$, the enhancement of $H_{c2\perp}/H_{c2\perp}^{\rm orb}(0)$ is caused by the local inversion symmetry breaking at the interface [80, 81]. The asymmetry of the potential perpendicular to the 2D plane of the superlattice, $\nabla V \parallel [0\,0\,1]$, induces the Rashba spin-orbit interaction $\alpha_R = \boldsymbol{g}(\boldsymbol{k}) \cdot \boldsymbol{\sigma} \propto (\boldsymbol{k} \times \nabla V) \cdot \boldsymbol{\sigma}$, where $\boldsymbol{g}(\boldsymbol{k}) = (k_y, -k_x, 0)/k_F$, k_F and $\boldsymbol{\sigma}$ are the Fermi wave number and the Pauli matrices, respectively. The Rashba spin-orbit interaction splits the Fermi surface into two sheets with different spin textures [85]. The energy splitting is given by α_R, and the spin direction is tilted into the 2D plane, rotating clockwise on one sheet and anticlockwise on the other. When the Rashba splitting exceeds the superconducting gap energy ($\alpha_R > \Delta$), the superconducting state is dramatically modified [80, 85, 105]. In particular, when the magnetic field is applied perpendicular to the 2D plane, the magnetic field does not couple to the spins, leading to a suppression of the Pauli pair-breaking effect. At $p = 2.2\,\mathrm{GPa}$, $H_{c2\perp}/H_{c2\perp}^{\rm orb}(0)$ of $CeCoIn_5/YbCoIn_5$ nearly coincides with the WHH curve. This indicates that $H_{c2\perp}$ is dominated by the orbital pair breaking most likely due to the suppression of the Pauli paramagnetic pair-breaking effect by the Rashba splitting.

On the other hand, in $CeCoIn_5/CeRhIn_5$ superlattices, it has been shown that the effect of the local inversion symmetry breaking on $H_{c2\perp}$ is less important compared with $CeCoIn_5/YbCoIn_5$ [90]. It has been proposed that magnetic fluctuations (paramagnons) in $CeRhIn_5$ BLs injected through the interface dramatically enhance the force binding superconducting electron pairs in $CeCoIn_5$ BLs, leading to the enhancement of Δ. As a result, the Pauli limiting field $H_{c2\perp}^{\rm Pauli}(= \sqrt{2}\Delta/g\mu_{\rm B})$ is enhanced, where g is the g-factor of the electrons. This increases the relative importance of the orbital pair-breaking effect, giving rise to the enhancement of $H_{c2\perp}/H_{c2\perp}^{\rm orb}(0)$ [90]. At $p = 2.1\,\mathrm{GPa}$, which is close to the AFM QCP of $CeRhIn_5$ BLs, $H_{c2\perp}/H_{c2\perp}^{\rm orb}(0)$ nearly coincides with the WHH curve. This has been attributed to the enhanced Pauli limiting field that well exceeds the orbital limiting field ($H_{c2\perp}^{\rm Pauli} \gg H_{c2\perp}^{\rm orb}$) [90].

In contrast to $CeCoIn_5/YbCoIn_5$ and $CeCoIn_5/CeRhIn_5$, $H_{c2\perp}/H_{c2\perp}^{\rm orb}(0)$ is only slightly enhanced in $CeCoIn_5(7)/CeIn_3(13)$ superlattice at ambient pressure from that of bulk $CeCoIn_5$ single crystal. This indicates that $H_{c2\perp}$ is dominated by Pauli paramagnetic effect, i.e. $H_{c2\perp} \approx H_{c2\perp}^{\rm Pauli} \ll H_{c2\perp}^{\rm orb}$. This implies that the effect of local inversion symmetry breaking on the superconductivity in $CeCoIn_5/CeIn_3$ is weak compared with $CeCoIn_5/YbCoIn_5$. The local inversion symmetry is broken for the $CeCoIn_5/YbCoIn_5$ on the CoIn-layer while it is broken on the Ce layer for $CeCoIn_5/CeIn_3$ and $CeCoIn_5/CeRhIn_5$. Therefore, the present results suggest that the inversion symmetry breaking on the CoIn-layer induces a larger local electric field gradient. Moreover, superconducting electrons in $CeCoIn_5$ BLs are not strongly influenced by the AFM order in $CeIn_3$ BLs compared with $CeCoIn_5/CeRhIn_5$.

When superconductivity is dominated by the Pauli-limiting effect ($H_{c2\perp} \approx H_{c2\perp}^{\rm Pauli}$), $2\Delta/k_{\rm B}T_c$ is estimated as

$$\frac{2\Delta}{k_{\rm B}T_c} \approx \sqrt{2}\frac{g\mu_{\rm B}H_{c2\perp}}{k_{\rm B}T_c}. \tag{6.2}$$

where $\mu_{\rm B}$ is Bohr magneton and g is the g-factor of electron. In Figure 6.9, $g = 2$ is assumed. Figure 6.9 depicts the pressure dependence of $q = \sqrt{2}g\mu_{\rm B}H_{c2\perp}/k_{\rm B}T_c$ for

$CeCoIn_5/CeRhIn_5$ and $CeCoIn_5/CeIn_3$, along with q for bulk $CeCoIn_5$ single crystal. Here $g = 2$ is assumed. Although this simple assumption should be scrutinized, the fact that $q = 4.2$ of the bulk $CeCoIn_5$ is larger than the BCS value of $q = 3.54$ is consistent with the strong coupling superconductivity, which is supported by the specific heat measurements that reports $2\Delta/k_BT_c \approx 6$ [19]. The increase of q with pressure in $CeCoIn_5/CeRhIn_5$ implies the increase of $2\Delta/k_BT_c$. This increase has been attributed to an enhancement of the force binding superconducting electron pairs. In spin fluctuation mediated superconductors, the pairing interaction is mainly provided by high-energy fluctuations while low-energy fluctuations act as pair breaking. In this case, an increase of $2\Delta/k_BT_c$ occurs without accompanying a large enhancement of T_c, which is consistent with the results of $CeCoIn_5/CeRhIn_5$ [90]. Thus, the critical AFM fluctuations that develop in $CeRhIn_5$ BLs near the QCP are injected into the $CeCoIn_5$ BLs through the interface and strongly enhance the pairing interaction in $CeCoIn_5$ BLs.

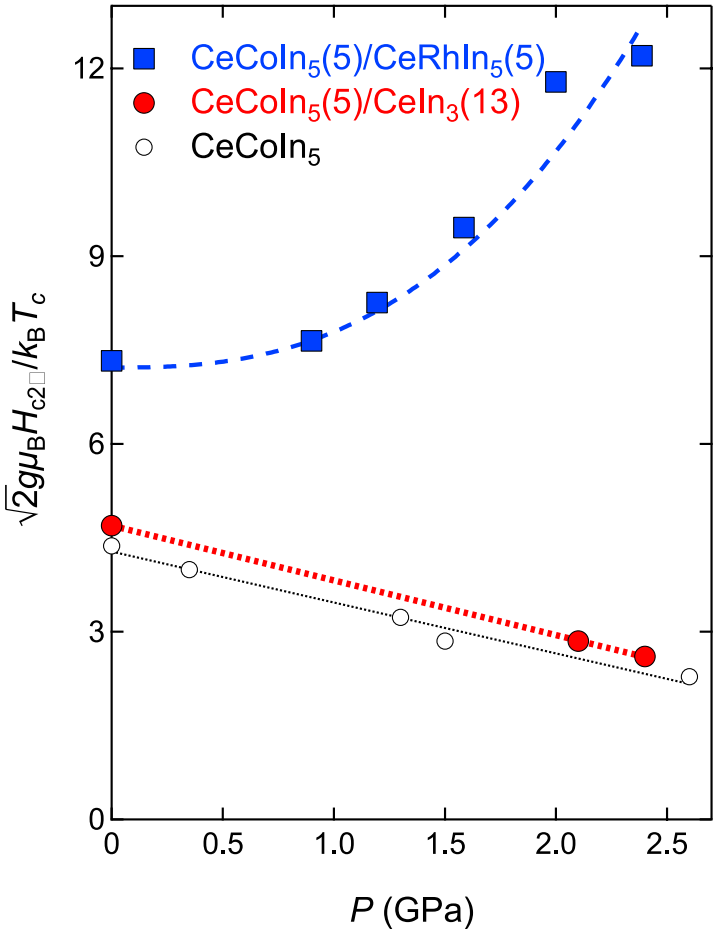

Figure 6.9: Pressure dependence of $q = \sqrt{2}g\mu_B H_{c2\perp}/k_BT_c \approx 2\Delta/k_BT_c$ for $CeCoIn_5(7)/CeIn_3(13)$ superlattice. For comparison, q of bulk $CeCoIn_5$ single crystal and $CeCoIn_5(5)/CeRhIn_5(5)$ are plotted.

In stark contrast to $CeCoIn_5/CeRhIn_5$ superlattices, q decreases with pressure in bulk $CeCoIn_5$ single crystal. This implies that the pairing interaction is weakened by

applying pressure, which is consistent with the fact that the pressure moves the system away from the QCP of $CeCoIn_5$. The reduction of $2\Delta/k_BT_c$ with pressure in bulk $CeCoIn_5$ single crystals is confirmed by the jump of the specific heat at T_c [150]. It should be stressed that the pressure dependence of q in $CeCoIn_5(7)/CeIn_3(13)$ is very similar to that of bulk $CeCoIn_5$. This strongly indicates that the pairing interactions in $CeCoIn_5$ BLs are barely influenced by AFM fluctuations injected from the adjacent $CeIn_3$ BLs through the interface even when $CeIn_3$ BLs are located near the AFM QCP.

6.4.2 Comparisoin with $CeCoIn_5/CeRhIn_5$ superlattice

The most salient feature in the $CeCoIn_5/CeIn_3$ superlattices is that the superconductivity of $CeCoIn_5$ BLs is little affected by the critical AFM fluctuations in $CeIn_3$ BLs, despite the fact that AFM fluctuations are injected from the adjacent $CeIn_3$ BLs into $CeCoIn_5$ BLs, as evidenced by the AFM order in $CeCoIn_5/CeIn_3$ demonstrating that different $CeIn_3$ BLs are magnetically coupled by the RKKY interaction through adjacent $CeCoIn_5$ BLs. Even in the vicinity of the AFM QCP of the $CeIn_3$ BLs, the superconducting state in the $CeCoIn_5$ BLs is very similar to that of $CeCoIn_5$ bulk single crystals. This indicates that the AFM fluctuations injected from $CeIn_3$ BLs do not help to enhance the force binding the superconducting electron pairs in $CeCoIn_5$ BLs. This is in stark contrast to $CeCoIn_5/CeRhIn_5$, in which the pairing force in $CeCoIn_5$ BL is strongly enhanced by the AFM fluctuations in $CeRhIn_5$ BLs [90], although the $CeRhIn_5$ BLs are magnetically only weakly coupled through $CeCoIn_5$ BLs.

We note that the superconducting phase appears under pressure in $CeRhIn_5$ single crystals and epitaxial thin films. On the other hand, in the $CeRhIn_5/YbRhIn_5$, zero resistivity is not attained even under pressure. This result indicates that the superconductvity of $CeRhIn_5$ is suppressed when the thickness of the BLs was reduced. Similarly, in $CeCoIn_5/CeRhIn_5$ superlattices, 2D superconductivity derived from the $CeCoIn_5$ BLs is thought to be realized from ambient pressure to under pressure near QCP.

This contrasting behaviors between $CeCoIn_5/CeIn_3$ and $CeCoIn_5/CeRhIn_5$ superlattices suggest that there are two possible important factors that determine whether magnetic fluctuations are injected through the interface; One is the magnetic wave vector and the other is the matching of the Fermi surface between two materials.

For $CeCoIn_5$, the Fermi surface is 2D-like and AFM fluctuations with wave vector $\boldsymbol{q}_0 = (0.45, 0.45, 0.5)$ are dominant [144]. The magnetic wave vector in the ordered phase of $CeIn_3$ is commensurate with $\boldsymbol{q}_0 = (0.5, 0.5, 0.5)$ [69]. The evolution of the ordered moment below T_N is consistent with mean field theory. While the wave number along the c axis, q_c, of $CeIn_3$ is the same as that of $CeCoIn_5$, the 3D Fermi surface of $CeIn_3$ is very different from the 2D Fermi surface of $CeCoIn_5$. On the other hand, for $CeRhIn_5$, $\boldsymbol{q}_0$ in the ordered phase is incommensurate $\boldsymbol{q}_0 = (0.5, 0.5, 0.297)$ at low pressure [62] and changes to $\boldsymbol{q}_0 = (0.5, 0.5, 0.4)$ above $\sim 1.0\,\mathrm{GPa}$ [151]. Thus, the q_c of $CeRhIn_5$ is different from the q_c of $CeCoIn_5$. The evolution of the ordered moment below T_N deviates from mean field behavior, likely due to 2D fluctuations. However, the 2D Fermi surface of $CeRhIn_5$ bears a close resemblance to that of $CeCoIn_5$.

The equality between the c axis component of $\boldsymbol{q}_0$ in $CeCoIn_5$ and $CeIn_3$ would explain why the magnetic coupling between $CeIn_3$ BLs through a $CeCoIn_5$ BL is stronger than that between $CeRhIn_5$ BLs. Thus, AFM order is formed in $CeCoIn_5(7)/CeIn_3(n)$ even for small n, for which the AFM order has already vanished in $CeCoIn_5(n)/CeRhIn_5(n)$. In magnetically mediated superconductors, the pairing interaction is expected to be strongly wave number dependent. Considering the good resemblance of the Fermi surface and the same $d_{x^2-y^2}$ superconducting gap symmetry of $CeCoIn_5$ and $CeRhIn_5$ [64], it is likely that the pairing interaction in both compounds has 2D character and peaks around the same wave number on the Fermi surface. Furthermore, it has been assumed that 2D magnetic fluctuations are strong in $CeRhIn_5$. Thus, superconductivity in the $CeCoIn_5$ BLs of $CeCoIn_5(n)/CeRhIn_5(n)$ is strongly influenced. On the other hand, in $CeIn_3$ with 3D Fermi surface, 2D AFM fluctuations are expected to be very weak. AFM fluctuations having 3D character in $CeIn_3$ may not play an important role for the pairing interaction in $CeCoIn_5$, resulting in little change of the superconductivity in $CeCoIn_5/CeIn_3$.

6.5 Summary

A state-of-the-art MBE technique has enabled us to fabricate superlattices consisting of different heavy-fermion compounds. These heavy-fermion superlattices provide a unique opportunity to study the mutual interaction between unconventional superconductivity and magnetic order through the atomic interface. In hybrid superlattice $CeCoIn_5/CeIn_3$, the superconductivity in $CeCoIn_5$ BLs and AFM order in $CeIn_3$ BLs coexist in spatially separated layers. We find that each $CeIn_3$ BL is magnetically coupled by the RKKY interaction through adjacent $CeCoIn_5$ BLs. An analysis of the upper critical field under pressure reveals that the superconductivity in $CeCoIn_5$ BLs is little influenced even in the presence of abundant AFM fluctuations in the vicinity of the AFM QCP of adjacent $CeIn_3$ BLs. Thus, although the AFM fluctuations are injected to the $CeCoIn_5$ BLs from the $CeIn_3$ BLs through the interfaces, they barely influence the force binding superconducting electron pairs. This is in sharp contrast to $CeCoIn_5/CeRhIn_5$, in which the superconductivity in the $CeCoIn_5$ BLs is strongly influenced by quantum critical AFM fluctuations in $CeRhIn_5$ BLs.

It has been widely believed that 2D AFM fluctuations are essential for the pairing interaction in $CeCoIn_5$, however, direct evidence was lacking. The present results provide strong support that 2D AFM fluctuations are fundamentally crucial for the unconventional superconductivity in $CeCoIn_5$.

Chapter 7

Conclusion

In this thesis, we have studied the interplay between unconventional superconductivity and magnetically ordered- or conventional metallic-state through the interface. By using a state-of-the-art molecular beam epitaxy technique, we have established new strategies for controlling unconventional superconductivity in artificially engineered heavy-fermion superlattices.

In Chapter 4, we have designed and fabricated tricolor superlattice, in which strongly correlated superconductor $CeCoIn_5$ is sandwiched by nonmagnetic metals $YbCoIn_5$ and $YbRhIn_5$ with different electronic structures. By stacking three compounds repeatedly in an asymmetric sequence such as $YbCoIn_5/CeCoIn_5/YbRhIn_5$, we can introduce the global inversion symmetry breaking along the stacking direction. We find that the Rashba asymmetric spin-orbit coupling (ASOC) induced by the global inversion symmetry breaking in these tricolor superlattices leads to profound changes in the superconducting properties of $CeCoIn_5$ with atomic thickness. The upper critical field exhibits unusual temperature and angular dependence, indicating that the Rashba ASOC induced in the tricolor superlattices leads to the strong suppression of the Pauli paramagnetic pair-breaking effect. We also demonstrate that the magnitude of the Rashba ASOC incorporated into the two-dimensional (2D) $CeCoIn_5$ block layers (BLs) is controllable by changing the thickness of $CeCoIn_5$ BLs. Moreover, the temperature dependence of the in-plane upper critical field exhibits an anomalous upturn at low temperatures, which is attributed to a possible emergence of a helical or stripe superconducting phase. Our results demonstrate that the tricolor superlattices provide a new playground for exploring exotic superconducting states in the strongly correlated 2D electron systems with the Rashba effect.

In Chapter 5, we have designed and fabricated hybrid superlattices consisting of alternating atomic layers of *d*-wave superconductor $CeCoIn_5$ and antiferromagnetic (AFM) metal $CeRhIn_5$, in which the AFM order can be suppressed by applying pressure. We also established the hydrostatic pressure measurements on the heavy-fermion thin films and heavy-fermion superlattices. We find that the superconducting and AFM states coexist in spatially separated layers, but their mutual coupling via the interface significantly modifies the superconducting properties. An analysis of upper critical fields reveals that in the vicinity of the quantum critical point (QCP) of $CeRhIn_5$ BLs, the

superconducting pairing strength $2\Delta/k_{\rm B}T_c$ have strongly increased. This is the first realization that the superconducting pairing can be tuned nontrivially by magnetic fluctuations (paramagnons) injected through the interface.

In Chapter 6, we designed and fabricated hybrid superlattices consisting of alternating layers of $CeCoIn_5$ and heavy-fermion AFM metal $CeIn_3$, in which the AFM transition temperature is higher than $CeRhIn_5$ and AFM order can be suppressed by pressure as in $CeRhIn_5$. We demonstrated that by changing the number of magnetic layers in the superlattice, 2D magnetic order was realized in $CeCoIn_5/CeRhIn_5$, while three-dimensional (3D) magnetic order was realized in $CeCoIn_5/CeIn_3$. The analysis of the upper critical field revealed that the superconductivity of the $CeCoIn_5$ layers was not affected by the magnetic fluctuations of the $CeIn_3$ layer even in the vicinity of the QCP of $CeIn_3$ BLs. This is in sharp contrast to the superconductivity in $CeCoIn_5/CeRhIn_5$, which is strongly affected by the magnetic fluctuations of the $CeRhIn_5$ BLs. Focusing on the dimensionality of magnetic fluctuations of each AFM material, it is suggested that there are 2D AFM fluctuations in $CeRhIn_5$ and 3D AFM fluctuations in $CeIn_3$. It has been widely believed that 2D AFM fluctuations are important for the pairing interaction in $CeCoIn_5$. However, direct evidence was lacking. The present results provide strong support that 2D AFM fluctuations are essentially important for the unconventional superconductivity in $CeCoIn_5$.

Bibliography

[1] N. D. Mathur, F. M. Grosche, S. R. Julian, I. R. Walker, D. M. Freye, R. K. W. Haselwimmer, and G. G. Lonzarich, *Nature* **394**, 39–43 (1998).

[2] T. Shibauchi, A. Carrington, and Y. Matsuda, *Annu. Rev. Condens. Matter Phys.* **5**, 113 (2014).

[3] D. Faltermeier, J. Barz, M. Dumm, M. Dressel, N. Drichko, B. Petrov, V. Semkin, R. Vlasova, C. Meziere, and P. Batail, *Phys. Rev. B* **76**, 165113 (2007).

[4] Y. Sato, S. Kasahara, H. Murayama, Y. Kasahara, E.-G. Moon, T. Nishizaki, T. Loew, J. Porras, B. Keimer, T. Shibauchi, and Y. Matsuda, *Nat. Phys.* **13**, 1074–1078 (2017).

[5] S. Sachdev, "Quantum phase transitions.", Cambridge University Press (2011).

[6] T. Moriya and K. Ueda, *Adv. In Phys.* **49**, 555606 (2000).

[7] B. Keimer, S. A. Kivelson, M. R. Norman, S. Uchida, and J. Zaanen, *Nature* **518**, 179 (2015).

[8] N. Sato, and K. Miyake, "Heavy Fermion Physics: Magnetism and Superconductivity", The University of Nagoya Press (2013).

[9] J. Kondo, *Prog. Theor. Phys.* **32**, 37 (1964).

[10] M. A. Ruderman and C. Kittel, *Phys. Rev.* **96**, 99 (1954).

[11] T. Kasuya, *Prog. Theo. Phys.* **16**, 45 (1956).

[12] K. Yoshida, *Phys. Rev.* **106**, 896 (1957).

[13] N. Mott, *Philosophical Magazine* **30**, 403 (1974).

[14] S. Doniach, *Physica B+C* **91**, 231–234 (1977).

[15] H. V. Löhneysen, A. Rosch, M. Vojta, and P. Wölfle, *Rev. Mod. Phys.* **79**, 1015 (2007).

[16] T. Park, F. Ronning, H. Q. Yuan, M. B. Salamon, R. Movshovich, J. L. Sarrao, and J. D. Thompson, *Nature* **440**, 65–68 (2006).

[17] P. Gegenwart, Q. Si, and F. Steglich, *Nat. Phys.* **4**, 186 (2008).

[18] M. Sato and S. Fujimoto, *Phys. Rev. Lett.* **105**, 217001 (2010).

[19] C. Petrovic, P. G. Pagliuso, M. F. Hundley, R. Movshovich, J. L. Sarrao, J. D. Thompson, Z. Fisk, and P. Monthoux, *J. Phys. Condens. Matter* **13**, L337 (2001).

[20] H. Hegger, C. Petrovic, E. G. Moshopoulou, M. F. Hundley, J. L. Sarrao, Z. Fisk, and J. D. Thompson, *Phys. Rev. Lett.* **84**, 4986 (2000).

[21] C. Petrovic, R. Movshovich, M. Jaime, P. G. Pagliuso, M. F. Hundley, J. L. Sarrao, Z. Fisk, and J. D. Thompson, *Europhys. Lett.* **53**, 354 (2001).

[22] J. L. Sarrao, L. A. Morales, J. D. Thompson, B. L. Scott, G. R. Stewart, F. Wastin, J. Rebizant, P. Boulet, E. Colineau, and G. H. Lander, *Nature (London)* **420**, 297 (2002).

[23] F. Steglich, J. Aarts, C. D. Bredl, W. Lieke, D. Meschede, W. Franz, H. Schäfer, *Phys. Rev. Lett.* **43**, 1892 (1979).

[24] H. R. Ott, H. Rudigier, Z. Fisk, J. L. Smith, *Phys. Rev. Lett.* **50**, 1595 (1983).

[25] G. R. Stewart, Z. Fisk, J. O. Willis, J. L. Smith, *Phys. Rev. Lett.* **52**, 679 (1984).

[26] T. T. M. Palstra, A. A. Menovsky, J. van den Berg, A. J. Dirkmaat, P. H. Kes, G. J. Nieuwenhuys, J. A. Mydosh, *Phys. Rev. Lett.* **55**, 2727 (1985).

[27] M. B. Maple, J. W. Chen, Y. Dalichaouch, T. Kohara, C. Rossel, M. S. Torikachvili, M. W. McElfresh, J. D. Thompson, *Phys. Rev. Lett.* **56**, 185 (1986).

[28] W. Schlabitz, J. Baumann, B. Pollit, U. Rauchschwalbe, H. M. Mayer, U. Ahlheim, C. D. Bredl, *Z. Phys. B* **62**, 171 (1986).

[29] F. M. Grosche, S. R. Julian, N. D. Mathur, G. G. Lonzarich, *Physica B* **223** & **224**, 50 (1996).

[30] P. Monthoux and G. G. Lonzarich, *Phys. Rev. B* **59**, 14598 (1999).

[31] M. Tinkham, "Introduction to Superconductivity", 2nd ed., McGraw-Hill, New York (1996).

[32] R. Settai, H. Shishido, S. Ikeda, Y. Murakawa, M. Nakashima, D. Aoki, Y. Haga, H. Harima, and Y. Onuki, *J. Phys. Condens. Matter* **13**, L627 (2001).

[33] G. Knebel, D. Aoki, J.-P. Brison, and J. Flouquet, *J. Phys. Soc. Jpn.* **77**, 114704 (2008).

[34] N. R. Werthamer, E. Helfand, and P. C. Hohenberg, *Phys. Rev.* **147**, 295 (1966).

[35] H. Shishido, R. Settai, D. Aoki, S. Ikeda, H. Nakawaki, N. Nakamura, T. Iizuka, Y. Inada, K. Sugiyama, T. Takeuchi, K. Kindo, T. C. Kobayashi, Y. Haga, H. Harima, Y. Aoki, T. Namiki, H. Sato, and Y. Ōnuki, *J. Phys. Soc. Japan* **71**, 162 (2002).

[36] H. Shishido, R. Settai, H. Harima, and Y. Ōnuki, *J. Phys. Soc. Jpn.* **74**, 1003–1106 (2005).

[37] V. A. Sidorov, M. Nicklas, P. G. Pagliuso, J. L. Sarrao, Y. Bang, A. V. Balatsky, and J. D. Thompson, *Phys. Rev. Lett.* **89**, 157004 (2002).

[38] Y. Kohori, Y. Yamato, Y. Iwamoto, T. Kohara, E. D. Bauer, M. B. Maple, and J. L. Sarrao, *Phys. Rev. B* **64**, 134526 (2001).

[39] J. S. Kim, J. Alwood, G. R. Stewart, J. L. Sarrao, and J. D. Thompson, *Phys. Rev. B* **64**, 134524 (2001).

[40] E. D. Bauer, F. Ronning, C. Capan, M. J. Graf, D. Vandervelde, H. Q. Yuan, M. B. Salamon, D. J. Mixson, N. O. Moreno, S. R. Brown, J. D. Thompson, R. Movshovich, M. F. Hundley, J. L. Sarrao, P. G. Pagliuso, and S. M. Kauzlarich, *Phys. Rev. B* **73**, 245109 (2006).

[41] L. D. Phamet, T. Park, S. Maquilon, J. D. Thompson, and Z. Fisk, *Phys. Rev. Lett.* **97**, 056404 (2006).

[42] M. Nicklas, O. Stockert, T. Park, K. Habicht, K. Kiefer, L. D. Pham, J. D. Thompson, Z. Fisk, and F. Steglich, *Phys. Rev. B* **76**, 052401 (2007).

[43] S. Nair, O. Stockert, U. Witte, M. Nicklas, R. Schedler, K. Kiefer, J. D. Thompson, A. D. Bianchi, Z. Fisk, S. Wirth, and F. Steglich, *Proc. Natl. Acad. Sci. USA* **107**, 9537 (2010).

[44] S. Seo, X. Lu, J.-X. Zhu, R. R. Urbano, N. Curro, E. D. Bauer, V. A. Sidorov, L. D. Pham, T. Park, Z. Fisk, and J. D. Thompson, *Nat. Phys.* **10**, 120 (2014).

[45] E. Bauer, N. Moreno, D. Mixson, J. Sarrao, J. Thompson, M. Hundley, R. Movshovich, and P. Pagliuso, *Physica B* **359–361**, 35 (2005).

[46] M. Daniel, S.-W. Han, C. Booth, A. Cornelius, E. Bauer, and J. Sarrao, *Physica B* **359–361**, 401 (2005).

[47] E. D. Bauer, C. Capan, F. Ronning, R. Movshovich, J. D. Thompson, and J. L. Sarrao, *Phys. Rev. Lett.* **94**, 047001 (2005).

[48] J. Donath, P. Gegenwart, R. Köchler, N. Oeschler, F. Steglich, E. Bauer, and J. Sarrao, *Physica B* **378–380**, 98 (2006).

[49] S. M. Ramos, M. B. Fontes, E. N. Hering, M. A. Continentino, E. Baggio-Saitovich, F. D. Neto, E. M. Bittar, P. G. Pagliuso, E. D. Bauer, J. L. Sarrao, and J. D. Thompson, *Phys. Rev. Lett.* **105**, 126401 (2010).

[50] K. Chen, F. Strigari, M. Sundermann, Z. Hu, Z. Fisk, E. D. Bauer, P. F. S. Rosa, J. L. Sarrao, J. D. Thompson, J. Herrero-Martin, E. Pellegrin, D. Betto, K. Kummer, A. Tanaka, S. Wirth, and A. Severing, *Phys. Rev. B* **97**, 1 (2018).

[51] S. Ohira-Kawamura, H. Shishido, A. Yoshida, R. Okazaki, H. Kawano-Furukawa, T. Shibauchi, H. Harima, and Y. Matsuda, *Phys. Rev. B* **76**, 132507 (2007).

[52] V. S. Zapf, E. J. Freeman, E. D. Bauer, J. Petricka, C. Sirvent, N. A. Frederick, R. P. Dickey, and M. B. Maple, *Phys.Rev. B* **65**, 014506 (2001).

[53] M. P. Allan, F. Massee, D. K. Morr, J. Van Dyke, A. W. Rost, A. P. Mackenzie, C. Petrovic, and J. C. Davis, *Nat. Phys.* **9**, 468 (2013).

[54] B. B. Zhou, S. Misra, E. H. da Silva Neto, P. Aynajian, R. E. Baumbach, J. D. Thompson, E. D. Bauer, and A. Yazdani, *Nat. Phys.* **9**, 474 (2013).

[55] K. Izawa, H. Yamaguchi, Y. Matsuda, H. Shishido, R. Settai, and Y. Onuki, *Phys. Rev. Lett.* **87**, 057002 (2001).

[56] K. An, T. Sakakibara, R. Settai, Y. Onuki, M. Hiragi, M. Ichioka, and K. Machida, *Phys. Rev. Lett.* **104**, 037002 (2010).

[57] P. Fulde and R. A. Ferrell, *Phys. Rev.* **135**, A550 (1964).

[58] A. I. Larkin and Y. N. Ovchinnikov, *Zh. Eksp. Teor. Fiz* **47**, 1136 (1964).

[59] J. D. Thompson and Z. Fisk, *J. Phys. Soc. Japan* **81**, 1 (2012).

[60] S. Gerber, M. Bartkowiak, J. L. Gavilano, E. Ressouche, N. Egetenmeyer, C. Niedermayer, A. D. Bianchi, R. Movshovich, E. D. Bauer, J. D. Thompson, and M. Kenzelmann, *Nat. Phys.* **10**, 126 (2014).

[61] D. Y. Kim, S. Z. Lin, F. Weickert, M. Kenzelmann, E. D. Bauer, F. Ronning, J. D. Thompson, and R. Movshovich, *Phys. Rev. X* **6**, 1 (2016).

[62] W. Bao, P. G. Pagliuso, J. L. Sarrao, J. D. Thompson, Z. Fisk, J. W. Lynn, and R. W. Erwin, *Phys. Rev. B* **62**, R14621 (2000).

[63] Y. Ida, R. Settai, Y. Ota, F. Honda, and Y. Onuki, *J. Phys. Soc. Jpn* **77**, 084708 (2008).

[64] W. K. Park, J. L. Sarrao, J. D. Thompson, and L. H. Greene, *Phys. Rev. Lett.* **100**, 177001 (2008).

[65] T. Takeuchi, T. Inoue, K. Sugiyama, D. Aoki, Y. Tokiwa, Y. Haga, K. Kindo, and Y. Ōnuki, *J. Phys. Soc. Jpn.* **70**, 877 (2001).

[66] L. Jiao, Y. Chen, Y. Kohama, D. Graf, E. D. Bauer, J. Singleton, J.-X. Zhu, Z. Weng, G. Pang, T. Shang, J. Zhang, H.-O. Lee, T. Park, M. Jaime, J. D. Thompson, F. Steglich, Q. Si, and H. Q. Yuan, *Proc. Natl. Acad. Sci. USA* **112**, 673 (2015).

[67] F. Ronning, T. Helm, K. R. Shirer, M. D. Bachmann, L. Balicas, M. K. Chan, B. J. Ramshaw, R. D. McDonald, F. F. Balakirev, M. Jaime, E. D. Bauer, and P. J. W. Moll, *Nature* **548**, 313 (2017).

[68] L. Jiao, Z. F. Weng, M. Smidman, D. Graf, J. Singleton, E. D. Bauer, J. D. Thompson, and H. Q. Yuan, *Philos. Mag.* **97**, 3446 (2017).

[69] A. Benoit, J. X. Boucherle, P. Convert, J. Flouquet, J. Pellau, and J. Schweizer, *Solid State Commun.* **34**, 293 (1980).

[70] G. Knebel, D. Braithwaite, P. C. Canfield, G. Lapertot, and J. Flouquet, *Phys. Rev. B* **65**, 024425 (2001).

[71] V. I. Zaremba, U. C. Rodewald, R.-D. Hoffmann, Y. M. Kalychak, R. Pöettgen, *Z. anorg. allg. Chem.* **629**, 1157–1161. (2003).

[72] C. H. Booth, T. Durakiewicz, C. Capan, D. Hurt, A. D. Bianchi, J. J. Joyce and Z. Fisk, *Phys. Rev. B*, **83**, 235117 (2011).

[73] Z. Bukowski, K. Gofryk, and D. Kaczorowski, *Solid State Commun.* **134**, 475 (2005).

[74] H. T. Huy, S. Noguchi, N. V. Hieu, X. Shao, T. Sugimoto and T. Ishida, *Journal of Magnetism and Magnetic Materials*, **321**, 2425–2428 (2009).

[75] H. Shishido, T. Shibauchi, K. Yasu, T. Kato, H. Kontani, T. Terashima, and Y. Matsuda, *Science* **327**, 980 (2010).

[76] Y. Mizukami, H. Shishido, T. Shibauchi, M. Shimozawa, S. Yasumoto, D. Watanabe, M. Yamashita, H. Ikeda, T. Terashima, H. Kontani, and Y. Matsuda, *Nat. Phys.* **7**, 849 (2011).

[77] T. Ishii, R. Toda, Y. Hanaoka, Y. Tokiwa, M. Shimozawa, Y. Kasahara, R. Endo, T. Terashima, A. H. Nevidomskyy, T. Shibauchi, and Y. Matsuda, *Phys. Rev. Lett.* **116**, 206401 (2016).

[78] K. Kadowaki and S. B. Woods, *Solid State Commun.* **58**, 507 (1986).

[79] M. Shimozawa, S. K. Goh, T. Shibauchi, and Y. Matsuda, *Reports Prog. Phys.***79**, 074503 (2016).

[80] D. Maruyama, M. Sigrist, and Y. Yanase, *J. Phys. Soc. Jpn.* **81**, 034702 (2012).

[81] S. K. Goh, Y. Mizukami, H. Shishido, D. Watanabe, S. Yasumoto, M. Shimozawa, M. Yamashita, T. Terashima, Y. Yanase, T. Shibauchi, A. I. Buzdin, and Y. Matsuda, *Phys. Rev. Lett.* **109**, 157006 (2012).

[82] T. Yamanaka, M. Shimozawa, R. Endo, Y. Mizukami, H. Shishido, T. Terashima, T. Shibauchi, Y. Matsuda, and K. Ishida, *Phys. Rev. B* **92**, 241105(R) (2015).

[83] E. I. Rashba, *Sov. Phys. Solid State* **2**, 1109 (1960).

[84] Y. A. Bychkov and E. I. Rashba, *JETP Lett.* **39**, 78 (1984).

[85] E. Bauer and M. Sigrist, "Non-Centrosymmetric Superconductors: Introduction and Overview", Lecture Notes in Physics, Springer-Verlag, Berlin, Heidelberg (2012).

[86] R. E. Honing and D. A. Karmer, *RCA Review* **30**, 285–305 (1969).

[87] 3D model of the MBE machine using the Blender software was provided by Mr. Yosuke Hanaoka.

[88] M. Izaki, H. Shishido, T. Kato, T. Shibauchi, Y. Matsuda, T. Terashima, *Applied Physics Letters* **91**, 122507 (2007).

[89] O. K. Soroka, G. Blendin, and M. Huth, *Journal of Physics: Condensed Matter*, **19**, (5), 056006 (2007).

[90] M. Naritsuka, P. F. S. Rosa, Yongkang Luo, Y. Kasahara, Y. Tokiwa, T. Ishii, and Y. Matsuda, *Phys. Rev. Let.* **120**, 187002 (2018).

[91] A. G. Zaitsev, A. Beck, R. Schneider, R. Fromknecht, D. Fuchs, J. Geerk, and H. v. Löhneysen, *Physica C Supercond*, **469**, (1), 52–54. (2009).

[92] J. Hänisch, F. Ronning, R. Movshovich, and V. Matias, *Physica C Supercond*, **470**, S568-S569. (2010).

[93] J. Kim, H. H. Lee, S. Lee, S. Park, T. Park, Y. Cho, W. S. Choi, *Curr. Appl. Phys.*, **19**, (12), 1338–1342 (2019).

[94] B. A. Joyce, P. J. Dobson, J. H. Neave, K. Woodbrige, J. Zhang, P. K. Larsen, and Bölger, *Surf. Sci.* **168**, 423–438 (1986).

[95] A. Eiling and J. S. Schilling, *J. Phys. F: Metal Phys.* **11**, 623–639 (1981).

[96] Y. Uwatoko, M. Hedo, N. Kurita, M. Koeda, M. Abliz, and T. Matsumoto, *Physica B* **329–333**, 1658–1659 (2003).

[97] S. Murakami, N. Nagaosa, and C. Zhang, *Science* **301**, 1348–1351 (2003).

[98] J. Sinova, D. Culcer, Q. Niu, N. A. Sinitsyn, T. Jungwirth, A. H. MacDonald, *Phys. Rev. Lett.* **92**, 126603 (2004).

[99] X.-L. Qi and S.-C. Zhang, *Rev. Mod. Phys.* **83**, 1057–1110 (2011).

[100] V. P. Mineev, *Low Temp. Phys.* **37**, 872 (2011).

[101] C.-K. Lu and S. K. Yip, *Phys. Rev. B* **78**, 132502 (2008).

[102] L. P. Gor'kov and E. I. Rashba, *Phys. Rev. Lett.* **87**, 037004 (2001).

[103] P. A. Frigeri, D. F. Agterberg, A. Koga, and M. Sigrist, *Phys. Rev. Lett.* **92**, 097001 (2004).

[104] Y. Tanaka, T. Yokoyama, A. V. Balatsky, and N. Nagaosa, *Phys. Rev. B* **79**, 060505(R) (2009).

[105] S. Fujimoto, *J. Phys. Soc. Jpn.* **76**, 051008 (2007).

[106] D. Maruyama and Y. Yanase, *J. Phys. Soc. Jpn.* **84**, 074702 (2015).

[107] E. Bauer, G. Hilscher, H. Michor, Ch. Paul, E. Scheit, A. Gribanov, Yu. Seropegin, H. Noël, M. Sigrist, and P. Rogl, *Phys. Rev. Lett.* **92**, 027003 (2004).

[108] N. Kimura, K. Ito, K. Saitoh, Y. Umeda, H. Aoki, and T. Terashima, *Phys. Rev. Lett.* **95**, 247004 (2005).

[109] T. Akazawa, H. Hidaka, T. Fujiwara, T. C. Kobayashi, E. Yamamoto, Y. Haga, R. Settai, and Y. Ōnuki, *J. Phys.: Condens. Matter* **16**, L29 (2004).

[110] G. Dresselhaus, *Phys. Rev.* **100**, 580 (1955).

[111] D. F. Agterberg and R. P. Kaur, *Phys. Rev. B* **75**, 064511 (2007).

[112] M. Shimozawa, S. K. Goh, R. Endo, R. Kobayashi, T. Watashige, Y. Mizukami, H. Ikeda, H. Shishido, Y. Yanase, T. Terashima, T. Shibauchi, and Y. Matsuda, *Phys. Rev. Lett.* **112**, 156404 (2014).

[113] R. Peters, Y. Tada, and N. Kawakami, *Phys. Rev. B* **88**, 155134 (2013).

[114] J.-H. She and A. V. Balatsky, *Phys. Rev. Lett.* **109**, 077002 (2012).

[115] T. Schneider and A. Schmidt, *Phys. Rev. B* **47**, 5915 (1993).

[116] C. Stock, C. Broholm, J. Hudis, H. J. Kang, and C. Petrovic, *Phys. Rev. Lett.* **100**, 087001 (2008).

[117] Y. Yanase and M. Sigrist, *J. Phys. Soc. Jpn.* **77**, 124711 (2008).

[118] T. Takimoto, *J. Phys. Soc. Jpn.* **77**, 113706 (2008).

[119] T. Tayama, A. Harita, T. Sakakibara, Y. Haga, H. Shishido, R. Settai, and Y. Onuki, *Phys. Rev. B* **65**, 180504(R) (2002).

[120] M. Tinkham, *Phys. Rev.* **129**, 2413 (1963).

[121] A. M. Clogston, *Phys. Lett.* **9**, 266 (1962).

[122] K. V. Samokhin, *Phys. Rev. Lett.* **94**, 027004 (2005).

[123] A. Gurevich, *Phys. Rev. B* **67**, 184515 (2003).

[124] L. N. Bulaevskii, O. V. Dolgov, and M. O. Ptitsyn, *Phys. Rev. B* **38**, 11290–11295 (1988).

[125] Y. Matsuda and H. Shimahara, *J. Phys. Soc. Jpn.* **76**, 051005 (2007).

[126] R. Lortz, Y. Wang, A. Demuer, P. H. M. Böttger, B. Bergk, G. Zwicknagl, Y. Nakazawa, and J. Wosnitza, *Phys. Rev. Lett.* **99**, 187002 (2007).

[127] R. P. Kaur, D. F. Agterberg, and M. Sigrist, *Phys. Rev. Lett.* **94**, 137002 (2005).

[128] K. Kakuyanagi, M. Saitoh, K. Kumagai, S. Takashima, M. Nohara, H. Takagi, and Y. Matsuda, *Phys. Rev. Lett.* **94**, 047602 (2005).

[129] K. Kumagai, H. Shishido, T. Shibauchi, and Y. Matsuda, *Phys. Rev. Lett.* **106**, 137004 (2011).

[130] H. A. Radovan, N. A. Fortune, T. P. Murphys, S. T. Hannahs, E. C. Palm, S. W. Tozer, and D. Hall, *Nature (London)* **425**, 51 (2003).

[131] Y. Yanase and M. Sigrist, *J. Phys. Soc. Jpn.* **78**, 114715 (2009).

[132] A. Daido and Y. Yanase, *Phys. Rev. B* **95**, 134507 (2017).

[133] N. F. Q. Yuan, C. L. M. Wong, K. T. Law, *Physica E* **55**, 30 (2014).

[134] T. Yoshida, M. Sigrist, and Y. Yanase, *Phys. Rev. B* **86**, 134514 (2012).

[135] T. Yoshida, M. Sigrist, and Y. Yanase, *J. Phys. Soc. Jpn.* **82**, 074714 (2013).

[136] T. Yoshida, M. Sigrist, and Y. Yanase, *Phys. Rev. Lett.* **115**, 027001 (2015).

[137] D. Huang and J. E. Hoffman, *Annu. Rev. Condens. Matter Phys.* **8**, 311–336 (2017).

[138] D.-H. Lee, *Chin. Phys. B* **24**, 117405 (2015).

[139] J. J. Lee, F. T. Schmitt, R. G. Moore, S. Johnston, Y.-T. Cui, W. Li, M. Yi, Z. K. Liu, M. Hashimoto, Y. Zhang, D. H. Lu, T. P. Devereaux, D.-H. Lee, and Z.-X. Shen, *Nature* **515**, 245–248 (2014).

[140] L. Rademaker, Y. Wang, T. Berlijn, and S. Johnston, *New J. Phys.* **18**, 02201 (2016).

[141] M. Kenzelmann, Th. Strässle, C. Niedermayer, M. Sigrist, B. Padmanabhan, M. Zolliker, A. D. Bianchi, R. Movshovich, E. D. Bauer, J. L. Sarrao, and J. D. Thompson, *Science* **321**, 1652 (2008).

[142] G. Knebel, D. Aoki, J.-P. Brison, L. Howald, G. Lapertot, J. Panarin, S. Raymond, and J. Flouquet, *Phys. Status Solidi B* **247**, 557–562 (2010).

[143] Y. Nakajima, H. Shishido, H. Nakai, T. Shibauchi, K. Behnia, K. Izawa, M. Hedo, Y. Uwatoko, T. Matsumoto, R. Settai, Y. Onuki, H. Kontani, and Y. Matsuda, *J. Phys. Soc. Jpn.* **76**, 024703 (2007).

[144] S. Raymond and G. Lapertot, *Phys. Rev. Lett.* **115**, 037001 (2015).

[145] B. J. Ramshaw, S. E. Sebastian, R. D. McDonald, J. Day, B. S. Tan, Z. Zhu, J. B. Betts, R. Liang, D. A. Bonn, W. N. Hardy, and N. Harrison, *Science* **348**, 317–320 (2015).

[146] W. Witczak-Krempa, G. Chen, Y. B. Kim, and L. Balents, *Annu. Rev. Condens. Matter Phys.* **5**, 57 (2014).

[147] A. Bianchi, R. Movshovich, N. Oeschler, P. Gegenwart, F. Steglich, J. D. Thompson, P. G. Pagliuso, and J. L. Sarrao, *Phys. Rev. Lett.* **89**, 137002 (2002).

[148] B. L. Young, R. R. Urbano, N. J. Curro, J. D. Thompson, J. L. Sarrao, A. B. Vorontsov, and M. J. Graf, *Phys. Rev. Lett.* **98**, 1 (2007).

[149] M. Naritsuka, T. Ishii, S. Miyake, Y. Tokiwa, R. Toda, M. Shimozawa, T. Terashima, T. Shibauchi, Y. Matsuda, and Y. Kasahara, *Phys. Rev. B* **96**, 174512 (2017).

[150] G. Knebel, M.-A. Méasson, B. Salce, D. Aoki, D. Braithwaite, J. P. Brison, and J. Flauquet, *J. Phys.: Condens. Matter* **16**, 8905 (2004).

[151] S. Raymond, G. Knebel, D. Aoki, and J. Flouquet, *Phys. Rev. B* **77**, 172502 (2008).

[152] G. Nakamine, T. Yamanaka, S. Kitagawa, M. Naritsuka, T. Ishii, T. Shibauchi, T. Terashima, Y. Kasahara, Y. Matsuda, and K. Ishida, *Phys. Rev. B* **99**, 081115(R) (2019).

[153] T. Ebihara, I. Umehara, A. K. Albessard, K. Satoh, and Y. Onuki, *Physica B* **123–125**, 186 (1993).

[154] N. Harrison, U. Alver, R. G. Goodrich, I. Vekhter, J. L. Sarrao, P. G. Pagliuso, N. O. Moreno, L. Balicas, Z. Fisk, D. Hall, *Phys. Rev. Lett.* **93**, 186405 (2004).

[155] N. Oeschler, P. Gegenwart, M. Lang, R. Movshovich, J. L. Sarrao, J. D. Thompson, and F. Steglich, *Phys. Rev. Lett.* **91**, 076402 (2003).

Published works

Main works

1) **M. Naritsuka**, S. Nakamura, Y. Kasahara, T. Terashima, R. Peters, and Y. Matsuda, "Coupling between the heavy-fermion superconductor $CeCoIn_5$ and the antiferromagnetic metal $CeIn_3$ through the atomic interface", *Physical Review B* **100**, 024507 (2019).

2) **M. Naritsuka**, P. F. S. Rosa, Yongkang Luo, Y. Kasahara, Y. Tokiwa, T. Ishii, S. Miyake, T. Terashima, T. Shibauchi, F. Ronning, J. D. Thompson, and Y. Matsuda, "Tuning the Pairing Interaction in a *d*-Wave Superconductor by Paramagnons Injected through Interfaces", *Physical Review Letters* **120**, 187002 (2018).

3) **M. Naritsuka**, T. Ishii, S. Miyake, Y. Tokiwa, R. Toda, M. Shimozawa, T. Terashima, T. Shibauchi, Y. Matsuda, and Y. Kasahara, "Emergent exotic superconductivity in artificially engineered tricolor Kondo superlattices", *Physical Review B* **96**, 174512 (2017).

Reference works

1) Genki Nakamine, Takayoshi Yamanaka, Shunsaku Kitagawa, **Masahiro Naritsuka**, Tomohiro Ishii, Takasada Shibauchi, Takahito Terashima, Yuichi Kasahara, Yuji Matsuda, and Kenji Ishida, "Modification of magnetic fluctuations by interfacial interactions in artificially engineered heavy-fermion superlattices", *Physical Review B* **99**, 081115(R) (2019).

2) Masahiro Haze, Robert Peters, Yohei Torii, Tomoka Suematsu, Daiki Sano, **Masahiro Naritsuka**, Yuichi Kasahara, Takasada Shibauchi, Takahito Terashima, and Yuji Matsuda, "Direct Evidence for the Existence of Heavy Quasiparticles in the Magnetically Ordered Phase of $CeRhIn_5$", *Journal of Physical Society of Japan* **88**, 014706 (2019).

Acknowledgements

I am grateful to my supervisor Professor Yuji Matsuda for his support and continuous encouragement throughout my Ph.D. student career. His valuable guidance and unique perspective was a great assistance to at all times during the course of my research. I also would like to thank Professor Takahito Terashima, who provided me with great advice and fruitful discussion regarding my experimental methods and results. Had it not been for both of them, I would never have developed this study.

I wish to express my appreciation for Professor Yuichi Kasahara, Professor Shigeru Kasahara, Professor Yoshifumi Tokiwa, Professor Yoichi Yanase, Professor Robert Peters, Professor Hiroshi Kontani, Professor Takasada Shibauchi, Professor Masaaki Shimozawa, and Professor Kenji Ishida for their productive discussions related to my experimental work. I also would like to acknowledge Professor Filip Ronning and Professor Joe D. Thompson for their kind support during my stay at Los Alamos National Laboratory, and for supporting my experiments and for helpful consultation. I would like to thank Professor Kenji Ishida, Dr. Takayoshi Yamanaka, and Mr. Genki Nakamine for establishing the NMR measurement on heavy-fermion superlattices that require ultra-high sensitivity, and for fruitful discussions. I would like to thank Dr. Masahiro Haze, Mr. Tomohiro Ishii, Mr. Sohei Miyake, Mr. Rintaro Toda, Dr. P. F. S. Rosa, Professor Yongkang Luo, and Dr. Yuta Mizukami for their efforts to support my research.

I am deeply indebted to all the members of the group of Professor Matsuda and Professor Terashima at Kyoto University, namely, Mr. Yuki Sato, Ms. Hinako Murayama, Mr. Ryo Kurihara, Mr. Daiki Sano, and Mr. Satoshi Nakamura. Their discussions and help were all significant to me.

I am grateful to the staff members of the Research Center for Low Temperature and Material Science at Kyoto University for cryogenic service. I wish to acknowledge the financial support provided by the Research Fellowship of the Japan Society for Promotion of Science for Young Scientists. Finally, I would like to express my gratitude to my parents and the rest of my family for their support and warm encouragement.